Dynamic and Quasi-Static Mechanical Properties of Fe-Ni Alloy Honeycomb

A Dissertation
Presented to
The Academic Faculty

By

Justin L. Clark

In Partial Fulfillment
of the Requirements for the Degree
Doctor of Philosophy in the
School of Materials Science and Engineering

Georgia Institute of Technology
12 April 2004

Dynamic and Quasi-Static Mechanical Properties of Fe-Ni Alloy Honeycomb

Approved by:

Dr. Joe K. Cochran

Dr. Thomas H. Sanders

Dr. David McDowell

Dr. Naresh Thadhani

Dr. Jim Lee

Date Approved 12 April 2004

Dedication

I would like to dedicate this work to my family for their love and support throughout my many wonderful years at Georgia Tech.

Acknowledgements

I would like to thank my committee members: Dr. Joe Cochran, Dr. Tom Sanders, Dr. David McDowell, Dr. Naresh Thadhani, and Dr. Jim Lee, for their advice and expertise that they so freely shared. I would like to thank my fellow graduate students for their support and comradery: Ben Church, Kevin Hurysz, Jason Nadler, Matt Trexler, Tracie Zoeller, Tammy McCoy, and Raymond Oh. Many thanks to Greg Kennedy, Matt McGill, and Lou Ferranti for their excellent tutoring in the arts of gas gun maintenance. I would also like to acknowledge the financial support of this research provided by (1) DARPA/DSO under ONR Grant N00014-99-1-1016 directed by Dr. Leo Christodoulou, (2) ONR under ONR Grant N00014-99-1-0852 directed by Dr. Steve Fishman, and (3) NSWC Dahlgren Division under contract N00178-03-Q-1008 directed by Robert Garrett.

Table of Contents

List of Tables

List of Figures

Summary

Several metal honeycombs, termed Linear Cellular Alloys (LCA's), were fabricated via a paste extrusion process and thermal treatment. Two Fe-Ni based alloy compositions were evaluated. Maraging steel and Super Invar were chosen for their compatibility with the process and the wide range of properties they afforded. Cell wall material was characterized and compared to wrought alloy specifications. The bulk alloy was found to compare well with the more conventionally produced wrought product when porosity was taken into account. The presence of extrusion defects and raw material impurities were shown to degrade properties with respect to wrought alloys. The performance of LCA's was investigated for several alloys and cell morphologies. The results showed that out-of-plane properties exceeded model predictions and in-plane properties fell short due to missing cell walls and similar defects. Strength and energy absorption were shown to outperform several existing cellular metals by as much as an order of magnitude in some instances. Finally, the suitability of LCA's as an energetic capsule was investigated. The investigation found that the LCA's added significant static strength and as much as three to five times improvement in the dynamic strength of the system. More importantly, it was shown that the pressures achieved with the LCA capsule were significantly higher than the energetic material could achieve alone. High pressures coupled with the fragmentation of the capsule during impact increased the likelihood of initiation and propagation of the energetic reaction. This multi-functional aspect of the LCA makes it a suitable capsule material.

Chapter 1

Introduction

Lightweight multifunctional materials are of great interest to academia and industry for their potential in weight saving applications. Weight is fast becoming a critical design criterion in a climate that demands increasing performance and low environmental impact. Performance factors such as stiffness and energy absorption must be improved without the concomitant increase in weight that would arise from simply increasing the cross-section of a structural member. In order to accomplish weight reduction while retaining or improving performance the engineer must rely on new alloy and structural designs. Cellular materials have been one solution to the ladder design consideration. These materials encompass low-density structures utilizing a high degree of porosity, i.e., foams, or alternatively a honeycomb structure.

Foams derive their low density from the 3-dimensional distribution of pores throughout the material. The process by which the foams are made will dictate the characteristics of the porosity. These characteristics, which include pore size, shape, distribution, and connectivity, intrinsically affect the performance of the foam, i.e. strength, stiffness, and isotropy. Honeycombs, on the other hand, are made up of a 2-dimensional space-filling array of cells with varied sizes and shapes. The 2-dimensional nature of honeycombs imposes mechanical anisotropy, i.e. properties perpendicular to the cell axis will necessarily be different from those parallel.

The processing of honeycombs includes the stacking of corrugated metal sheets, commonly used in aerospace applications, and extrusions. Extrusion processing has been used most notably to make honeycomb cordierite substrates that can subsequently be coated with a catalyzing agent and used in commercial catalytic converter applications. Extrusion technology is particularly attractive given the labor intensive and expensive nature of corrugated lay-ups. Still, extrusions on the scale of fine honeycombs seen in catalytic applications have been chiefly restricted to ceramic pastes with yield strengths that can be tailored to flow well through the extrusion dies.

The focus of this paper is the performance of honeycombs fabricated using a metal chemo-powder extrusion process. Essentially, honeycomb extrusions are formed from metal oxide pastes. These green honeycombs can be heated in a reducing atmosphere to convert the oxides to metal and sinter the structure. The result is dense metal sheets forming walls of the honeycomb. The honeycombs are designated linear cellular alloys (LCA's) due to their unique processing and design.

In this paper, a series of ferrous compositions and honeycomb designs are investigated for metallurgy, mechanical behavior, and modeling of linear cellular alloys processed via the oxide powder reduction method. The alloy compositions used in this study are based on the Fe-Ni system and yield a wide range of strengths and ductilities for comparison. Maraging steel compositions consist of Fe, Ni, Co, Mo, and Ti. Compositional variations allow this alloy to range in yield strength from 1400 MPa to more than 2400 MPa while maintaining reasonable toughness ranging from 40 to 150 MPa $m^{1/2}$. Super Invar is a Fe-Ni-Co alloy possessing an ultra-low coefficient of thermal expansion over a significant range including ambient temperatures. The annealed

condition of the alloy yields a significantly lower strength than the maraging steel with the advantage of high ductility. Cooling of the Super Invar alloy increases strength and gives intermediate properties as compared to the annealed Super Invar and lowest strength maraging steel. The large range of properties and small compositional variations make these alloys ideal for validation of direct-reduced alloys in light of conventional processing and for modeling and validation of LCA behavior.

Extensive characterization of the bulk properties of direct-reduced alloys is performed for the purpose of comparison to traditionally processed alloys and to create a database of direct-reduced alloy performance for analyzing LCA mechanical behavior. A triangular honeycomb design and a square annulus design with triangular honeycomb walls are fabricated and tested to analyze LCA performance under quasi-static compression and to compare LCA performance to honeycomb models from the literature. Finally, dynamic properties of LCA's are tested using a modified version of the classic Taylor anvil impact test. In these tests a specially designed LCA is impacted by a projectile traveling at high velocity. The resulting deformation is captured with high speed digital imaging for analysis. The purpose is to determine the suitability of LCA's as encapsulants for energetic materials or penetrators.

Chapter 2

Cellular Metals Fabrication

Cellular materials are a class of materials that incorporate cells bounded by solid matrix in a space-filling configuration. The cells may be open to the air or contain an inert gas. The cells may also fill space in two or three dimensions. A 2-dimensional (linear) arrangement of cells creates what is commonly known as a honeycomb. The most notable honeycomb is that associated with the honeybee. These honeycombs are made up of hexagonal unit cells and can be periodic in nature. In general, any 2-D arrangement of cells can constitute a honeycomb including multiple cell shapes, sizes, or periodicity. A 3-dimensional arrangement of cells is called foam. Ideally, foam fabrication would create uniformly dispersed, monosized, regular cells throughout the material. In practice foams have varied cell shapes, sizes, and distributions depending on the fabrication method.

Interest in cellular materials is based on several useful properties that are unique to this class. Mechanical, acoustical, and thermal applications make up the bulk of interests for which cellular materials continue to be researched. Particular interest has been given to the development of cellular metal alloys for use in impact mitigation and lightweight structural components. Numerous researchers have generated models to better understand and predict the behavior of cellular materials under various loading conditions.

The method of fabrication of cellular materials can have substantial implications on the performance of the material. Often, processing dictates what characteristics of the cellular structure can be controlled during fabrication. Process control and the nature and frequency of defects have a direct impact on the mechanical performance of cellular alloys.

2.1 Metal Foam Fabrication

Several methods exist for the fabrication of metallic foams. An extensive list of the processes has been compiled by John Banhart of the Fraunhofer-Institute for Manufacturing and Advanced Materials. [1,2] The techniques are categorized by the form of the starting materials. They include liquid state processing, solid state processing, electro-deposition, and vapour deposition. Several of these techniques involving the use of liquid and powder metals are reviewed in the following section.

2.1.1 Foams from Molten Metals

The majority of research on molten metal foam processing incorporates the evolution of gas from a liquid melt. Early attempts to fabricate foams used gas injectors to force a gas such as air, argon, or nitrogen into a liquid melt. As the gas bubbles rose to the surface of the melt the metal would solidify trapping the gases and creating a metal foam. With the addition of silicon carbide or aluminum oxide particles, the viscosity of the melt could be varied to control the rate of gas evolution from the melt and, consequently, the final foam density. Cymat of Canada and Hydro Aluminum of Norway continue to further develop this particular technique. As a continuous casting process, Cymat claims a casting rate of approximately 900 kg/hr making this an attractive

process.[3] However, the particle additions, as much as 20 volume percent, used to control the viscosity of the melt have an undesired side effect. In the solidified foam the ceramic particles embrittle the bulk material and significantly degrade its mechanical performance.

Other processes utilizing gas evolution in the foaming process include the ALPORAS process developed in Japan and the GASARS process developed in the Ukraine. The ALPORAS technique adds foaming agents to the melt to generate the gas bubbles. Shinko-Wire in Japan uses TiH_2 to this end. As the hydride decomposes, hydrogen gas is released into the melt creating the bubbles that become entrapped upon solidification. This batch process remains small scale and continues to be researched. The GASARS process takes advantage of the eutectic phase that some liquid metals form with hydrogen gas. By cooling a melt through this phase field the hydrogen is evolved generating the gas bubbles. Controlled properly, the GASARS gas evolution method leads to finely dispersed pores with porosities ranging from 5-75 volume percent.

Additional methods for fabricating metal foams from a melt include investment casting and casting around low-density filler material. Investment casting requires generation of a mold into which the molten metal is cast. Often this involves infiltrating polymer foam with a slurry mixture that is subsequently dried. The polymer is burned out leaving a negative of the original foam. Metal is cast into the resultant mold creating the metal foam. This foam fabrication technique allows complex shapes with porosities ranging from 80 to 97%.

2.1.2 Foams from Metal and Metal Oxide Powders

Metal foam fabrication is not restricted to molten metal processing as evidenced by numerous techniques utilizing metal powders or similar precursor materials. One such process patented by the Fraunhofer Institute in Bremen mixes a foaming agent such as a metal hydride with metal alloy powders. The powder mixture can be compacted and further processed using a number of conventional methods such as rolling or extrusion. After final forming the article is heated to decompose the foaming agent and create the foam structure. Metals such as aluminum, tin, zinc, brass, bronze, and lead can be processed to this effect.

Another fabrication method that uses powder as a starting material is the coaxial nozzle process developed at the Georgia Institute of Technology. This process was the forerunner to the current paste extrusion process that will be described in the following section. In the coaxial nozzle process hollow ceramic spheres are produced by passing an acetone-based slurry through the outer annulus of a coaxial nozzle creating a hollow cylinder of slurry. An inner-jet of an inert gas such as nitrogen is injected into the hollow cylinder destabilizing the cylinder. This causes the walls to pinch off and create hollow spheres of slurry. As the spheres fall through a heated air updraft, the acetone evaporates from the sphere walls leaving a ceramic shell bonded by polymer additives. Slurry compositions consist of acetone, ceramic precursor powders (typically a metal oxide or hydride with an average particle size of approximately 4 microns), a polymer dispersant to prevent flocculation and a polymer binder for added green strength. Solids loading and dispersant concentrations are adjusted to obtain proper viscosity for processing. Slurry feed rate and inner jet rate are controlled to produce the most desirable sustained

sphere production. Sphere formation rates of 5000-6000 spheres per minute are typical and monosized(± 4%), 2–3 millimeter spheres are the result. Adjustment to the control variables such as viscosity, slurry feed rate, and inner jet rate allows production of spheres with various sizes and wall thickness. The end result is the ability to control final foam density.

An alternative spray-coating process may also be used to generate the hollow metal spheres. This process uses sacrificial polymer beads as a substrate for the ceramic powder slurries. The slurries are sprayed onto the spherical substrates and allowed to dry. Thermal processing in a reducing atmosphere simultaneously deoxidizes the powders to metal and incinerates the polymer cores leaving metal shells.

Once formed the shells generated from the coaxial nozzle or spray-coating process can be bonded together in the green, fired, or reduced state. An aqueous bond slurry consisting of the appropriate powder precursors is mixed with the shells and then cast into a suitable mold. The bond slurry provides additional material at points of contact for formation of necks and improves the foam integrity. The combination of open and closed porosity allows densities on the order of 10% theoretical bulk density.

2.2 Metal Honeycomb Fabrication

2.2.1 Traditional Metal Honeycombs

Metal honeycombs have most notably been used in sandwich panel constructions that are incorporated into aerospace applications. These constructions provide significant stiffness without the weight costs of solid structural members. The honeycomb core is fabricated by laying up several pieces of alloy sheet. The sheets are bonded to each other

along parallel, periodically spaced strips of adhesive. To create the honeycomb these bonded sheets are pulled apart until near symmetric cells are created between bonded joints. This bonding method allows only for the use of hexagonal cells and results in one-third of the cell walls having a thickness of twice the starting alloy sheet thickness. Corrugated sheets may also be stacked in a periodic manner and bonded together to create a honeycomb structure. This technique allows more flexibility in cell shape than simply bonding flat sheets. For example, triangular honeycombs may be fabricated by using a V-shaped corrugation capped by a flat sheet. These layers can be stacked to create the honeycomb structure. Again, this technique this results in double thickness walls along points of contact between sheets. Defects can result from failed bond joints, uneven adhesive spacing, and incomplete cell expansion. At this point, the honeycomb core must be bonded to alloy sheets to complete the sandwich panel construction. The additional bonding joints with the face sheets can also be a site for failure due to incomplete bonding or adhesive failure.

2.2.2 Linear Cellular Alloys

Linear cellular alloy is a term given to the metallic honeycombs fabricated using oxide paste extrusion and heat treatment. The process incorporates traditional aspects of ceramic paste extrusion to produce a green body honeycomb with sufficient strength to retain its shape. The dried ceramic honeycomb is reduced to metal upon heating in a reducing atmosphere.

The pastes are prepared through conventional means. The precursor powders are dry blended with a methylcellulose binder in the appropriate proportions. The proportion

of oxide powders is determined by the metal yield upon reduction. The rheological behavior of the pastes can be controlled by the amount of liquid phase present. This includes the binder (methylcellulose), water, and lubricant (pegospurse). The proportions are chosen to give the best possible extrusion. Paste rheology, as it relates to LCA extrusion, has been studied extensively by Hurysz.[4]. After mixing, the batch is processed through a high shear compounding mixer to ensure paste homogeneity. Pastes are extruded through a reduced cross-section die with the appropriate honeycomb design. The green extrusions are dried and thermally treated in a reducing atmosphere to convert the oxide to metal and sinter the structure.

The reduction stage of processing places special restrictions on the raw materials used to make the LCAs. Specifically, the ceramic powder precursor materials must be reducible in a hydrogen atmosphere at realistic temperatures and oxygen partial pressures. Investigation of the Ellingham diagram can pinpoint the exact requirements for reduction of several oxides. Oxides of iron, copper, cobalt, and nickel have been used with great success thus far. Alloying components such as aluminum and titanium present a special challenge for incorporation into LCAs. The use of metal hydrides has been investigated as an alternative component for incorporating these types of alloying elements. In the case of titanium hydride, the material is stable to 400°C making it suitable for the reduction process. Typical particle size range for the raw material powders averages 2-8 μm.

2.3 Effects of Fabrication Method on Mechanical Properties

When predicting the behavior of cellular materials under load one must account for the degree of perfection expected in either the foam or honeycomb. The nature of commercially viable foam fabrication prevents the production of ideal closed cell foams with a homogeneous distribution of closed, monosized, uniform cells as modeled by researchers. Variable thickness or missing cell walls, holes, inclusions, cell wall curvature and corrugation, and otherwise irregular cells are not controllable by the fabrication methods detailed previously. This will result in significant variability in properties and overall anisotropic behavior. For example, studies by Sanders and Gibson on closed cell foams suggest that cell wall curvature and corrugation have a significant knockdown effect on the Young's modulus by a factor of 2-3.[5]

Honeycombs can suffer a similar knockdown effect from the presence of holes, cell wall corrugation or missing cell walls. The proven technology behind traditional ceramic honeycomb extrusion affords the capability to produce green honeycombs with very low defect concentrations. Through chemo-powder processing, linear cellular alloys can be fabricated with properties that can be reliably predicted through modeling and the design of which can be easily altered to fit the required application.

Chapter 3

Bulk Alloy Characterization

Chemo-powder processing is the term given to the method of metal honeycomb production wherein oxide powder precursor shapes are used to create the final metallic product. This process bears many similarities to powder metallurgy where metal powders (pre-alloyed or pure) are used as starting materials. Because of particle size considerations, the use of oxide powder allows traditional paste extrusion techniques to generate the honeycomb structure and thermal processing in a reducing atmosphere converts oxide particles to metallic which gives rise to the "chemo" terminology. This method of processing does have some limitations when considering alloying components that are difficult to reduce such as titanium and aluminum. However, the use of hydrides and intermetallics are being investigated as an alternative for incorporating such elements. Numerous alloy systems may be pursued using this fabrication method including, but not limited to, copper, nickel, and iron alloys. In this chapter the effects of processing metal alloys by chemo-powder techniques compared to conventional processing is investigated. Several alloys were fabricated and tested to characterize bulk materials making up the linear cellular alloys.

3.1 Background

As discussed previously, chemo-powder processing has more similarities to powder metallurgy, but there are two significant differences. The first of these differences is the use of oxide powders and the requirement for subsequent reduction to

metal that has been previously discussed. The second is that the LCA fabrication process produces a green cellular body in final geometry, neglecting dimensional changes. Because the structure is cellular, the material cannot undergo pressure-assisted sintering such as in the HIP process nor can it undergo additional working, such as forging. The implications are that elements of the microstructure such as porosity, homogeneity, and feature sizes must be controlled in the oxide paste extrusion and thermal processing stages.

3.1.1 Powder Processing

The paste extrusion technique used to fabricate linear cellular materials is only one of many possible powder processing techniques available for forming useful parts from powders. Pressing, slip casting, solid casting, tape casting and injection molding are also common processing methods for ceramic materials. Processing of metallic powder may also be used to fabricate metallic parts. Powder metallurgy uses many of the same concepts as ceramic powder processing to shape and densify raw materials into parts of near-theoretical density. For metals, powders, either ceramic or metallic, allow the use of high purity, homogeneous starting materials to produce homogeneous bulk materials. This is especially attractive for alloys where high purity is necessary or in highly alloyed materials where segregation during traditional melt casting techniques is an issue. Regardless of the reasons for using these techniques, the greatest issue associated with powder processing is the consolidation of the powder form into a uniform, homogeneous mass.

Typically, the efficiency of packing for randomly distributed monosized spheres is approximately 60%.[6] This means that 40% of the remaining volume is atmospheric gas or what is more commonly referred to as pores. Pores in the final product can have a severe effect on the performance of the material. Consequently, much of the effort in powder processing is directed towards porosity reduction. To this end, several techniques are used throughout the stages of forming to improve particle packing and reduce porosity in the end product. Characteristics of the raw material, such as particle size, are the first control that can be employed to improve packing. Powder particle size distributions can be adjusted to optimally fill interstices between larger particles with smaller particles. A size distribution that yields a large to small particle diameter ratio of 7:1 is required for minimal interstitial packing and for significant interstitial packing a minimum ratio of 14 is required. Powders used in the production of LCAs fulfilled this requirement with particle sizes ranging from 0.5 to 10 μm.

Additionally, mechanical forming techniques such as vibrating or pressing can reduce the porosity of the body. Both of these techniques work to more efficiently fill interstices. Pressing of metal powders gives the added benefit of using materials with lower flow stresses as compared to ceramics. Consequently, material can be deformed to fill open volumes and the added dislocations that are created in the material aid in the later stages of consolidation. An additional aid of heating during pressing, known as hot pressing, can further reduce the flow stress of the material and enhance diffusion during sintering. Under these conditions full density can be achieved. However, the added expense and complexity of the equipment is a disadvantage.[7] For extrusion processing of LCAs, these techniques cannot be used because the extruded green form is the final form

of the product prior to sintering. Additional work on the material would destroy the honeycomb structure. Instead, efficient use of binder to reduce inherent porosity and good extrusion techniques to reduce defects such as those caused by inadequate de-airing of the paste, must be utilized.

Ultimately, once the LCA extrusion is made, the final recourse for the removal of porosity is through sintering. As previously discussed the chemo-powder process utilizes a flowing hydrogen atmosphere during the sintering process to convert the oxide powders to their metallic constituents. Similarly, it is conventional in powder metallurgy to use a slightly reducing or inert atmosphere to prevent oxidation during sintering at high temperatures. However, the chemo-powder process has the advantage of using much finer particle sizes due to the use of ceramic powders. Since reduction takes place prior to sintering in these materials the combination of the metallic nature of the material and the fine particles size serve to favorably enhance the sintering behavior of the body. As a result, final densities approaching theoretical can be achieved.

3.1.2 Porosity Effects

Porosity is of particular concern in direct-reduced alloys due the degradation of mechanical properties. Several reports on hot isostatically pressed maraging steel powder cite porosity or microvoids as being responsible for the majority of deficiencies in the final product.[8,9] Bocchini reports several relationships for sintered materials in which the material properties are a function of the porosity.[10] The relationships for strength, rupture elongation, and elastic modulus are as follows:

$$\sigma = \sigma_o e^{-4.3P},$$

$$e_{fs} = e_o e^{-10.6P},$$

$$E_s = E_o(1-P)^{3.4},$$

where, σ is strength at a fractional porosity of P, σ_o is strength at zero porosity, e_{fs} is the elongation at failure for a given porosity, e_o is the elongation at failure for zero porosity, E_s is the modulus at porosity P, E_o is modulus of fully dense materials and the exponential powers are empirical constants that describe a variety of materials. A comparison of the predicted effects of porosity is shown in Figure 3.1. Modulus and yield strength show very similar behavior with increasing porosity possessing nearly linear relationships. Modulus reaction to porosity is predicted to be marginally better

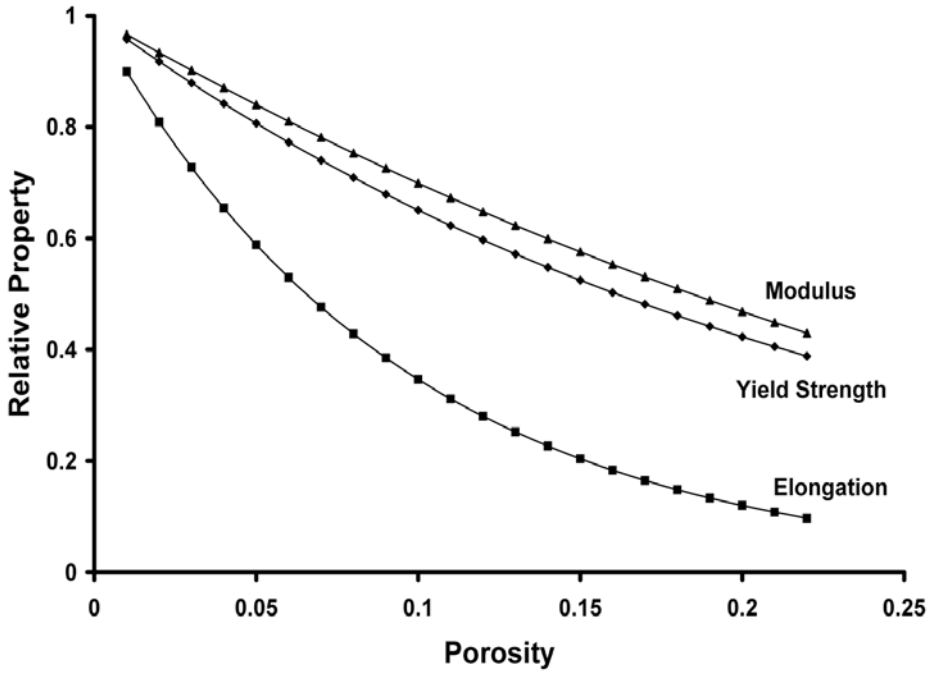

Figure 3.1 – Reduction in relative property with respect to fraction porosity as postulated by Bocchini.

than strength. The greatest impact of porosity is seen in the relative elongation with a drop of ~40% for a porosity of only 5%. This will have implications in the behavior of the LCAs since the bulk alloy will not be fully dense. The relationships derived by Bocchini are used in this study as a lower bound to compare chemo-powder processed alloys to their wrought counterparts. An upper bound assuming a linear relationship of relative property to relative density may also be used for comparison since typical porosities were ~5%.

3.1.3 Alloy Selection

The alloys selected for study in this research are based on the Fe-Ni system. The choice of these alloys was based on prior work with processing an austenitic stainless steel alloy (Fe-Ni-Cr) using the oxide powder processing technique. In that research it was determined that the chromium oxide component was difficult to fully reduce. Subsequent research has shown that full reduction can be achieved depending on the concentration of chromium oxide.[11] Due to the difficulties with Cr reduction, two other alloy systems were chosen for study. Maraging steel and Super Invar alloys were investigated based on the reducibility of the component oxides and the overall range of mechanical properties offered by the two systems.

Maraging Steel

The maraging steel compositions studied in this research were chosen due to their combination of high strength and toughness. Based on the Fe-Ni system, these steels derive their strength from two microstructural phenomena: a martensitic transformation and a precipitation event. The martensitic transformation occurs on furnace cooling from

solutionizing temperatures. Fe-Ni martensite is considered to be a "soft" martensite as compared to the higher dislocation density Fe-C martensite. Subsequent aging at elevated temperatures causes the evolution of precipitates of which Ni_3Ti and Ni_3Mo are chiefly credited with the most significant strengthening effects.[12] The compositions of three different maraging steel grades are given in Table 3.1. With the exception of titanium, the primary alloying elements for maraging steels (Fe, Ni, Co, and Mo) are readily reduced in hydrogen. Titanium oxide, however, remains stable at sufficiently high temperatures and oxygen partial pressures to preclude its use in the processing of these alloys. It was determined that there were two options available with which to pursue these compositions containing Ti. The first and simplest solution was to omit the Ti addition at the expense of some strength. However, an increase in Ti from 0.1% to 0.7% for a M200 based alloy increased yield strength by more than 25%.[13] Because of the strengthening effect of Ti, TiH_2 was explored as a viable titanium source in this

Table 3.1 – Composition and mechanical properties of wrought alloys.

	Composition (wt%)					
	Fe	Ni	Co	Mo	Ti	Al
M200	69.9	18	8.5	3.3	0.2	0.1
M350	63.2	18	12.5	4.8	1.4	0.1
M400	59.5	17.88	14.75	6.69	1.1	0.08
Super Invar	62.89	31.75	5.36	--	--	--

	Mechanical Properties		
	UTS (MPa)	YTS (MPa)	El (%)
M200	1500	1400	10
M350	2450	2400	6
M400	2693	2617	6
Super Invar	483	276	40

process. The hydride powder readily decomposes on heating to 400°C. The main concerns with the use of TiH_2 are stability during past processing and the potential re-oxidation of the Ti metal during the reduction of the surrounding oxide powders. Ultimately, both options were investigated and the results presented in this research.

Despite the potential difficulties in the reduction of the Ti component, the maraging steel alloys lend themselves well to the oxide powder processing technique. Additionally, maraging steel compositions have been extensively processed and studied using more conventional powder metallurgy techniques such as hot isostatic pressing. This is because the high alloy content of these alloys risks segregation of alloying elements during melt processing. Several studies have shown that maraging alloys produced by powder metallurgy methods perform as well as alloys produced by conventional techniques.[14,15,16] Thus, there exists a body of work that allows for more direct comparison of the oxide powder processed maraging steel to the conventionally processed alloys.

Three maraging grades were chosen for this study; maraging 400 (M400), maraging 350 (M350), and maraging 200 (M200). The numbering of the alloys refers to the approximate yield strengths of the maraging compositions, 400, 350, and 200 ksi, respectively. The nominal compositions and mechanical properties of these alloys are given in Table 3.1.[17,18] These alloys possess very high yield strengths, but still maintain good ductility with elongation values ranging between 6 and 10 percent.

Super Invar

The Super Invar alloy was investigated in order to extend the range of mechanical properties by adding more ductile alternatives. This alloy is a Fe-Ni-Co alloy, which is

not generally considered for conventional engineering structure applications. It is chiefly known for its low coefficient of thermal expansion over a temperature range of approximately 0-100°C.[19] The alloy possesses strengths much lower than the maraging steel, but with a much higher elongation (Table 3.1). [20] The alloy can be strengthened at the expense of elongation through martensitic transformation by cooling below the martensite start temperature reported to be -80°C. This gives an additional range of strengths and ductilities for analysis and allows processing effects of LCA chemo-powder metallurgy to be better validated. The choice of Super Invar also does not deviate significantly from the composition of the maraging steels (Table 3.1). This means that paste rheology and the impurities from raw materials will be common to both systems.

3.2 Experimental

The alloys selected for study in this research were investigated for their bulk properties including microstructure and mechanical behavior. The purpose of the experiments was to characterize alloys made using the oxide powder paste extrusion process to allow comparison to similar alloys made using conventional techniques and to create a database of material properties for use in LCA modeling efforts.

3.2.1 Sample Fabrication

Samples of each alloy system were prepared for testing and characterization. The fabrication of the samples was similar to the technique detailed in Chapter II. Oxide powders in the appropriate proportions were dry mixed with a methocel binder. Liquid phase containing water and lubricant was then added to create a granulated mixture. The mixture was consolidated into a paste using a high shear compounder. The paste was

then available for extrusion through any number of dies of suitable cross-section. All samples were reduced in a flowing hydrogen atmosphere at 1350°C for 2 hours, unless otherwise specified.

Samples for testing the bulk material were extruded in two rectangular strip dies to generate sufficient lengths of flat extrusions for tensile testing and characterization. Two thicknesses were available for testing. Thin strips with a post-reduction thickness of ~0.5 mm were collected and prepared for uniaxial testing. Thick strip with a post-reduction thickness of ~2.7 mm was used for wave speed measurements, hardness, and metallographic analysis.

3.2.2 Uniaxial Testing

Thin strips of oxide paste were collected from the extrusion process for test specimen preparation. The strips were laid flat on wax paper and tensile specimens were stamped from the material using a cookie-cutter apparatus in the shape of the conventional "dogbone." The length and width of the gage section after reduction were 35.5 mm and 4.15 mm, respectively. The cut, green samples were sandwiched between two layers of foam to promote even drying and prevent curling and warping. Prior to thermal treatment the edges of the tensile samples were sanded with 320-grit grinding paper to remove excess material left during the stamping process. All samples were prepared in this manner with the exception of the M350 samples, which had gage lengths cut after the reduction process using wire EDM machining.

Several alloys and thermal treatment schedules were investigated. Super Invar in the as-reduced (annealed) and hardened (liquid N_2 cooled) condition were tested for

uniaxial properties. These alloys were also used to assess processing/porosity effects on the performance of the bulk material. Specifically, a study was conducted to observe the effects of paste preparation on the porosity of the finished material and to quantify the overall effects of porosity on the mechanical properties of the materials. Testing was also conducted with a series of maraging steel grades. M200, M350, and M400 grades were evaluated. Samples of M200 and M350 were prepared with and without Ti additions to determine whether TiH_2 was being incorporated into the alloys as pure Ti. An x-ray diffraction study was also performed on the pure TiH_2 under various conditions to ascertain if the powder was stable through the extrusion process and ultimately through the reduction process. As described previously, maraging steel alloys must undergo an age-hardening treatment to fully strengthen the material. For the alloys used in this study, a thermal treatment of 480°C for 5 hours was used based on common heat treatment schedules found in the review literature.

Uniaxial tests were performed using a screw-drive test frame with a 10,000-pound load cell. Data, in the form of load and crosshead displacement, was collected using computer data acquisition software linked to the test frame. Samples were measured for average length, width, and thickness of the gage section and density was calculated using the Archimedes method. The collected data was converted to engineering stress versus strain and relevant values such as ultimate strength, yield strength, and elongation were determined for each test and averaged. In order to fully characterize the materials for modeling purposes, the engineering stress-strain data was converted to true stress-strain data. From this the values for the strain-hardening coefficient and strain-hardening

exponent could be extracted using the relationship $\sigma = K\varepsilon^n$ for the plastic regime. This information is valuable in predicting the dynamic behavior of the materials.

3.2.3 Metallography and Alloy Characterization

Samples of thick strip extrusion were used for metallographic observation as well as a number of tests that required a larger volume or surface area of material than was afforded by the thin strip samples. Metallographic specimens were prepared for observation using both optical and scanning electron microscopy. Optical specimens were ground and finish polished with 0.5-μm alumina slurry. The surface was etched with a 2% nital solution to reveal pertinent microstructural features. A Leica DM IRM optical microscope with digital image capture capabilities was used to evaluate grain size and identify phases and phase distribution. Scanning electron microscopy (SEM) was used to supplement optical observations of microstructure. SEM was also utilized to observe fracture surfaces of tensile specimens. The energy dispersive spectroscopy capabilities of the SEM were used to determine the extent of homogeneity of the alloys through elemental maps as well as to identify the chemical make-up of features of fracture surfaces.

Additional testing was performed on thick strip samples to complete the database of material properties for oxide paste processed alloys. Hardness values were collected for M200 and Super Invar alloys using a LECO LR-100RD Rockwell-Type Hardness Tester. Rockwell B hardness scale was used for the annealed and hardened Super Invar alloys and the Rockwell D scale was used for M200. A minimum of three tests per sample was conducted on multiple samples of each alloy. Young's modulus data were

collected using sound speed measurements from a NCA 1000 Ultrasonic Analyzer. The apparatus uses probes to send and receive an ultrasonic pulse. The software allows the user to determine the time of flight of the pulse through a sample. This data can be converted to a sound speed if the thickness of the sample is known. Modulus values can be calculated from the sound speed measurements using the following relationships,

$$C_l = \left(\frac{\lambda + 2\mu}{\rho} \right)^{1/2} \text{ and}$$

$$C_s = \left(\frac{\mu}{\rho} \right)^{1/2},$$

where C_l is the longitudinal wave speed, C_s is the shear wave speed, and ρ is the material density. The μ and λ parameters in these equations are related to the modulus by the following relationships,

$$\mu = \frac{E}{\left[2(1+\nu) \right]} \text{ and}$$

$$\lambda = \frac{\nu E}{\left[(1+\nu)(1-2\nu) \right]},$$

where E is the elastic modulus and v is Poisson's ratio, typically assumed to be 0.3 for metals.[21] By using both longitudinal and shear probes and using the relationship $G = E/(1+2\nu)$, the elastic modulus, E, and the shear modulus, G, were determined for the Super Invar and maraging alloys.

Porosity measurements were collected on all samples using the Archimedes method. This technique relies on the buoyancy effect to determine the amount of porosity present. Samples are weighed dry, W_D, and then placed in a container of water.

Vacuum is applied to the container to remove air from open pores. Samples are weighed suspended in water, W_{SS}, and while still saturated, W_S. The following relationships were then used to calculate the actual density of the samples,

$$P_O = \frac{(W_S - W_D)}{(W_S - W_{SS})} \text{ and}$$

$$P_C = 1 - \frac{W_D / (W_D - W_{SS})}{\rho},$$

where P_O is fraction of open porosity, P_C is fraction of closed porosity, and the total porosity is the sum of these two values. Porosity values were calculated based on the theoretical densities of the maraging and Super Invar alloys, given as 8.0 and 8.15 g/cc, respectively.

3.3 Results and Discussion

3.3.1 Microstructural Observations

The reduction of the powder-processed alloys required that the samples be processed in a hydrogen atmosphere at high temperatures. The reduction processes are complete by ~700°C. Thermal treatment to 1350°C is required to insure good sintering and homogenization. At these temperatures both the maraging and Super Invar alloys are austenitic. The high nickel content of the Super Invar alloys, in fact, stabilizes the austenitic phase making it the stable phase at room temperature. The metallographic image in Figure 3.2 shows the single phase, austenitic microstructure of Super Invar that is in the as-reduced condition. Notable features of the microstructure are the 10-20 μm grain size and the distribution of pores throughout. Typically, any further processing of the Super Invar alloy would include cold working for improved strength or, conversely,

annealing treatments to stabilize the microstructure and promote the low coefficient of thermal expansion for which this alloy is known. In this work it was determined that partial conversion of the austenitic phase to martensite would be useful for extending the range of mechanical properties. This was accomplished by cooling the as-reduced samples in liquid-N_2. The resulting microstructure, Figure 3.3, is a mixture of austenite, which is identical to that in Figure 3.2, and Fe-Ni martensite, which appears as the dark, crosshatched region. From point counting, the alloy was shown to be 81.5% converted to martensite. Further cooling to temperatures below that of liquid N_2 would likely have converted more austenite to martensite. Unlike the Super Invar alloy, the stable phase for maraging alloys at room temperature is ferrite. However, due the sluggish kinetics of the Fe-Ni austenite transformation, furnace cooling is sufficient to yield a fully martensitic

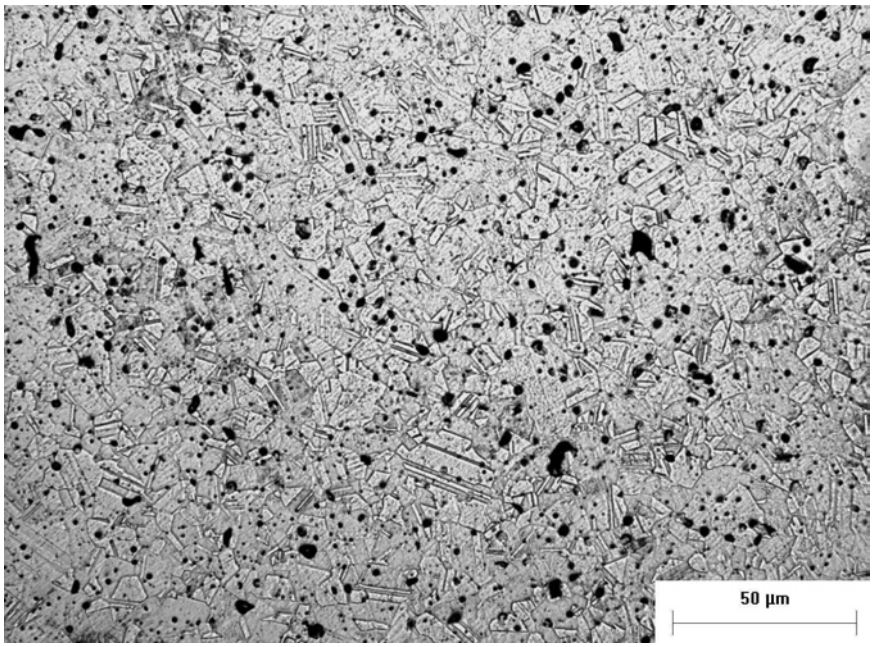

Figure 3.2 – Optical micrograph of oxide powder processed Super Invar alloy in the as–reduced condition showing the fully austenitic microstructure.

structure. This was advantageous to the reduction process since, due to the thermal mass of the furnace, quenching the samples from the soak temperature was not practical.

The microstructure of 200-grade maraging steel is shown in Figure 3.4. The martensitic structure appears as crosshatched lathes with maximum lathe lengths of approximately 20 μm. Since the size of the martensitic structure is dependent on the grain size of the austenite prior to cooling, and, the austenite grain size observed in similarly processed Super Invar of similar composition is approximately 20 μm, the scale of the martensitic microstructure is reasonable. Further observations of the same sample with scanning electron microscopy yield similar images. Precipitate phases were not observed in these images since the scale of these precipitates is in the nanometer range. Energy dispersive spectroscopy of the reduced samples of both alloys also revealed the relative homogeneity of the materials. The homogeneity of the polished specimens was confirmed using the x-ray mapping capabilities of the SEM, i.e. there were no compositional gradients detected at the resolutions capable of this equipment, Figure 3.5.

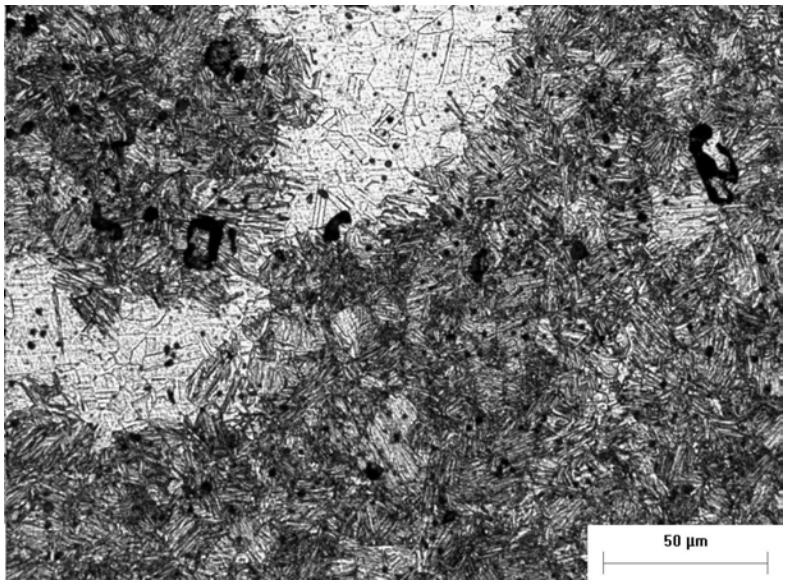

Figure 3.3 – Optical micrograph of oxide powder processed Super Invar alloy in the quenched condition showing the partially converted two-phase microstructure.

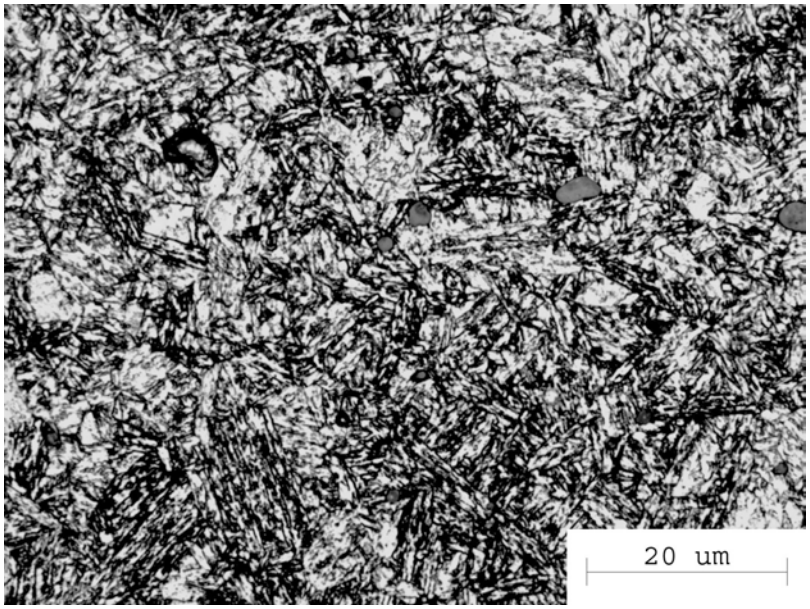

Figure 3.4 – Optical micrograph of 200-grade maraging steel showing the fine martensitic structure after furnace cooling to room temperature.

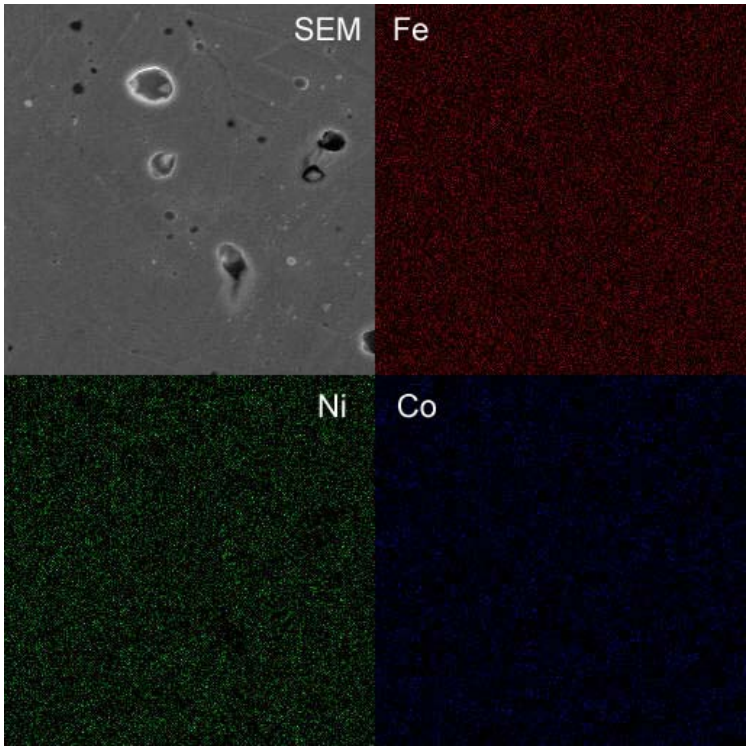

Figure 3.5 – X-ray maps show the relative homogeneity of the Super Invar alloy, 1500x magnification.

3.3.2 Mechanical Properties

Thus far, the bulk alloys produced from the chemo-powder process have been characterized for microstructural features such as size and morphology of phases and porosity. In this section, the mechanical behavior of the alloys will be investigated and compared to the performance of commercially available alloys. Knockdown effects of porosity and incorporation of titanium into the maraging alloys will be discussed as they relate to alloy performance. Testing included uniaxial loading, hardness indentation, ultrasound wave speed, and density measurements. Where available, data for wrought alloys of the same or similar composition are used to evaluate powder processed alloys. Tabulated data for all tests is located in Appendix A for quick reference. These data are also vital in understanding and modeling the performance of cellular alloys as discussed in Chapters IV and V.

Maraging Alloys

Nominal apparent densities measured on the uniaxial test specimens averaged 95% of theoretical density. The source of the porosity was attributed to the inherent porosity associated with powder packing and sintering, and to the presence of extrusion defects. The mechanical data for the fully alloyed specimens, i.e., with Ti additions, is tabulated in Table 3.2. The first composition to be tested was a M350 alloy without the titanium addition. The stress-strain data for this alloy is shown in Figure 3.6. The yield strength data corresponds reasonably well with extrapolated data from research literature which shows similar composition alloys having yield strengths in the range of 1450 MPa.[13,22] It has already been stated that Ti additions to 0.7% can increase yield strengths by as much as 25%. Assuming a linear fit and extrapolating to the 1.4% Ti concentration

for M350 would indicate a potential 50% increase in strength with the addition of Ti to the base alloy. Subsequent M350 compositions were alloyed with titanium through the use of titanium hydride. It was hoped that the hydride would decompose to titanium and not re-oxidize before the reduction process was complete. Samples with the Ti addition were prepared and tested under the same conditions as the no-Ti M350. The mechanical behavior can be compared in Figure 3.6. The data shows a significant increase the yield strength of the titanium-alloyed composition from approximately 1200 MPa to 1500 MPa. However, the increase corresponds only to a 25% increase in the yield strength and it falls short of the strengths given by the wrought alloy properties. The ultimate and

Table 3.2 – Uniaxial properties of chemo-powder processed alloys.

	Mechanical Properties			
	UTS (MPa)	YTS (MPa)	Elongation (%)	5% porosity UTS prediction*
M200	1219	1178	3.5	1129
M350	1662	1522	2.5	1935
Super Invar	397	261	26	223
Super Invar/N_2**	679	414	7	--
*Calculated based on Bocchini and wrought UTS values.				
**Superinvar quenched in liquid nitrogen.				

yield strengths are approximately two-thirds the wrought value given in Table 3.1. If the effects of porosity were taken into account using the Bocchini relationships, predicted strengths could be compared to experimental results (Table 3.2). The experimental results are within 15% of strength values predicted for 5% porosity. Also of note is the low degree of ductility shown in the uniaxial testing. Wrought alloys have been shown to achieve from 6-10% elongation depending on heat treatment. While the effects of 5% porosity are expected to reduce elongation by nearly 40% to a minimum of ~3.5% total elongation, the average strain to failure for the powder processed M350 alloy of 2.5% is

more than 25% lower than predicted values. The low strength and elongation values suggest that porosity is not solely responsible for reduced performance. Investigation of M200 alloy generated similar results.

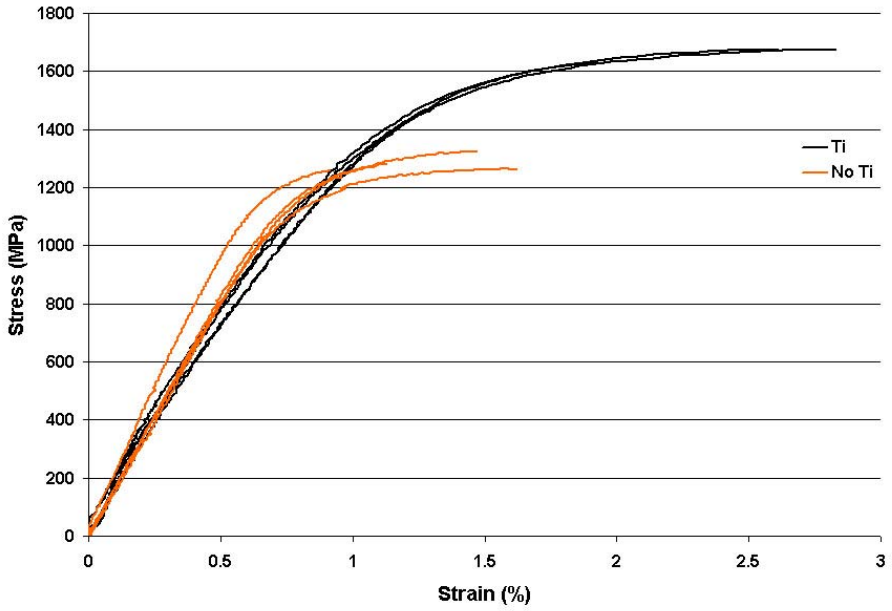

Figure 3.6 – Uniaxial engineering stress-strain response of M350 composition. Use of titanium hydride as a titanium source proves reasonably successful.

The M200 grade maraging steel was also prepared with and without titanium hydride additions, Figure 3.7. As expected, the M200 alloy shows an improved strength response with the addition of Ti. Yield strength is increased by nearly 150 MPa for the addition of only 0.2% Ti in this composition. This is a strength gain of 12.5% whereas the predicted strength gain at this Ti concentration level is only 8%. Strength comparisons to 5% porosity predictions also compare well to the actual results with the yield strength exceeding the predicted value. Elastic modulus determined from sonic wave speed measurements similarly show better than predicted results. Given the modulus of the wrought alloy to be 189.6 GPa, the predicted modulus at an average

porosity of 4.8% is 160 GPa. Wave speed calculations give the actual elastic modulus of the powder processed alloy to be 177.8 ± 7 GPa, which is more than 10% higher than predicted. However, strain to failure again fell short of expectations, averaging only 3.5% rather than the predicted 6%. In an attempt to improve the ductility of the higher strength alloys, the M200 alloy was over-aged by heat-treating at 500°C for 5 hours. The higher soak temperature was expected to increase precipitate size and spacing resulting in increased ductility at the expense of strength. Uniaxial tests results, Figure 3.7, show this to be case. Increased elongations can be achieved with the loss of about one-quarter of the strength. Though the fully hardened M200 alloy was the focus of testing in the remainder of the research to be presented here, the availability of the over-aged M200 will allow flexibility for future application studies with negligible process changes.

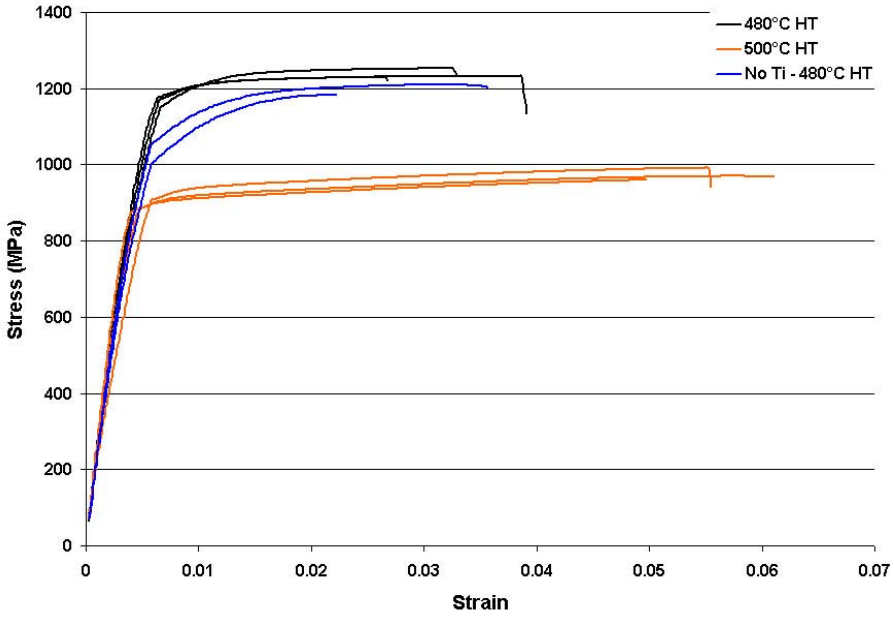

Figure 3.7 – Uniaxial response of M200 based alloy with and without Ti additions, and after over-aging to improve ductility (corrected for machine compliance).

Analysis of Titanium Additions

The strengths for the maraging steel grades are promising for honeycomb applications. However, the higher titanium grade, M350, performs well below expectations even when porosity is taken into account. This suggests that not all of the titanium addition is being incorporated into the alloy during reduction. Because Ti oxidizes so readily, the ability to maintain a furnace atmosphere that is reducing, i.e. having a sufficiently low partial pressure of oxygen, is critical to incorporating elemental titanium into the alloy during processing rather than reoxidizing the material. The stability and reducibility of the hydride alone was investigated to determine at what point the hydride might be decomposing and potentially reoxidizing. X-ray powder diffractometry was used to analyze the powder at three stages of processing. An as-received sample was tested to give a baseline analysis and insure that the raw materials were stable under normal storage conditions. A comparison of the diffraction peaks of the raw material and a standard from the JCPDS is shown in Figure 3.8. Also displayed in the same Figure is the x-ray analysis of a sample of paste-processed hydride. The paste-processed sample was prepared in a similar manner to the typical paste used in this study. A small amount of titanium hydride powder was combined with binder, lubricant, and water, and hand mixed. The wet paste was allowed to sit for an hour before drying at 70°C for 15 hours. The purpose of this exercise was to determine if the hydride was stable in the presence of water, as would be found in the paste, and during drying at elevated temperatures. The dried powder was ground with a mortar and pestle to generate a sample for testing. The results show that the hydride is

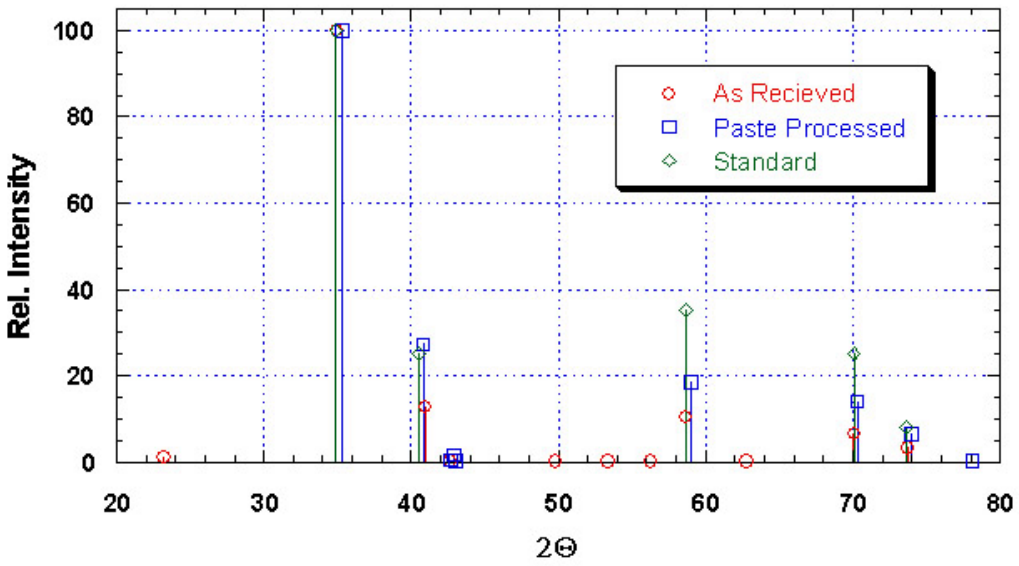

Figure 3.8 – X-ray peaks show that hydride is stable under laboratory storage conditions and after paste processing to a green form.

stable under typical storage conditions and during paste processing prior to reduction. This is significant since changes in raw materials storage or paste processing to accommodate such as small percentage component would likely be prohibitive in terms of time and cost.

It remained to be determined whether the paste-processed hydride powder could be reduced to pure titanium during a typical firing cycle in the atmosphere furnace. The same sample of paste-processed hydride was heat-treated to 1350°C for a two-hour soak in a flowing hydrogen atmosphere. Prior to firing, the furnace chamber was placed under vacuum and backfilled with hydrogen multiple times to insure the cleanliness of the atmosphere. The results of x-ray analysis are shown in Figures 3.9 and 3.10. The data for the processed material is compared to the JCPDS standard for pure Ti in Figure 3.9. There does not appear to any correlation between the data suggesting that the hydride does not remain elemental titanium upon decomposition, but reoxidizes instead. The

identification of an oxide form of titanium is confirmed in Figure 3.10. In this plot the data is compared against standards for TiO and TiO_2. The data show that the hydride was converted to the brookite form of TiO_2 during thermal processing. Brookite is an allotrope of TiO_2 possessing an orthorhombic crystal structure unlike the more common rutile that is tetragonal. Based on these findings it is a high probability that some portion of the TiH_2 addition in the high Ti-content alloys, such as M350 and M400,

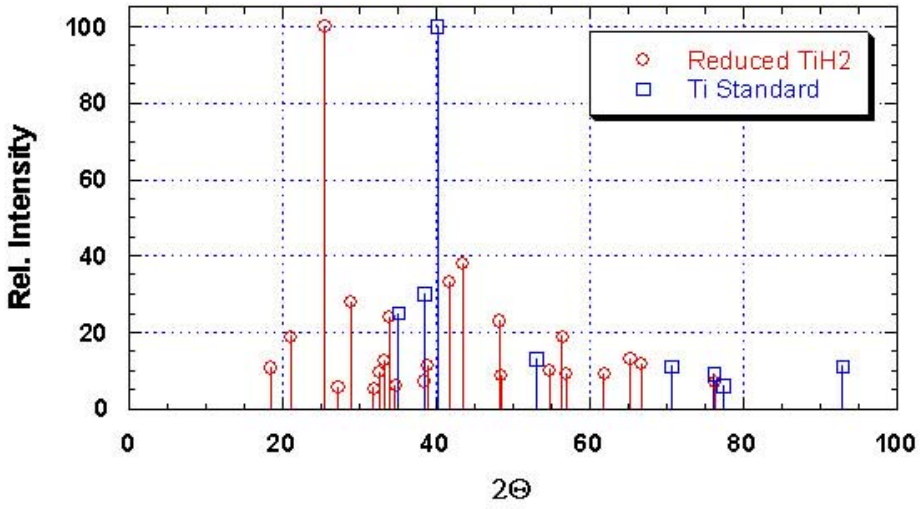

Figure 3.9 – X-ray data for heat-treated TiH_2 powder does not show the presence of elemental titanium.

is partially reoxidized during thermal processing and not fully incorporated into the alloy as elemental titanium. Oxygen concentration tests performed on samples of reduced maraging alloy also bears this out. Samples of M200 without Ti, M200 with Ti (0.2 post reduction wt%), and M400 with Ti (1.1 wt%) were tested on a LECO TCH600 to determine oxygen concentration. The results show increasing amounts of oxygen with increasing additions of titanium. A baseline oxygen content of 0.187% was determined for the M200 alloy processed without titanium. The oxygen content increased to 0.392%

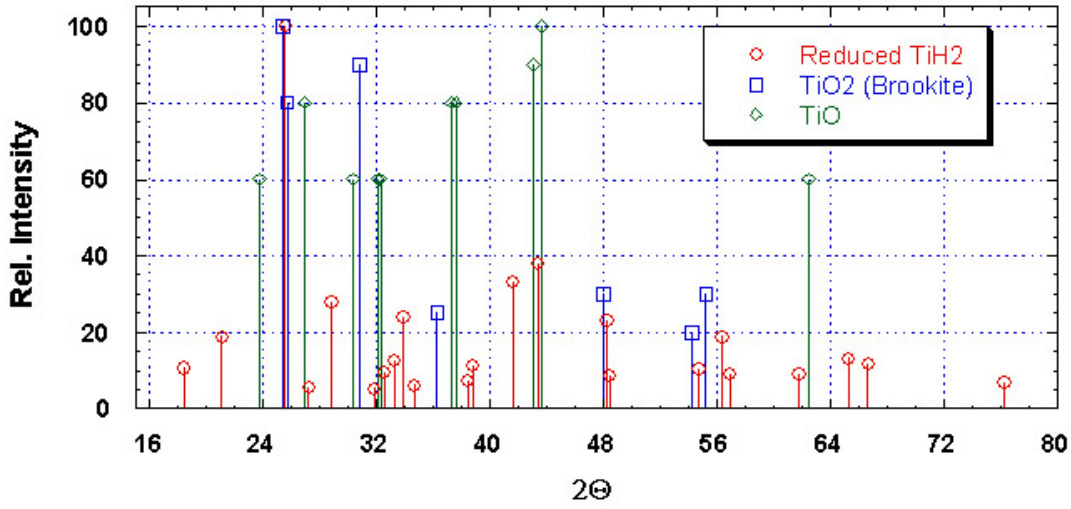

Figure 3.10 – X-ray identification shows that heat-treated TiH_2 was converted primarily to TiO_2 (Brookite).

for 0.2% Ti and 0.792% for 1.1% Ti. The correlation between oxygen content and titanium content is a good indicator that titanium is reoxidizing to a degree during thermal processing. It is also important to note that the decomposition of titanium hydride occurs at ~400°C according to MSDS while the bulk of the oxide powders, most significantly Fe_3O_4, used in the composition does not fully reduce until ~600°C. This means that titanium may act as a reducing agent to the surrounding oxide materials leading to the preferential oxidation of the titanium. XRD was also performed on two maraging samples in attempt to identify the presence of Ni_3Ti that should evolve from the aging process. A reference sample of billet maraging steel and a chemo-powder processed steel were analyzed over a 2Θ range of 22 to 97° for characteristic peaks. The samples exhibited similar peaks with a small degree of peak shift in the powder-processed sample. Identification of the Ni_3Ti precipitates in both samples proved inconclusive due to peak overlap of the high intensity matrix peaks and missing

secondary peaks. While evidence does support that Ti was being oxidized during thermal processing of higher concentration alloys such as M350 and M400, the strength gains that have been shown in the alloys containing Ti suggest that a significant amount of titanium was remaining in the bulk and that the use of TiH_2 was a reasonable success.

Analysis of Fracture Surfaces

Further investigation into the performance of maraging alloys included a detailed look at specimen fracture surfaces. As discussed previously, the strain to failure values suffer greatly from the presence of porosity. The maximum elongation for all maraging specimens aged to maximum hardness did not exceed 3.5%. While porosity is assumed to be responsible for the significant ductility loss, an investigation of the fracture surface was undertaken to seek additional reasons for the low tensile elongation values.

Scanning electron microscopy was used to investigate the details of the fracture surfaces. The fracture surface of an M200 specimen is shown in Figure 3.11. The micrograph was representative of the M350 surface as well. Features of note in this micrograph are the dimpled surface, and the presence of large pores and second phase particles. The dimpled surface suggests that, despite low elongation, the specimen exhibited significant local ductility. Intergranular failure was not observed in any of the maraging steel specimens. The large pores are consistent with air trapped in the paste during extrusion. These pores cannot be removed by sintering and effectively reduce the loading area causing the specimen to fail at lower loads. Improved vacuum de-airing of the paste prior to or during extrusion can reduce the overall volume of these pores and ultimately improve alloy performance. The second phase particles are, in this study,

common to both the maraging alloys and the Super Invar alloy processed using the oxide raw materials in this study. The particles are associated with dimples and range up to several microns in diameter. Energy dispersive spectroscopy (EDS) analysis of some of the larger particles indicates concentrations of silicon, titanium, and aluminum. Since titanium was an intended alloying element in the maraging alloys, its presence is justifiable. The presence of silicon and aluminum is linked to impurities in the raw materials. The supplier's assay of the magnetite powder used in processing the alloys lists several impurities including silica, alumina, and titania. Hence the baseline oxygen

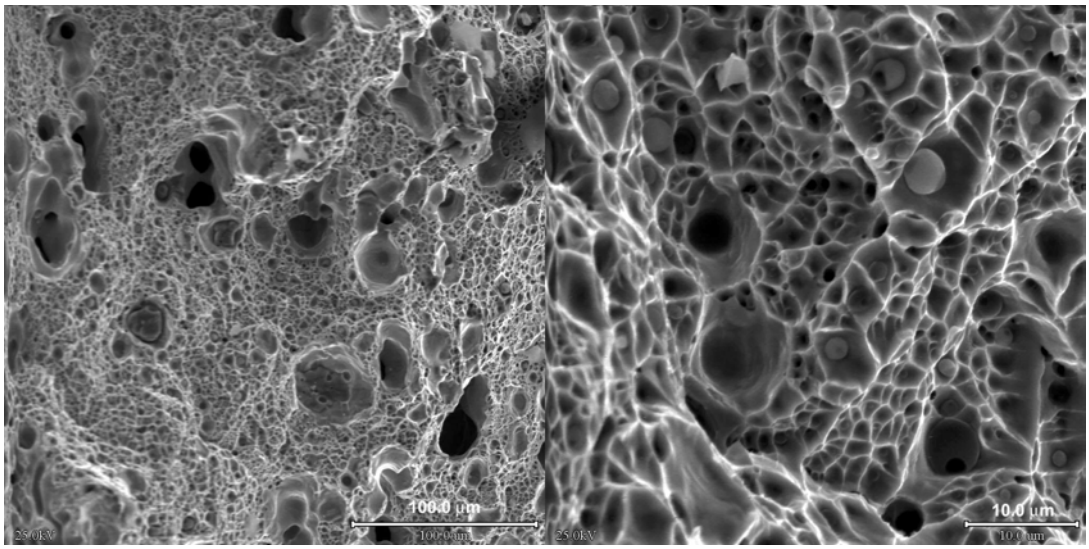

Figure 3.11 – SEM micrographs show the fracture surface morphology of a M200 alloy after uniaxial testing. Dimpling, second phase particles and large pores characterize the surface.

concentration tests for the M200 alloy without titanium registered more than just trace amounts. Based on the EDS information and the powders chemical makeup, it was determined that the particles were an oxide complex of several raw material impurities. The particles appear to play a part in the failure of the specimens since they appear throughout the fracture surface. German and Smugeresky report Ti-rich precipitates segregating at prior particle boundaries (Figure 3.12) to be responsible for the loss of

ductility in HIP samples of 250 grade maraging steel.[23] The size of these precipitates was in the 0.5-1.0 μm range and they were also associated with dimpling. To what degree the larger particles found in this study degraded mechanical performance beyond the effects of porosity alone was undetermined.

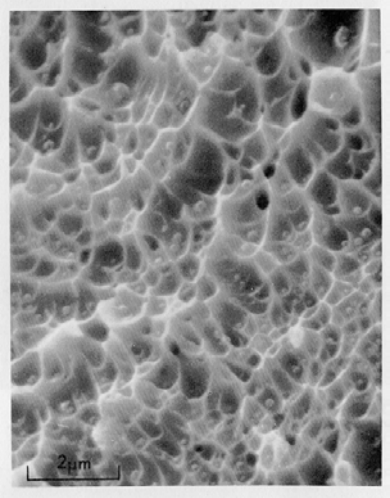

Figure 3.12 – A similar micrograph as reported by German and Smugeresky show Ti-rich precipitates in HIP samples of a maraging 250 alloy.

Super Invar

The Super Invar alloy was processed in a similar manner to the maraging alloys and the resultant 95% average apparent density was expected. Similar low-expansion Fe-Ni alloys have been processed by more traditional powder metallurgy means to yield similar densities. Thomas and Jones report 5% residual porosity for Fe-Ni powder metal alloys compacted to 30 tons/in^2 and heated to 1350°C for 3 hrs.[24] Much of the data available for Super Invar pertain to its low expansion properties rather than mechanical. Since the as-reduced Super Invar was processed to 1350°C, the mechanical properties should be very similar to the annealed properties given in technical specifications for the

alloy by Carpenter Technology Corporation and presented in Table 3.1. Properties for the partially transformed alloy are not available for comparison since this condition destroys the expansion properties for which the alloy is typically sought. Also, the relatively high percentage of retained austenite is not desirable since it promotes variability in local properties. The mechanical properties as determined by uniaxial testing and sonic wave measurements are presented here.

The tensile data for the Super Invar alloy in the as-reduced and the partially transformed condition are shown in Figure 3.13. The data are tabulated in Table 3.2.

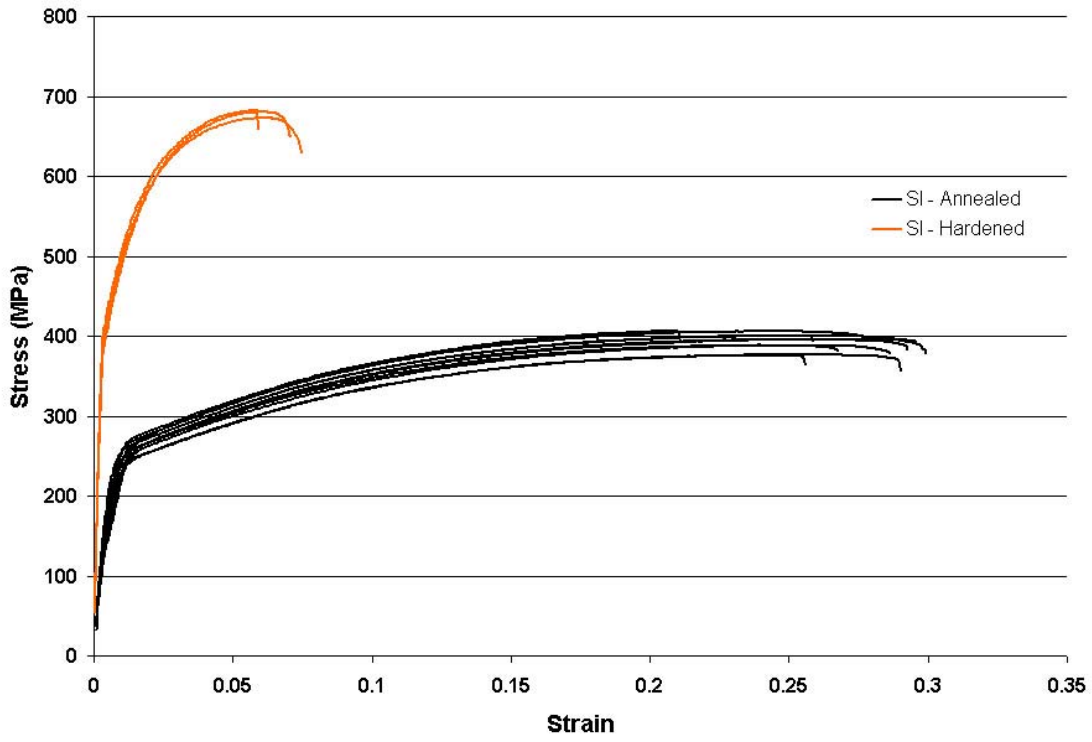

Figure 3.13 – Engineering stress-strain behavior of Super Invar in the as-reduced and partially transformed conditions (corrected for machine compliance).

Mechanical property values for strength and ductility of the as-reduced Super Invar alloy exceed published data when 5% porosity effects are taken into account. Ultimate strength falls within 2% of values predicted by Bocchini's relationships, while yield

strength and elongation to failure exceed these values by 17% and 10%, respectively. Similarly, elastic modulus as determined by wave speed calculations was 5% higher than predicted. Given a modulus of 144.8 GPa for the wrought alloy, the predicted value for the samples tested with an average porosity of 7.2% is 116.7 GPa. The average measured value was 122.1 GPa.

Mechanical properties for the partially transformed Super Invar alloy show much higher strength values and lower overall strains to failure than its as-reduced counterpart. This is due to the large volume of austenite that has been transformed to martensite on cooling to liquid N_2 temperatures. Ultimate and yield strengths of 679 and 414 MPa, respectively, were achieved from uniaxial testing. Fracture strain suffered, however, as the less ductile martensite phase reduced strain to failure to 7%. The partially transformed nature of the alloy was also apparent during hardness testing which showed increased scatter over the course of multiple tests. Elastic modulus of hardened Super Invar was 127 GPa with a standard deviation of 6.5.

A representative fracture surface of the Super Invar alloy is shown in Figure 3.14. Like the maraging steels, the fracture surface was characterized by dimpling, large pores, and second phase particles throughout. The dimples point to ductile failure expected of the as-reduced alloy. The large pores are associated with extrusion defects which could not be removed by thermal treatment alone. The second phase particles have been discussed previously with respect to the maraging steels. Their presence in the Super Invar composition, which does not require titanium additions, further amplifies the conclusion that impurities in the raw materials are playing a role in the fracture of these samples.

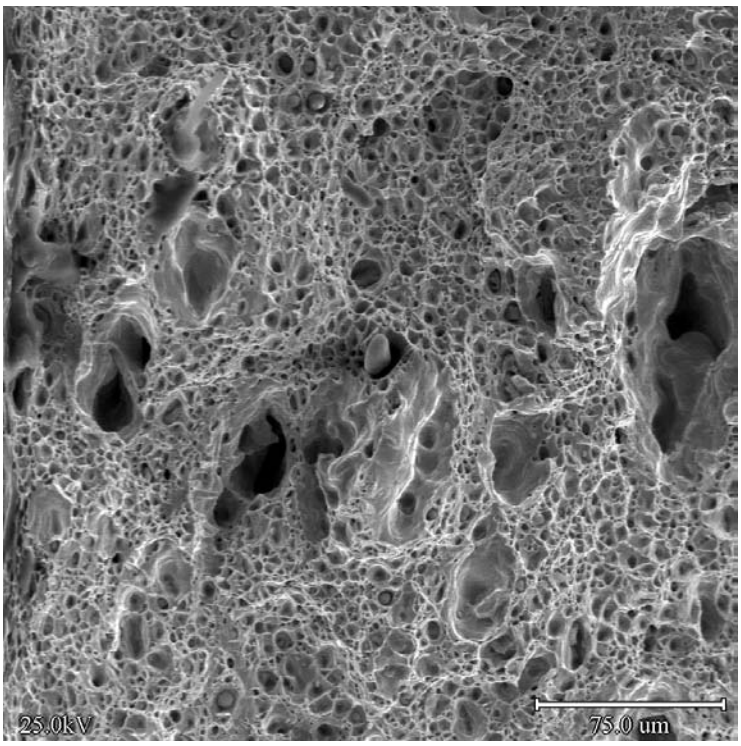

Figure 3.14 – Fracture surface of as-reduced Super Invar alloy after uniaxial testing showing the dimpled nature of the ductile fracture. Second phase particles and large pores from extrusion defects are also present.

3.3.3 Porosity and Paste Processing Relationship

Powder processing methods such as those used in this study are expected to generate products with some degree of porosity. This is a result of sintering, packing efficiency of the powders, and frequency of extrusion defects. While sintering is a concern, the driving force for sintering is dependent on the materials used and thermal processing. In the case of chemo-powder processed materials, the powders are reduced to metal at relatively low temperatures and sintered at high temperatures. Thus, small particle sizes, the metallic nature of the material after reduction, and the high temperature soak combine to give near fully dense materials. Consequently, if further improvements

to sintering were desired, sintering aids such as a liquid phase would have to be considered. Improvements in porosity reduction may also be accomplished through proper paste processing techniques. In the following section paste compounding during processing is discussed as it relates to particle packing and extrusion quality. Super Invar paste and YSZ paste were studied after being mixed under different conditions. The purpose of using YSZ in this study is to compare how processing effects ceramic materials as opposed to metallic materials. The pastes were compounded using three methods that varied the degree of mixing using high and low shear rates, provided by a Buss mixer and Brabender mixer, respectively and increased mixing times by adding a second pass in the Buss mixer. Rheology of the pastes was characterized and green and fired extrusions were analyzed.

Binder Segregation

The results of paste rheology characterization are presented in Table 3.3. The yield strength, σ, and the wall shear strength, τ, are given for each compounding method. YSZ and Super Invar pastes compounded in the Brabender mixer show the highest paste yield strengths and wall shear strengths. The Buss Single Pass method produces the lowest overall paste mechanical properties, and the Buss Multi Pass method produces paste with intermediate properties. Given that paste batches for each composition have identical solids loadings and lubricant, these results point to the degree of compounding and homogeneity available from each method. The Brabender mixer does not generate shear rates sufficient to adequately compound and homogenize the paste. This results in higher than expected rheological properties. The Buss mixer performs significantly better with paste properties 30-50% lower than the Brabender. When comparing single

Table 3.3 – Rheology of pastes after mixing under different conditions.

	Brabender	Buss Single Pass	Buss Multi Pass
YSZ			
σ (kPa)	648.4	254.3	438.1
τ (kPa)	44.9	36.4	38.6
Super Invar			
σ (kPa)	880.5	460.8	625.4
τ (kPa)	144.8	92.4	107.8

pass material to multiple pass material in the Buss it is expected that the additional work will result in improved properties. However, this is not the case. Paste mechanical properties increase with additional passes through Buss mixer. This result can be attributed to the additional work and handling when feeding the paste through mixer multiple times. The extended time that the paste is exposed to the ambient atmosphere reduces the liquid content of the paste as drying occurs. Approximately 2-wt% liquid content is lost during the extended handling of the paste between passes. Consequently, solids loading is increased and paste mechanical properties increase accordingly. Additionally, heat is generated in the paste as it is worked over an extended period. This can lead to gelation of the methocel binder and reduced compounding efficiency. Ultimately, this can lead to reduced extrusion quality and defects.

The quality of extrusions produced using these compounding methods gives further insight into their efficacy. The inhomogeneity of paste that is not sufficiently compounded is apparent in Figures 3.15 and 3.16. SEM micrographs of green YSZ honeycomb extrusion are shown in Figure 3.15 and green super invar honeycomb

extrusion are shown in Figure 3.16. In both, there is evidence of inhomogeneous compounding resulting in volumes of unmixed methocellulose. The segregated binder appears as areas of dark contrast under secondary electron imaging. In YSZ samples processed in the Brabender mixer, Figure 3.15, the segregated binder is distributed throughout the cross-section of the extrusion with some areas as large as 40 μm in diameter. Super Invar samples from the Brabender mixer, Figure 3.16, show a similar distribution of inhomogeneities. At higher magnification the nature of the inhomogeneity is more apparent, also shown in Figure 3.16. In this micrograph an area of unmixed methocel approximately 15 μm across is shown surrounded by oxide powder particles. BSE imaging and EDS maps provide further evidence to conclude that the bodies are indeed methocel binder.

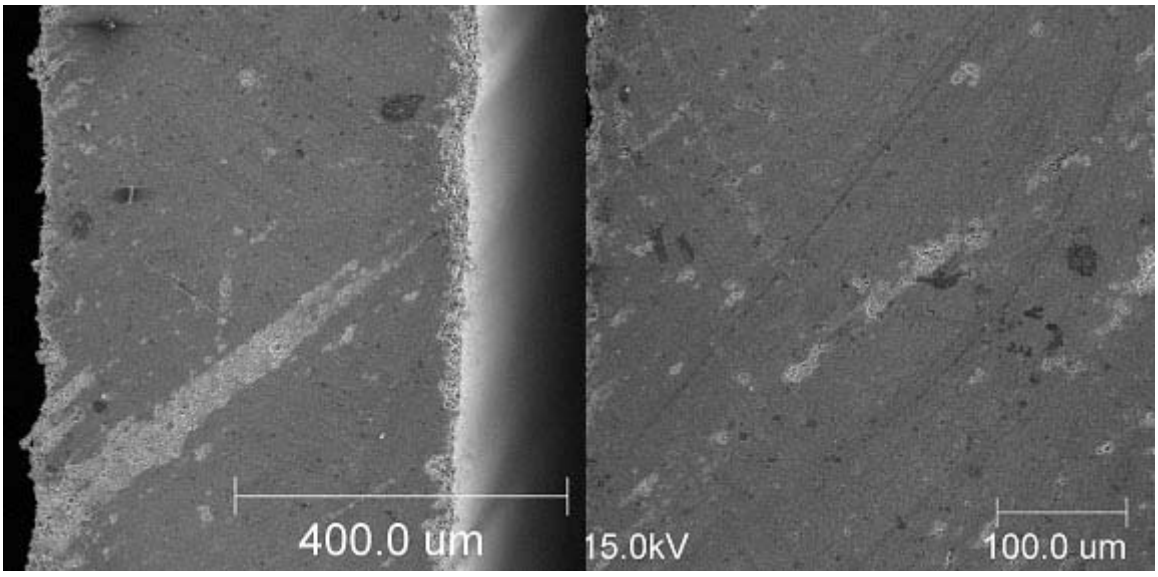

Figure 3.15 – SEM micrographs of green YSZ honeycomb showing inhomogeneities (darker areas).

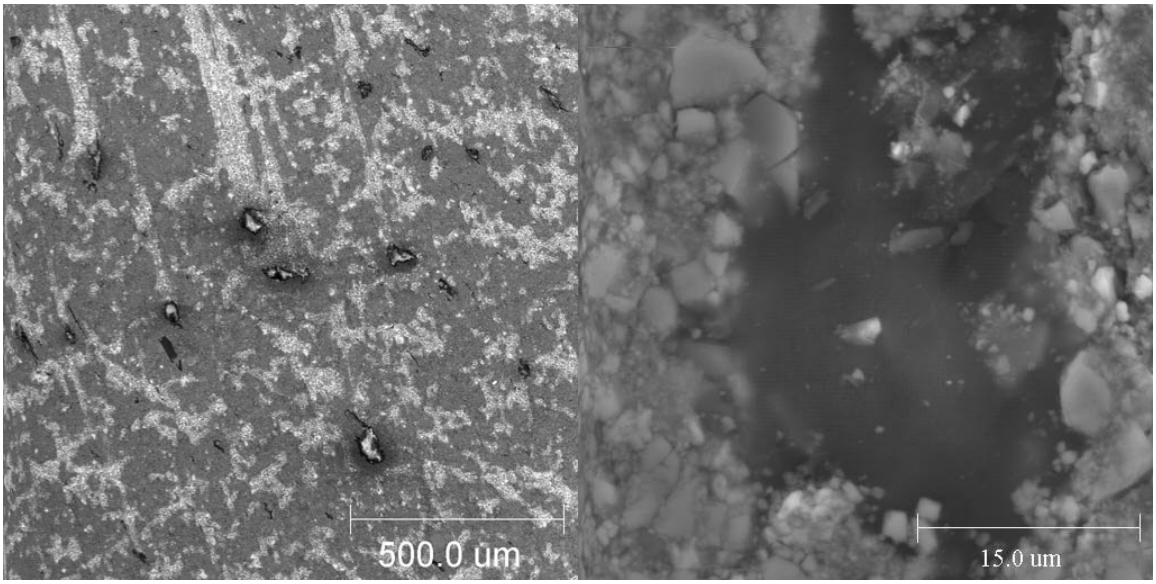

Figure 3.16 - SEM micrographs of green Super Invar honeycomb showing volumes of unmixed methocel.

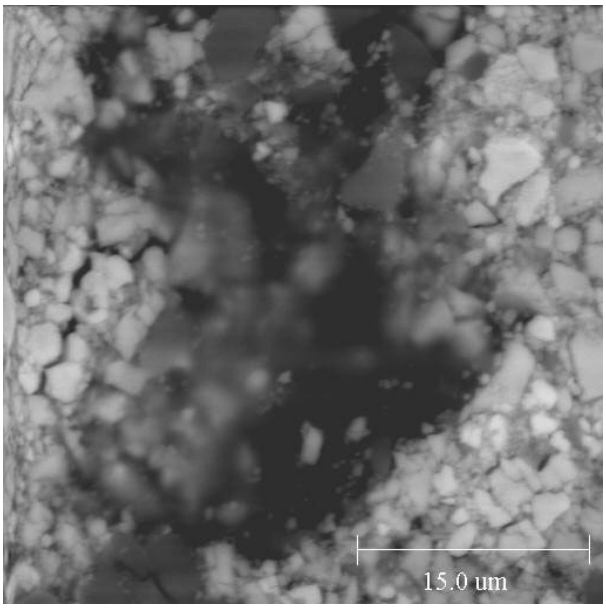

Figure 3.17 – Back-scatter electron image of inhomogeneous region.

The BSE image in Figure 3.17 shows the elemental contrast of the surrounding material with respect to the lighter elements of the methocel. EDS maps similar to that in Figure 3.18 verify that the areas do not correspond to the oxide powders or impurities such as silica or alumina. Investigation of multiple passes through the Buss mixer indicates that the size and frequency of unmixed methocel regions can be reduced with sufficient compounding. SEM micrographs of Super Invar paste compounded multiple times using the Buss mixer are shown in Figure 3.19. Regions of unmixed methocel are very nearly nonexistent on a large scale though occasional regions still persist. Results of the SEM analysis fit well with rheology data from the pastes. Insufficient compounding leads to unmixed methocel, which makes up the liquid phase of the paste. Since a higher volume of unmixed methocel would translate to a higher apparent solids loading, the paste will exhibit higher yield strength.

Poor compounding is also expected to effect overall porosity of fired extrusions. Porosity data for YSZ and Super Invar are presented in Table 3.4. Data for both paste compositions show increased porosity for batches compounded in the Brabender mixer. YSZ from the Brabender is shown to have significant amounts of open porosity as compared to any other batch leading to a total porosity of nearly 15-vol %. This may be attributed to the surface quality of the extrusions for the higher strength paste.

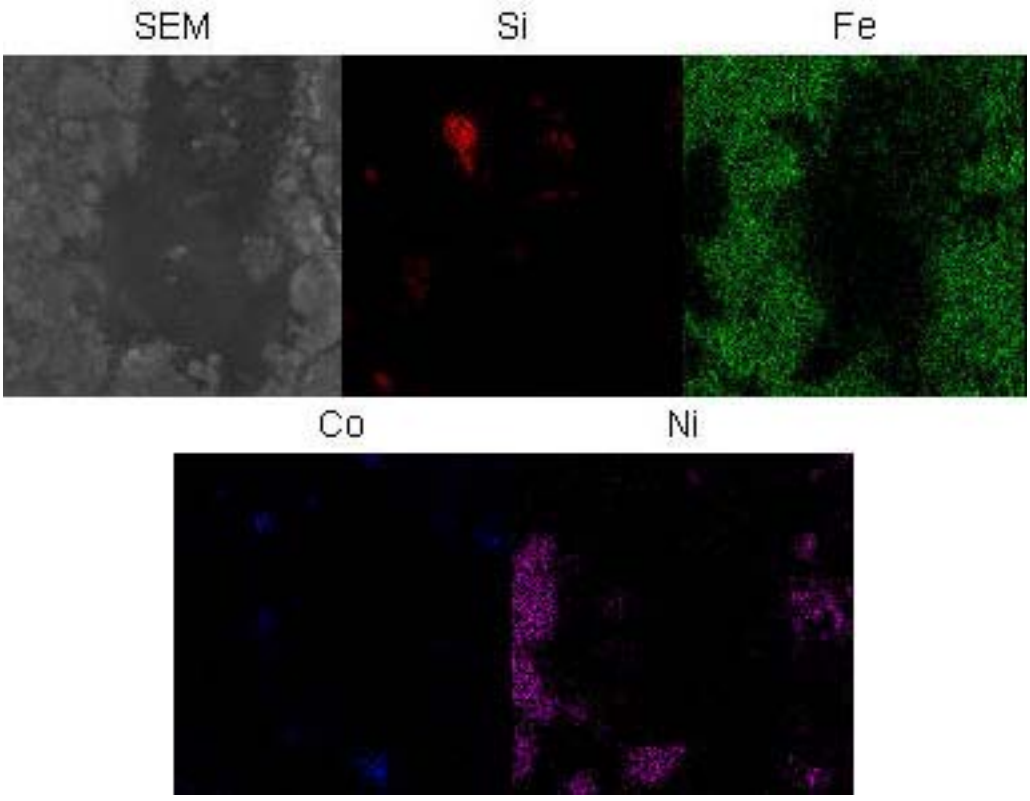

Figure 3.18 – EDS maps show no correlation of suspected methocel with other possible paste components.

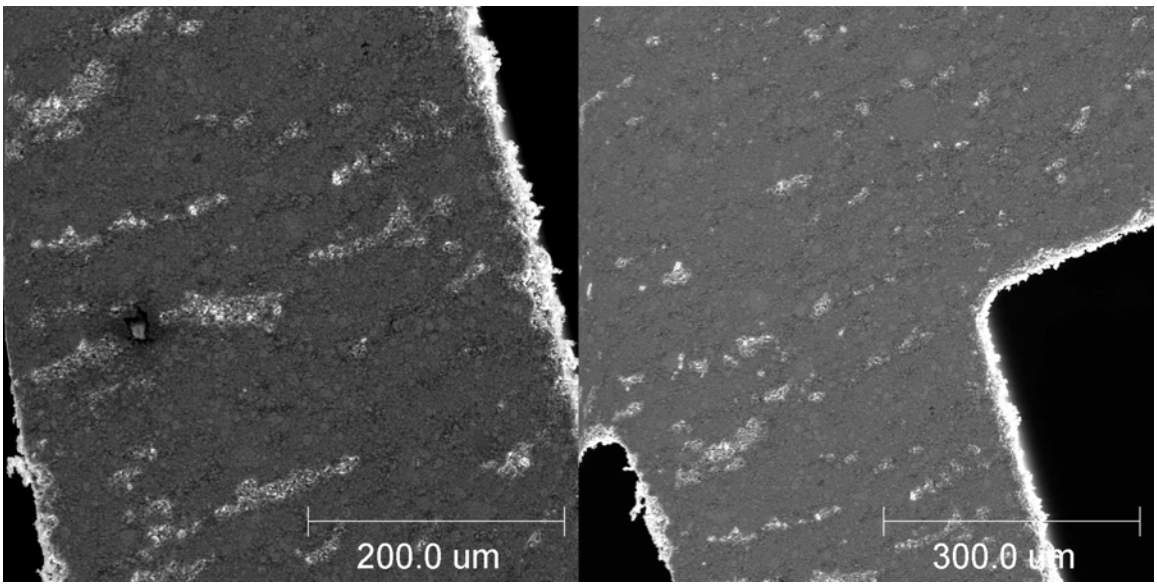

Figure 3.19 – SEM micrographs of green body Super Invar honeycomb showing relative homogeneity of cross-sections.

Table 3.4 – Porosity of samples for different compounding methods. P_O is open porosity, P_C is closed porosity, and P_T is total porosity.

	Brabender	Buss Single Pass	Buss Multi Pass
YSZ			
P_O (%)	5.93	1.05	0.09
P_C (%)	8.81	4.56	3.43
P_T (%)	14.74	5.61	3.52
Super Invar			
P_O (%)	0.58	0.64	0.19
P_C (%)	4.02	2.89	3.78
P_T (%)	4.6	3.53	3.97

A correlation between the unmixed methocel regions described previously and porosity may also be made. Fully reduced Super Invar samples are shown to retain porosity at the sites of the inhomogeneities, Figure 3.20. The micrographs show that the 2-D surface representation of the unmixed methocel volume can be misleading and the volume of the resulting pore much greater than is apparent. Consequently, the mixing method that shows the most inhomogeneities, the Brabender, is also the method responsible for the highest fired porosities.

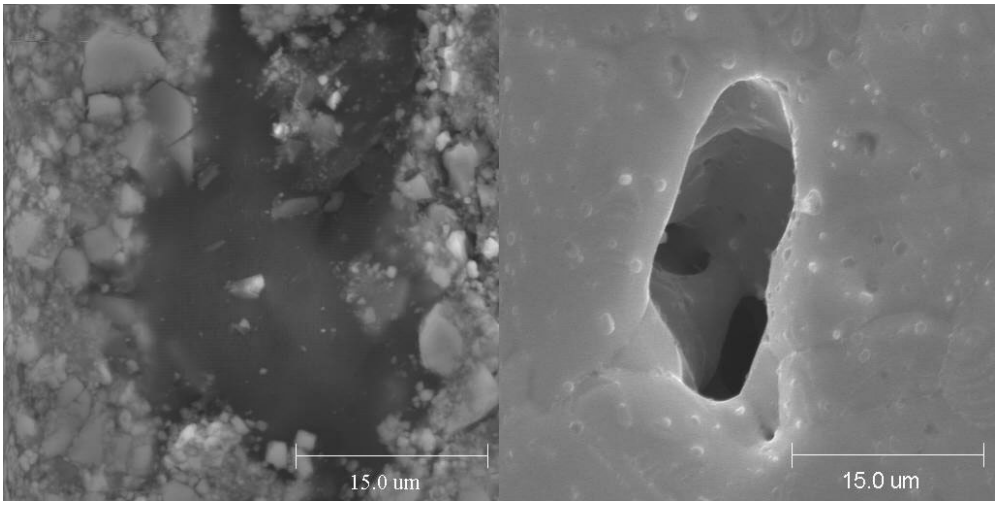

Figure 3.20 – SEM micrographs show the retention of pores in the reduced state associated with unmixed methocel. The associated volume is larger than is apparent in the green state.

Binder Segregation and Mechanical Properties

Mechanical properties of the fired extrusions are also expected to correlate to the compounding process since the final porosity of the body will ultimately determine mechanical performance. Three-point bend data for the YSZ rods are plotted using a Weibull distribution in Figure 3.21. Data for both the YSZ and reduced Super Invar alloy are presented in Table 35. Analysis of the YSZ data leads to no tenable conclusion based on the Weibull modulus of the three compounding methods. Comparison of the average modulus of rupture indicates that the samples produced from Brabender material have a lower strength than the Buss materials. Similarly, Super Invar samples tested in tension exhibit a similar trend in data. Both the ultimate and yield strengths of materials processed in the Buss mixer exceed those processed in the Brabender. Strain to failure, however, does not show this trend. It suspected that the compliance of the test machine artificially increased the overall strain of these specimens. The bulk of the results are not unexpected since porosity is known to degrade mechanical properties.

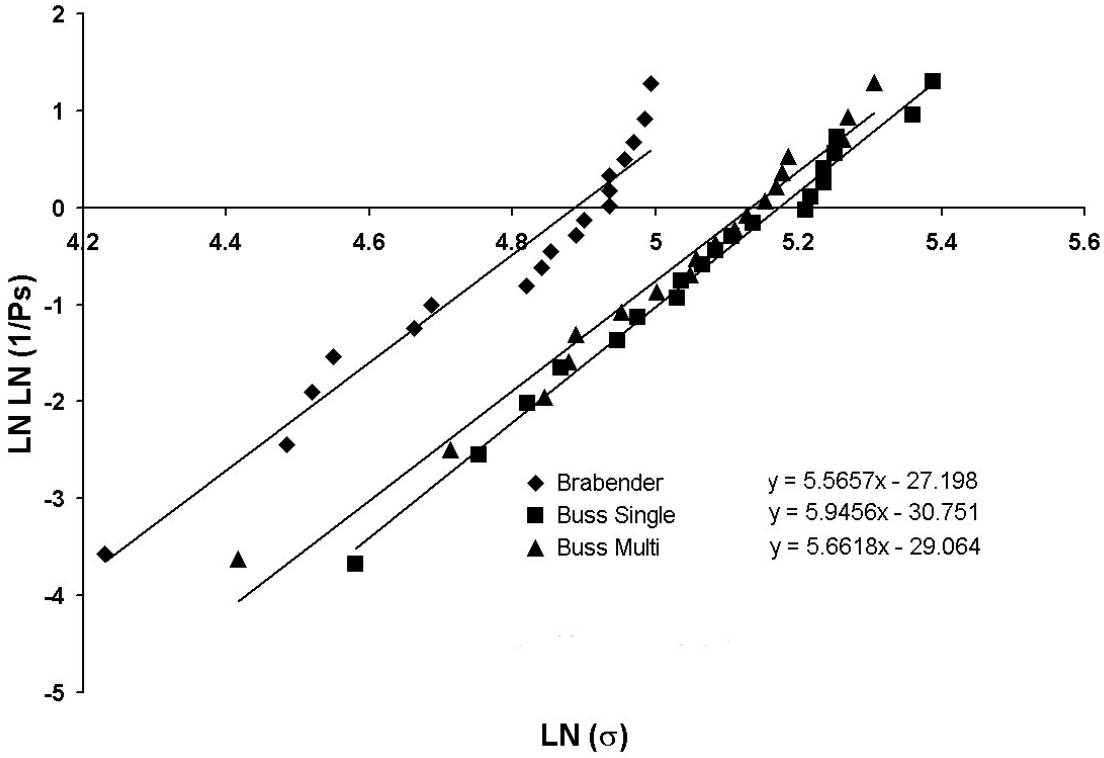

Figure 3.21 – Weibull distribution for three-point bend YSZ 1/8" rods.

Table 3.5 – Mechanical properties for YSZ rod in 3-pt bend and Super Invar strip in tension. 'm' is Weibull modulus and σ is modulus of rupture for YSZ. σ_u is ultimate strength and σ_{ys} is yield strength for Super Invar.

	Brabender	Buss Single Pass	Buss Multi Pass
YSZ			
m	5.657	5.9456	5.618
σ (MPa)	122.3 ± 23.5	163.5 ± 31.9	157±30.2
Super Invar			
σ_u (MPa)	382.5 ± 16.2	396.7 ± 14.3	398.1 ± 18.9
σ_{ys} (MPa)	246.8 ± 8.7	261 ± 1 1.9	266.3 ± 14.9
Elong (%)	29.9 ± 4	26.5 ± 3.6	24.2 ± 7.4

3.4 Conclusions

Alloys fabricated by the chemo-powder process have been characterized and compared to wrought alloys of the same or similar compositions. From a microstructural standpoint, the alloys showed all the features expected. The Super Invar alloys showed the single-phase austenitic microstructure in the annealed condition and the two-phase austenitic/martensitic microstructure in the hardened condition. Similarly, the maraging steel compositions showed the characteristic lathe-type martensitic structure. As expected, porosity was also found uniformly distributed throughout the material. Pores due to extrusion defects were easily identifiable as they were much larger than surrounding pores and often times stretched out along the extrusion direction. Homogeneity of the alloys was confirmed through EDS. No segregation was visible on the length scales resolved by the equipment.

Mechanical properties were investigated and compared to available wrought values. The presence of porosity and the presence of oxide impurities were found to degrade the performance of alloys tested. Measured values were therefore compared to predicted values calculated on the basis of a minimum solid area model. Super Invar in the annealed condition met or exceeded predictions. Super Invar in the hardened condition had no basis for comparison since no data is published on the properties of the partially transformed alloy. The maraging compositions tested showed a dependence on the amount of Ti content in the alloy. The lower Ti content M200 alloy showed good correlation with predicted values. The higher Ti content M350 alloy was significantly lower in strength than predicted. It was postulated that only partial incorporation of the Ti component is occurring due to high probability of reoxidation. This was confirmed

using XRD and uniaxial testing. Because significant strengthening was still achieved with the addition of TiH_2 to the maraging compositions, the hydride was used in all subsequent maraging compositions. Study of the fracture surfaces for Super Invar and maraging alloys revealed consistent, shared features such as dimpling, pores from extrusion defects, and second phase particles. The particles were identified as impurities common to the raw materials.

Paste processing was also shown to affect properties of the bulk materials due to defects associated with extrusions. Poor paste mixing results in a non-homogenous paste not suited to defect-free extrusions. Inhomogeneities in the paste correlated to increased porosity from unmixed binder and defects through poor paste rheology.

The sum of all results presented in this chapter show that chemo-powder processed alloys compare well to wrought alloys when porosity is taken into account. Several steps can be taken to improve alloy properties including optimizing paste rheology and using good judgment in alloy selection. Use of high purity raw materials and good control over furnace atmosphere during reduction and sintering can reduce impurities that may affect overall performance. A comprehensive list of mechanical properties can be found in Appendix A as well as CTE data of annealed Super Invar and M200 alloys for further reference.

Chapter 4

LCA Quasi-Static Compressive Behavior

In this chapter the mechanical behavior of Linear Cellular Alloys under quasi-static compressive loading is investigated. Two honeycomb designs, triangular and square annulus, are evaluated for strength and energy absorption in the in-plane and out-of-plane orientation. In order to better understand the test results, a review of the literature on the performance of cellular materials is presented. Comparisons are made based on predicted values and test results of other cellular alloys found in the literature.

4.1 Mechanical Behavior of Cellular Materials

Cellular materials show great potential for structural applications because of the promise for significant weight savings. Rather than using a solid mass of material, cellular materials offer a scheme for efficient distribution of material in an array of cells. These materials can be capable of achieving the same level of performance of a conventional solid mass, but with the advantage of decreased weight. Consequently, research into the mechanical behavior of cellular materials has investigated the advantages of various cellular materials including foams and honeycomb. Mechanical models for foams and honeycombs are presented here for comparison.

4.1.1 Mechanical Behavior of Foams

Foams have been widely used for a number of applications including sound dampening and filters. Most typically, foams are made of polymer materials that are easily processed at relatively low temperatures. Polymer foams, however, have not presented significant results in terms of high strength capability. With the evolution of metal foam processing, foams have merited serious attention for mechanical applications.

Open/Close Porosity Distinction

The behavior of foams is closely tied to the nature of the pores or cells that make up the structure. The shape, size, and orientation of the cells, as well as the distribution of bulk material in the cell walls, play a significant role in determining the performance of a foam. In particular, the distribution of bulk material in the cell walls is a defining characteristic of the porosity in a foam. When the bulk material is located in the cell edges a strut-like structure is formed. In this case the porosity is termed open and the pores form an interconnected channel. Conversely, when the bulk material is located in the cell walls, an array of closed polyhedra is the result. The resulting porosity is termed closed since each individual pore is closed off to its neighbors. Typically, foams fall somewhere in between these two extremes, possessing both open and closed porosity. The degree of open or closed porosity is believed to have implications as to the mechanical behavior of foams, and, consequently, mechanical models must take this into account.

Gibson and Ashby's model predicts the modulus and yield strength based on the strength of the bulk material and the volume of material in the cell walls. Gibson and Ashby derive the relationship for the elastic modulus as follows:

$$\frac{E^*}{E_s} \propto \frac{G^*}{G_s} \propto C_1\phi^2\left(\frac{\rho^*}{\rho_s}\right)^2 + C_2(1-\phi)\left(\frac{\rho^*}{\rho_s}\right),$$

where E^* and E_s are the Young's modulus of the foam and bulk solid, respectively, G^* and G_s are the shear modulus of the foam and bulk solid, respectively, ρ^* and ρ_s are the density of the foam and bulk solid, respectively, and ϕ is the volume fraction of the solid residing in the cell edges. For an open cell foam 100 percent of the solid resides in the cell edges, or $\phi = 1$. With C_1 close to unity, the modulus of an open cell foam is predicted as:

$$\frac{E^*}{E_s} = \left(\frac{\rho^*}{\rho_s}\right)^2.$$

For a closed cell foam the entire solid resides in the walls of the cell, or $\phi = 0$. Assuming a maximum of 0.5 for C_2 as predicted by the Hashin limit, the modulus of a closed cell foam is predicted as:

$$\frac{E^*}{E_s} = 0.5\left(\frac{\rho^*}{\rho_s}\right).$$

Comparison of these relationships reveals that closed cell foams have a modulus advantage over open cell foams for densities below 50% theoretical. Similarly, the relationship derived for the yield strength is as follows:

$$\frac{\sigma^*}{\sigma_s} = C_3\phi\left(\frac{\rho^*}{\rho_s}\right)^{3/2} + C_4(1-\phi)\left(\frac{\rho^*}{\rho_s}\right),$$

where σ is strength, C_3 is 0.3 and C_4 is 0.35. This gives a relative strength relationship for an open cell foam of,

$$\frac{\sigma^*}{\sigma_s} = 0.3\left(\frac{\rho^*}{\rho_s}\right)^{3/2},$$

while for a closed cell foam,

$$\frac{\sigma^*}{\sigma_s} = 0.35\left(\frac{\rho^*}{\rho_s}\right).$$

Closed cell foams also show a strength advantage over open cell at low densities based on these models.

4.1.2 Mechanical Behavior of Honeycombs

Honeycombs differ from foams in that they show anisotropic behavior dependent on the direction of loading. The nature of honeycombs requires that cells be arrayed in a 2-dimensional lattice with the 3rd dimension being a linear extension of the cells. Consequently, there are at least two distinct orientations tied to the array of linear cells and the mechanical response of each orientation is different. Out-of-plane loading is defined as loading along the linear axis of the honeycomb, i.e. applying a normal load to the planar cross-sections of the honeycomb. In-plane loading refers to loading perpendicular to the linear axis, or loading across the array of cells. Additional distinct orientations are possible in in-plane loading depending on the shape of the honeycomb and the rotation of the array about its axis.

Papka and Kyriakides[25] describe uniaxial compression of honeycombs in out-of-plane or in-plane directions with a stress-strain response typified by three regimes. The first regime is the linear elastic regime indicative of loading material in the cell walls

prior to plastic buckling. The second regime is the plateau region. In this regime bending, buckling, and fracture mechanisms result in deformation to the structure, but load is maintained at a plateau stress as damage is propagated throughout the honeycomb. Typically, loading is uniform throughout the honeycomb until an instability arises that causes localization of damage. Cells collapse along a band and this band is propagated through the sample as adjacent cell walls begin to buckle. For materials with high hardening properties a more uniform collapse has been observed. In this case, the array of cells can be treated as a single cell with an identical stress state.[26] As the cells collapse and cell walls begin impinging on each other, the behavior enters the densification regime. With increasing strain, the honeycomb approaches theoretical density for the cell wall material and behavior approaches that of the bulk material. The compressive response of three materials types is shown in Figure 4.1.

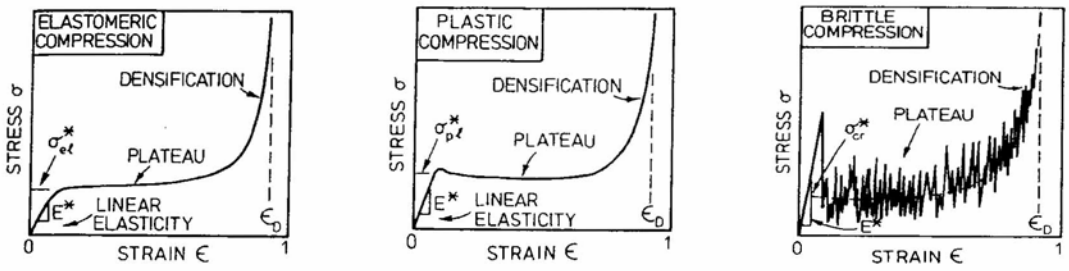

Figure 4.1 –Compressive response of honeycombs as predicted by Gibson and Ashby for three types of materials, [3] p. 96.

Honeycomb Models

Any 2-D cellular array can be used to create a honeycomb. Most typically, honeycombs based on hexagonal, square, and triangular cells are reviewed in the literature. Gibson and Ashby[27] give extensive treatment to the modeling of hexagonal honeycombs. Like foams, the mechanical properties of honeycombs are dependent on

relative density. However, rather than use a density ratio to express the relative density of the honeycomb, two parameters of the honeycomb cell, the cell wall thickness and the cell web length, are used in the models. The parameters are related to the relative density based on the geometry of the cells. For a regular hexagonal cell honeycomb Gibson and Ashby calculate that the relative density $\left(\frac{\rho^*}{\rho_s}\right) = \frac{2}{\sqrt{3}}\left(\frac{t}{l}\right)$ assuming small deformations and negligible geometry changes, where ρ^* is the density of the cellular material, ρ_s is the density of the bulk solid, t is the cell wall thickness, and l is the cell web length. The use of cell wall aspect ratio to define the relative density of honeycombs requires additional second order terms as t/l exceeds ¼ or when strains exceed 20%. This is due to the effects of cell wall joints have a finite volume.

Because of the anisotropy of honeycombs, the loading direction for honeycombs is defined as in-plane or out-of-plane. In-plane loading refers to loading across the honeycomb cross-section normal to the cell axis. Several orientations may also be available in in-plane loading depending on the cellular geometry and in-plane isotropy. Out-of-plane loading is defined as loading parallel to the cell axis.

The elastic moduli of square cell and triangular cell honeycombs for in-plane loading are predicted as a function of (t/l). For square cell honeycombs, the modulus is anisotropic depending on the direction of in-plane loading. The moduli in the loading direction normal to the cell walls is given by:

$$\frac{E_{1,2}^*}{E_s} = \frac{t}{l},$$

where $E^*_{1,2}$ is the elastic modulus of the honeycomb and E_s is the modulus of the bulk solid. In a direction diagonal to the cell wall normal, a relationship of

$$\frac{E^*_{45}}{E_s} = 2\left(\frac{t}{l}\right)^3$$

is given, where E^*_{45} is the modulus at 45° to the cell wall normal. For triangular cell honeycomb, it has been determined that the in-plane modulus is, in fact, isotropic with a relationship given by[28],

$$\frac{E^*_{1,2}}{E_s} = 1.15\frac{t}{l}.$$

Additional relationships have been developed to give a more complete behavioral predictor for both the square and triangular cell honeycombs, including expressions for elastic buckling strength (σ_{el}), plastic buckling strength (σ_{pl}), and shear plastic buckling strength (τ_{pl}). These relationships can also be expressed in terms of (t/l) for the square and triangular cross-sections assuming that $\left(\frac{\rho^*}{\rho_s}\right) = 2\left(\frac{t}{l}\right)$ and $\left(\frac{\rho^*}{\rho_s}\right) = 2\sqrt{3}\left(\frac{t}{l}\right)$, respectively. For square cell honeycombs the following expressions are proposed by Hayes et al[29] and Wang and McDowell[30],

$$\frac{\sigma_{el}{}^*}{E_s} = 0.824\left(\frac{t}{l}\right)^3,$$

$$\frac{\left(\sigma_{pl}{}^*\right)_{1,2}}{\sigma_{ys}} = \left(\frac{t}{l}\right), \text{ and}$$

$$\frac{(\sigma_{pl}{}^*)_{45}}{\sigma_{ys}} = \left(\frac{t}{l}\right)^2$$

where '*' denotes a property of the honeycomb, E_s is the elastic modulus of the bulk solid, and σ_{ys} is the yield strength of the bulk solid. Similarly, for triangular cell honeycombs,

$$\frac{\sigma_{el}{}^*}{E_s} = 3.799\left(\frac{t}{l}\right)^3,$$

$$\frac{(\sigma_{pl}{}^*)_1}{\sigma_{ys}} = \sqrt{3}\left(\frac{t}{l}\right), \text{ and}$$

$$\frac{(\sigma_{pl}{}^*)_2}{\sigma_{ys}} = \frac{2\sqrt{3}}{3}\left(\frac{t}{l}\right).$$

In the case of the triangular honeycomb loaded in plane, there is anisotropic plastic buckling behavior consistent with the orientation of triangular cell rows.

Unlike in-plane behavior, out-of-plane stiffness for LCA honeycombs is simply a linear function of the relative density of the honeycombs regardless of the cell shape. Other out-of-plane properties such as plastic strength have not been extensively investigated. Specific models have been presented by Wierzbicki[31] for hexagonal honeycombs in plastic compression where,

$$\frac{(\sigma_{pl}^*)_3}{\sigma_{ys}} = 6.6\left(\frac{t}{l}\right)^{5/3}.$$

Gibson and Ashby ([27], p.155) have proposed an upper bound for the plastic collapse strength as simply,

$$\frac{\left(\sigma_{pl}^{*}\right)_{3}}{\sigma_{ys}} = \left(\frac{\rho^{*}}{\rho_{S}}\right).$$

This relationship was proposed specifically for axial tension rather than axial compression, but is considered an upper bound for the compression behavior due to cell wall buckling.

4.1.3 Mechanical Comparison of Honeycomb and Foam

Honeycombs hold a definite advantage to foam when considering out-of-plane compressive properties. Out-of-plane performance of honeycombs should be a factor of 3 better than closed cell foam and a factor of 7 better than open cell foam. This is due to the alignment of the cell walls with the axis of loading. A comparison of in-plane honeycomb compressive properties shows that, based on cellular models, honeycomb and foam performance are comparable depending on the cellular geometry of the honeycomb. One review of published cellular material data of a variety of commercially available open and closed cell foams and traditional hexagonal aluminum honeycomb suggests that, based on normalized data, foams can match in-plane hexagonal honeycomb behavior.[32] However, the study admits a large margin of error is possible in its comparison. The data available in the study were taken from published information on several polymer and metal foams and honeycombs that could not be directly compared. The authors extensively document the assumptions required to make comparisons of the dissimilar cellular materials and their bulk properties. Bulk properties of the foam materials had to be extrapolated from the cellular data using a general form of $\frac{\sigma}{\sigma_s} \cong c\left(\frac{\rho}{\rho_s}\right)^n$ to describe the properties of the cellular materials relative to the bulk. The

densities of some bulk polymer materials had to be estimated as well. The limited scope of the study and the comparison of such disparate materials does not significantly challenge the models presented from the literature thus far. A comparison of the honeycomb and foam predictions, Figures 4.2 and 4.3, shows that ideal closed cell foams could be comparable in modulus to square cell honeycombs under in-plane, orthogonal conditions, but give up a 15% strength advantage to square and triangular cell honeycombs under in-plane compression.

The models that have been presented for cellular materials are based on an idealized conception of the cellular structure. In reality, these materials often deviate from the ideal either due to the processing or the presence of defects. For instance, metal foam fabrication does not allow close control over final foam structure and significant variations in properties can exist beyond the scope of the models. Sanders and Gibson have shown that cell wall curvature and corrugation in closed cell aluminum foam can reduce the Young's modulus by greater than a factor of three when compared to the models.[33] Also, non-uniformity of material distribution in cell walls and edges due to processing can result in variable performance due to increased or decreased resistance to bending.[34,35] Similarly, for honeycombs, defects such as holes or inclusions in the cellular array may be present due to processing difficulties. While inclusions have been shown to have little effect on properties, the presence of holes in the honeycomb can have a significant knockdown effect on both stiffness and strength due to early onset of cell wall bending.[36] The effect becomes more pronounced as the size of the hole approaches the cell size or the density of holes is increased.[37] Defects such as holes also act as initiation points for collapse leading to localization of damage. Onset of collapse occurs

at lower loads, but the transition to densification is unaffected for the case of a single defect.[38] Finite element studies have shown that the effect of removing cell walls on honeycomb properties is dependent on cellular geometry. In some cases, such as for square and hexagonal geometries, a precipitous drop in properties occurs with cell wall removal. Triangular geometries show a more gradual fall off in properties.[39]

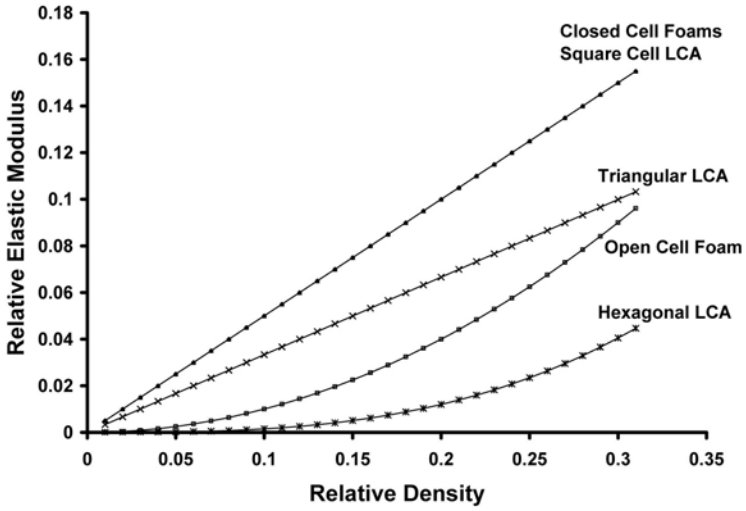

Figure 4.2 – Comparison of the relative elastic modulus versus the relative density of several cellular designs. LCA models are for in-plane loading.

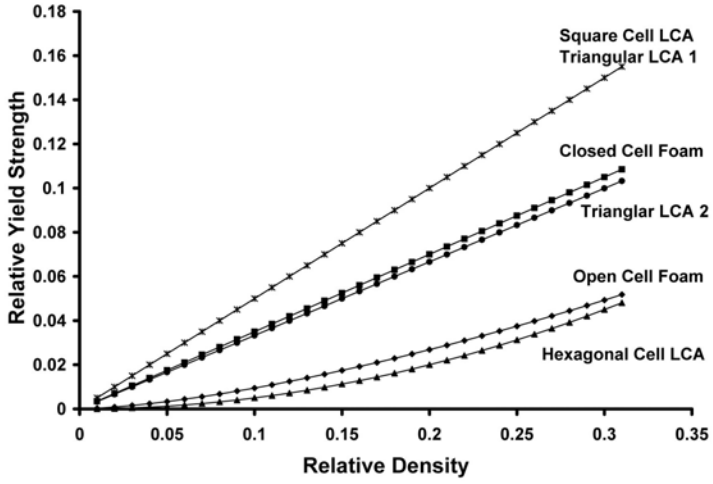

Figure 4.3 – Comparison of the relative yield strength versus the relative density of several cellular designs. LCA models are for in-plane loading.

4.2 Experimental

4.2.1 Sample Fabrication

Two honeycomb cross-sections were used for fabrication of quasi-static compression test samples. A triangular honeycomb, Figure 4.4, and a square annulus with triangular honeycomb walls, Figure 4.5, were extruded and processed using the chemo-powder processing technique. Post-reduction dimensions of the triangular and annulus honeycombs were ~ 21 x 21 mm and 13.75 x 13.75 mm, respectively. Samples of the Super Invar composition were made for testing in the annealed and hardened conditions. The samples of triangular honeycomb were cut to a minimum 1:1 aspect ratio and the square annulus samples were cut to a minimum 2:1 aspect ratio. The choice of aspect ratio was based on possible scale effects in cellular materials. Studies[40,41,42] show that scale effects can occur when specimen size is on the order of the cell size. In

uniaxial compression these effects were shown to be minimized for specimen sizes larger than 7 cells. The number of cells available for in-plane loading was a function of die design and could not be changed to suit these requirements. A diamond cut-off wheel was used to cut the samples and subsequent grinding with 320-grit SiC paper was used to clean the ends of debris from cutting. Care was taken to insure planarity of the cut faces for out of plane loading. Dimensions and weight were collected for each sample to be used in calculations for stress, strain, and density. The Archimedes method was used for measuring density.

4.2.2 Quasi-Static Compression Testing

A screw-drive test frame with a 50,000-pound capable load cell was used to apply the compressive load. Samples were loaded in uniaxial compression for all possible distinct orientations. This included out-of-plane loading, which corresponds to loading parallel to the extrusion axis, and in-plane loading, which corresponds to loading perpendicular to the extrusion axis. In the case of the triangular honeycomb there are two distinct loading orientations for in-plane tests due to the geometry of the design and the orientiation of ligaments perpendicular or parallel to the loading axis. These orientations are displayed in Figure 4.4. A pair of hardened platens was used to prevent damage to the fixtures. The test frame was operated under stroke control to give a displacement rate of approximately 0.25 cm per minute. Computer data acquisition was used to collect load and crosshead displacement data from each test. This data was used to generate stress-strain plots for each sample. Engineering stress values were calculated using the apparent planar cross-section of the honeycomb sample. Engineering strain values were calculated as the ratio of the change in crosshead displacement to the original sample height.

Cumulative energy absorption was calculated for each honeycomb design and loading orientation by summing the rectangular area under the stress-strain curve over discreet strain intervals.

A visual record of the tests was made using a digital image capture system. The system allowed 24 individual frames to be collected from each test at user defined time intervals. The images could then be used to make a time-lapse record of each test to observe the initiation of collapse and the predominant mechanism of failure.

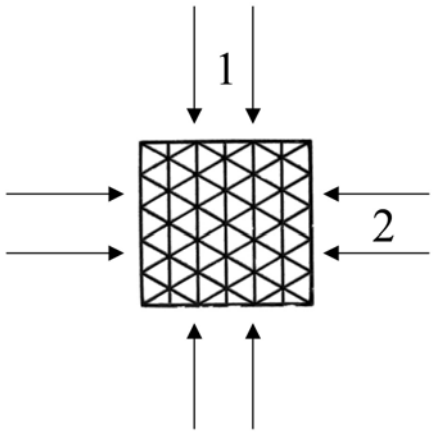

Figure 4.4 – Two distinct orientations exist for in-plane loading of the triangular LCA. Loading in direction 1 orients a large fraction of walls parallel to the loading direction.

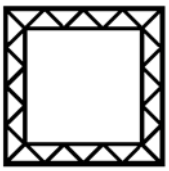

Figure 4.5 – Cross-sectional view of the square annulus LCA with triangular honeycomb walls.

4.3 Results and Discussion

A scanning electron micrograph of the representative cross-section of triangular cells is shown in Figure 4.6. Wall thickness was uniform, measuring approximately 200 μm across. Some small extrusion defects in the form of large pores were visible at the vertex of several cell walls. Samples from both honeycomb designs showed porosity in the bulk material in the range of 9-12%. These values were higher than that experienced in the tensile strip tested in Chapter 3. The higher porosity was attributed to increased error in measuring the saturated weight of honeycomb samples during Archimede's density analysis and the difference in reduction schedule used for the honeycomb. The saturated weight of the honeycomb is intended to determine the amount of open porosity due to retained water in the open pores. The cellular nature of the material makes it difficult to insure excess water is removed from remote areas of the cells. Excess water would ultimately translate to higher apparent open porosity and, ultimately, higher apparent total porosity. Since the honeycomb represented a much larger mass of material as compared to the tensile strip, the heating schedule was adjusted to insure all the components were completely reduced and as much water vapor was exhausted from the system as possible before ramping to the 1350°C soak temperature. This meant adding a hold at 700°C for at least 4 hours to allow complete reduction. It is possible that this partially stabilized porosity through grain growth and incorporation of pores within grains rather than at grain boundaries where diffusion processes associated with sintering are favored. The annulus and triangular honeycomb designs were shown to have bulk densities of ~24% and ~21%, respectively.

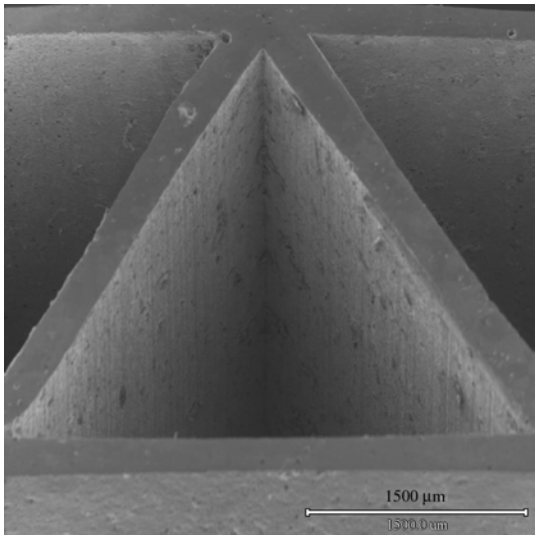

Figure 4.6 – Scanning electron micrograph of triangular cell cross-section showing the scale and uniformity of cell walls.

4.2.1 Performance of Square Annulus LCA

The performance of the square annulus LCA is presented in this section for both the annealed and hardened conditions of Super Invar. Stress-strain data and energy absorption data for in-plane and out-of-plane loading is given and mechanisms of collapse are discussed based on the visual recordings of the compression tests. Visual inspection of samples prior to testing showed some visible irregularities in the LCA specimens. Most notable were intermittent open seams in the interior skin of the annulus. These were defects from the extrusion process that were associated with poor knitting and other paste deficiencies. The presence of these defects was not easily detectable prior to cutting and must be addressed in the analysis of results. Dimensional irregularities were also readily apparent upon visual inspection. Chiefly, warping and bending along the length of the LCA during extrusion processing resulted in non-square cross-sectional geometry. The combination of the low-density structure and handling requirements led to these defects. These particular defects had the potential to promote

mechanisms of collapse not associated with the honeycomb structure alone. The dimensional irregularities were minimized through careful inspection and cutting around areas of high defect concentrations.

Annealed Super Invar Square Annulus

The out-of-plane compressive behavior of the annealed square annulus LCA is shown in Figures 4.7 and 4.8. The stress-strain plot, Figure 4.7, shows the response of the LCA to compressive loading with a high initial peak prior to failure, load drop, and short plateau. The initial loading of the LCA shows two distinct responses. The initial linear-elastic response transitions to a second linear regime at a yield stress of 62.9 MPa. The secondary regime corresponds to the buckling of the cells as the load causes cell wall extension and rotation. A small degree of barreling can be seen in Figure 4.8 (B) at approximately 9.3% strain just prior to load drop. At a peak stress of 99.5 MPa load begins to drop and continues to drop throughout the remainder of the test. In this regime the walls of the annulus were beginning to split and separate from the specimen since their stiffness prevented significant buckling, Figure 4.8 (C & D). Splitting occurred along well-defined lines parallel to the loading axis. The breaks were generally found in the cell walls away from cell vertices suggesting that seams associated with cell wall knitting were the weak link. The continued load drop throughout the remainder of the test was due to propagation of split seams through the length of the specimen, initiation of new seams, and eventually buckling of separated wall sections.

The in-plane compressive behavior of annealed Super Invar annulus LCA is shown in Figures 4.9 and 4.10. The stress-strain response, Figure 4.9, shows a high initial peak with a maximum occurring at 22.9 MPa followed by a load drop and short

stress plateau at approximately 6 MPa. The load drop was associated with initiation of buckling in the walls of the annulus parallel to the loading axis, Figure 4.10 (B). The formation of hinges at the midpoint of the annulus walls and the vertices of the square became more apparent at higher strains, Figure 4.10 (C & D). As deformation continued to higher strains, the buckled walls reloaded as new undamaged sections contacted the platens accounting for the increase in stress as strain approached 40%.

The energy absorption for out-of-plane and in-plane loading of the annealed Super Invar annulus LCA is shown in Figure 4.11. Consistent with the higher overall strength of the LCA in out-of-plane loading, the energy absorption of the LCA was much higher in the out-of-plane direction. At 40% strain, the out-of-plane orientation was capable of absorbing 18 J/cc as compared to only 3 J/cc for the in-plane orientation. Also consistent with stress-strain behavior was the steep initial increase in energy absorption associated with the high initial stress response of both orientations.

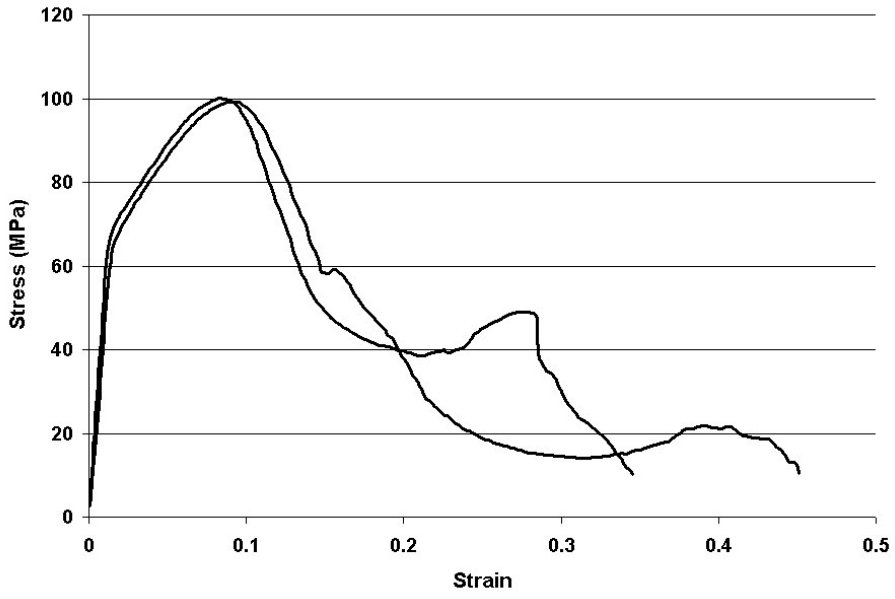

Figure 4.7 – Out-of-plane compression response of annealed Super Invar square annulus LCA.

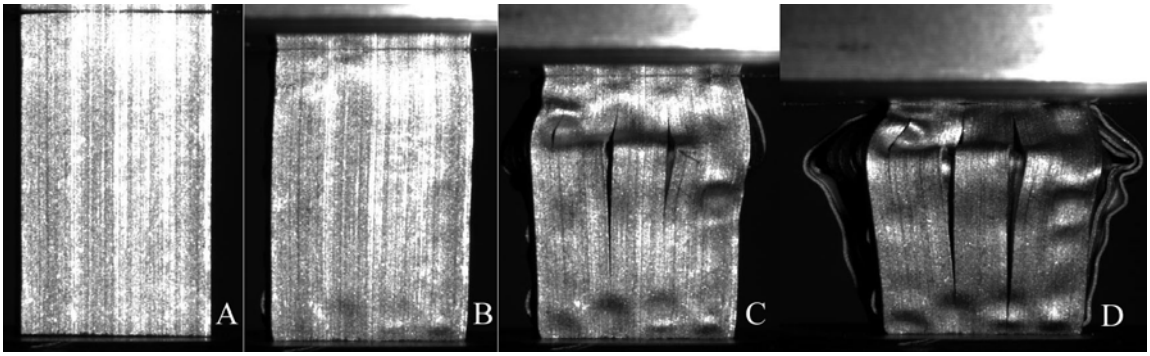

Figure 4.8 – Image capture of out-of-plane loading of annealed Super Invar square annulus LCA. A – 0%, B – 9.3%, C – 18%, and D – 26.7% strain.

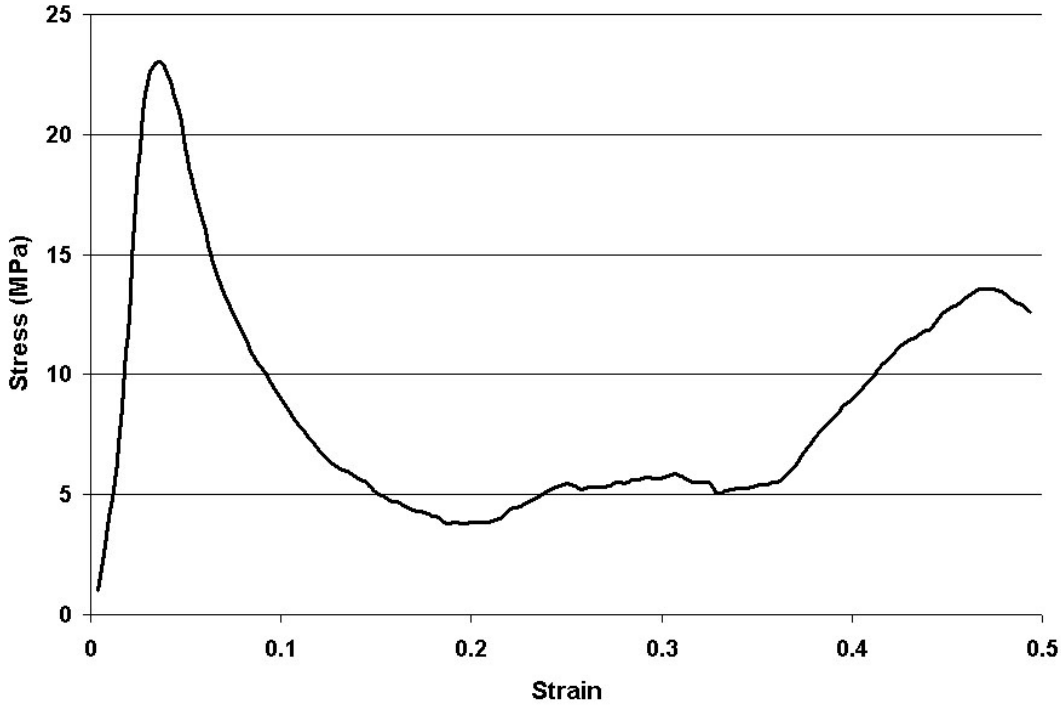

Figure 4.9 – In-plane compression response of annealed Super Invar square annulus LCA.

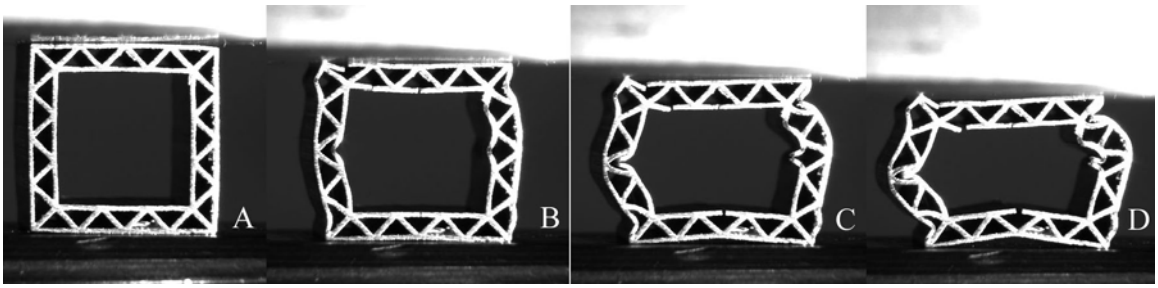

Figure 4.10 – Image capture of in-plane loading of annealed Super Invar square annulus LCA. A – 0%, B – 6.2%, C – 11.4%, and D – 18.6% strain.

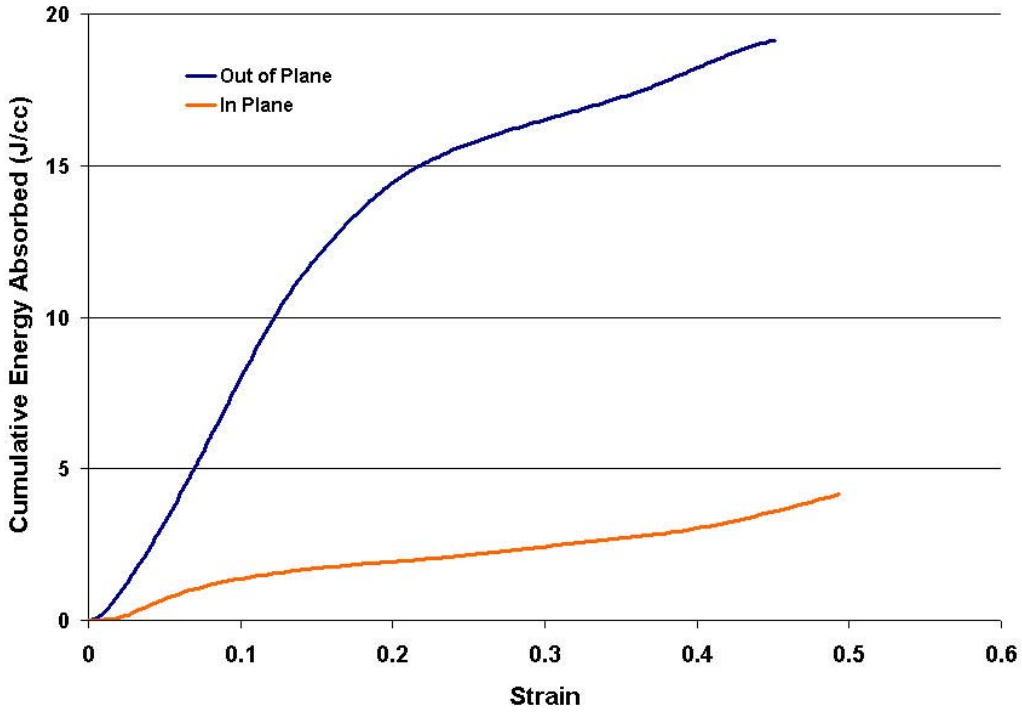

Figure 4.11 – Cumulative energy absorption of annealed Super Invar square annulus LCA under quasi-static compression.

Hardened Super Invar Square Annulus

The out-of-plane compressive response of hardened Super Invar square annulus LCA is shown in Figures 4.12 and 4.13. The response, Figure 4.12, was very similar to that of the annealed condition with the exception of the buckling regime which was less distinct in the annealed condition. The yield stress of the honeycomb was 83.6 MPa and the max stress prior to load drop was 157.4 MPa. While the load drop was significant, the LCA maintained a plateau strength averaging approximately 80 MPa. This was due to a greater percentage of the walls remaining parallel to the loading axis. The LCA experienced similar fractures along the load axis, Figure 4.13 (C & D), as witnessed in the annealed alloy. Walls split and pulled away from the LCA as buckling occurred along the length of the LCA.

The in-plane response of the hardened LCA is shown in Figures 4.14 and 4.15. The LCA achieved a maximum stress of 27.5 MPa before bending began in the walls of the annulus, Figure 4.15 (B). Ultimately, the bending would translate to a shearing across the cross-section of the LCA, Figure 4.15 (C & D). The stress dropped to very low values and did not increase again until the intact walls of the annulus contacted the loading platens once again. The shearing also resulted in termination of the test at low strain values to movement of the sample in the fixture.

Cumulative energy absorption of the hardened alloy was improved over the annealed for the out-of-plane loading condition, Figure 4.16, achieving an energy absorption of 37 J/cc at 40% strain. The in-plane loading condition, however, suffered greatly from the shearing of the LCA and did not meet the values achieved by the annealed condition.

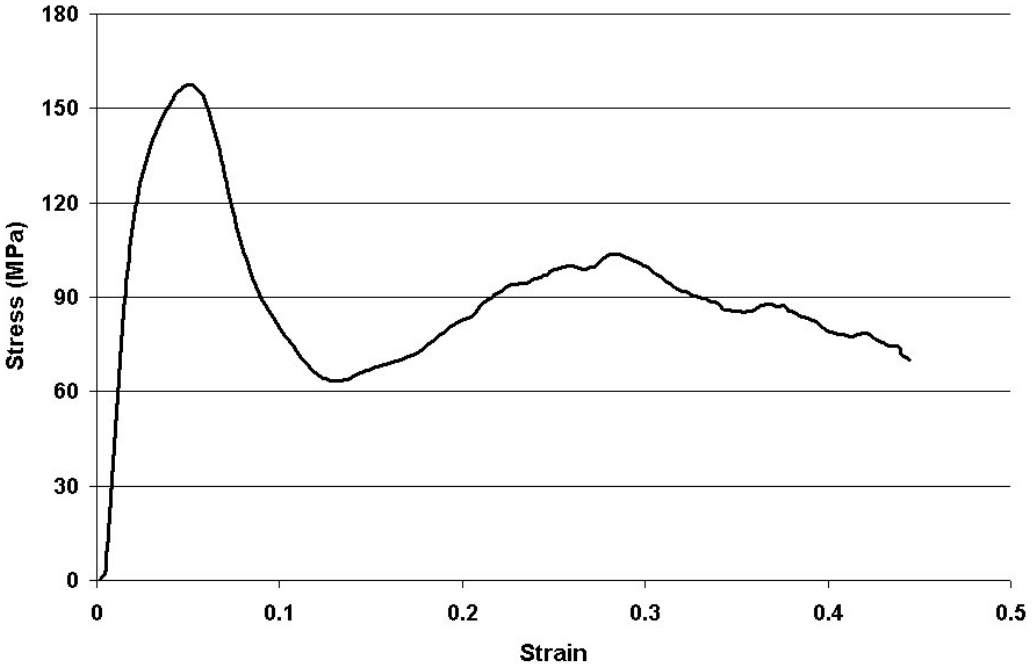

Figure 4.12 – Out-of-plane compression response of hardened Super Invar square annulus LCA.

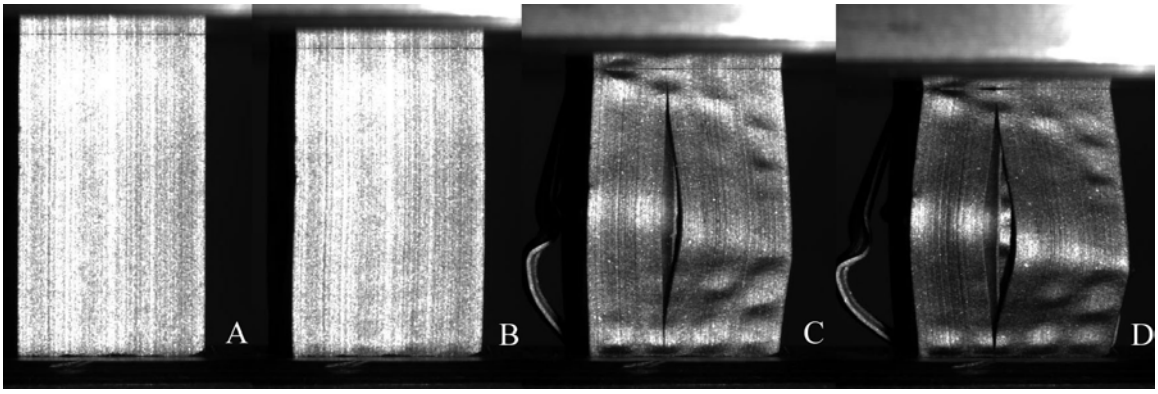

Figure 4.13 – Image capture of out-of-plane loading of hardened Super Invar square annulus LCA. A – 0%, B – 5.9%, C – 11.2%, and D – 16.1% strain.

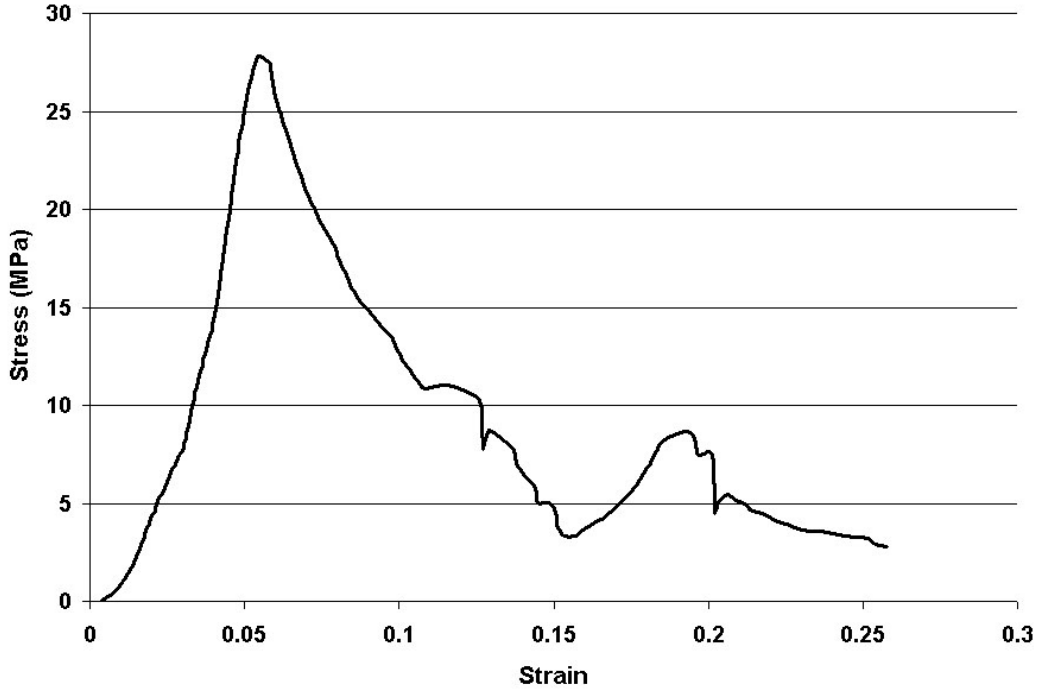

Figure 4.14 – In-plane compression response of hardened Super Invar square annulus LCA.

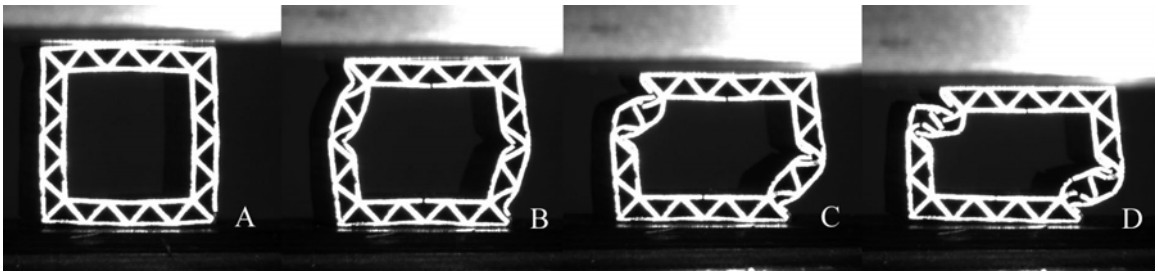

Figure 4.15 – Image capture of in-plane loading of hardened Super Invar square annulus LCA. A – 0%, B – 8.1%, C – 18.2%, and D – 25.2% strain.

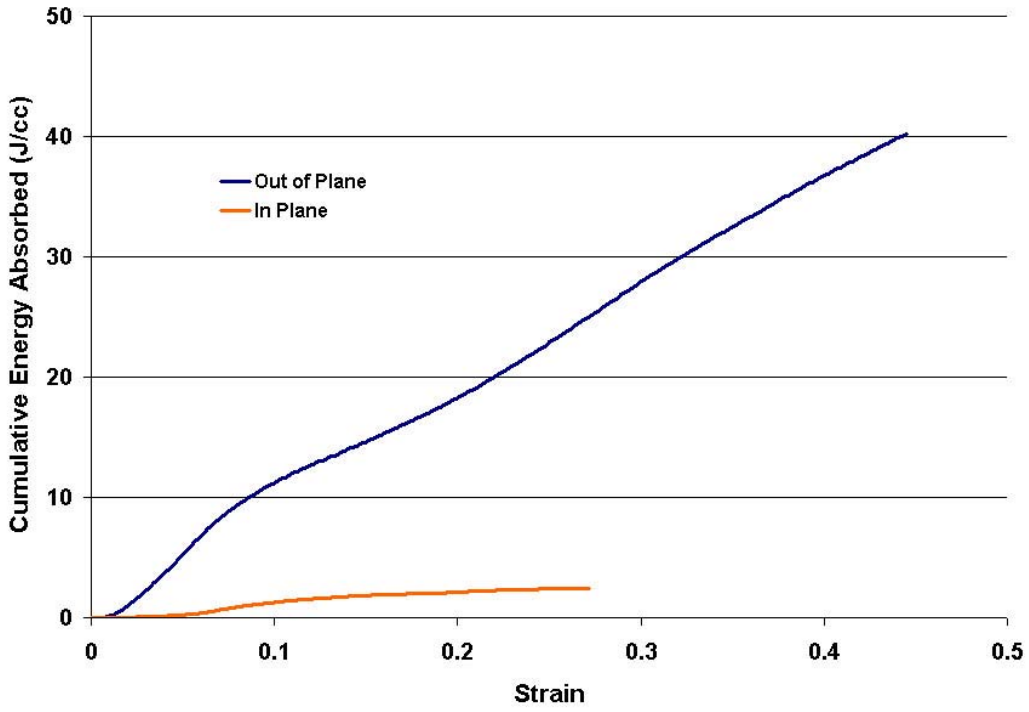

Figure 4.16 – Cumulative energy absorption of hardened Super Invar square annulus LCA under quasi-static compression.

4.2.2 Performance of Triangular LCA

The performance of triangular LCAs under uniaxial quasi-static compression is presented in this section. Super Invar in the annealed and hardened conditions was tested in the out-of-plane and in-plane orientations. Stress-strain response and energy absorption was determined for each condition and orientation. Image capture data was used to determine modes of collapse. Several irregularities were identified in the samples of triangular LCA that were tested. The most severe of these irregularities were the absence of some cell walls and a cell wall node. These defects were attributed to poor extrusion quality and paste rheology. The damaged cells were expected to have a negative effect on the performance of the LCA, specifically during in-plane loading. Wall curvature and lack of straightness along the extrusion direction were also observed

in the samples intended for testing. These defects were minimized during the cutting operation through careful choice of cuts.

Annealed Super Invar Triangular LCA

The out-of-plane stress-strain response of the annealed Super Invar triangular LCA is given in Figure 4.17. The initial rise to peak stress was similar to that observed for the annealed square annulus described previously. An initial linear elastic regime transitioned at the 67.5 MPa yield point to a secondary regime consistent with buckling. A peak stress of 105 MPa was observed before a slight stress decrease to the plateau stress of 90 MPa. This plateau extended to approximately 40% strain before cell wall impingement and the early stages of densification led to a rise in stress. Initially, plastic deformation was characterized by limited buckling of cell walls, Figure 4.18 (B). As collapse progressed, a shear band evolved at an angle of approximately 30° from the normal to the loading axis, Figure 4.18 (C & D). Within the band cells can be seen buckling and cell walls splitting.

In-plane loading consisted of two orientations. The stress-strain behavior of the orientation with cell walls oriented parallel to the loading axis is shown in Figure 4.19. An initial peak of 17.5 MPa was observed before the transition to the plateau stress of 13 MPa. The plateau stress was maintained to a strain of 40% where the behavior transitioned to one of densification. The image capture data, Figure 4.20, showed that the collapse band that formed initially was centered around two adjacent missing cell walls. Intact cell walls in the vicinity of the missing walls were forced to carry an increased load. This led to initiation of collapse around the missing cells and eventual propagation of the collapse band through the sample. The stress-strain behavior of the orientation

with no cell walls oriented parallel to the loading axis is shown in Figure 4.21. This orientation reaches a stress of 24 MPa before transitioning to a plateau stress of 15 MPa. The linear elastic region showed a discontinuity that was attributed to the defects describe previously. As seen in Figure 4.22, a cell wall was missing that contacted the corner of the LCA in contact with the platen. Additionally, some minor wall curvature created non-uniform contact along the loading area of the LCA. These factors combined to cause deformation at the defective corner and ultimately initiate the collapse band along the bottom row of cells. The presence of the missing adjacent cell walls near the center of the LCA cross-section did not appear to affect the collapse of the cells until the initial defect was consumed within the initial collapse band. As the band propagated through the LCA cross-section, those missing cell walls initiated a second partial collapse band adjacent to the previous collapse band.

The cumulative energy absorption of the three orientations is displayed in Figure 4.23. As expected, the out-of-plane energy absorption was significantly better than either in-plane orientation with absorption of 36 J/cc at a strain of 40% as compared to ~5 J/cc. Both in-plane orientations showed similar numbers across the range of strains.

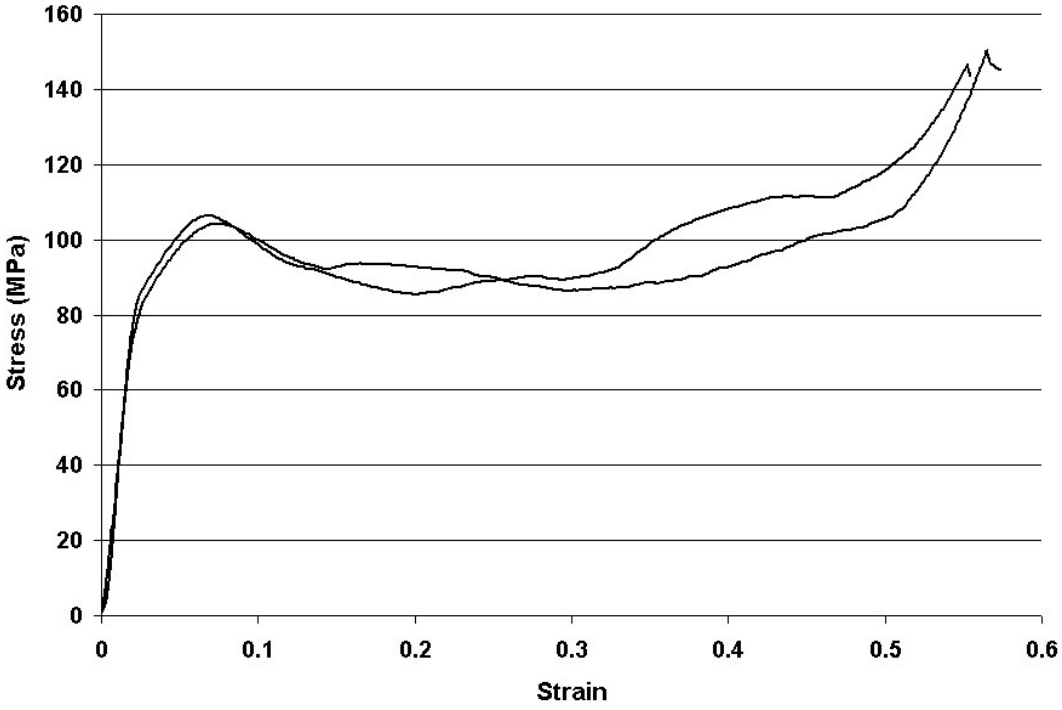

Figure 4.17 – Out-of-plane compression response of annealed Super Invar triangular LCA.

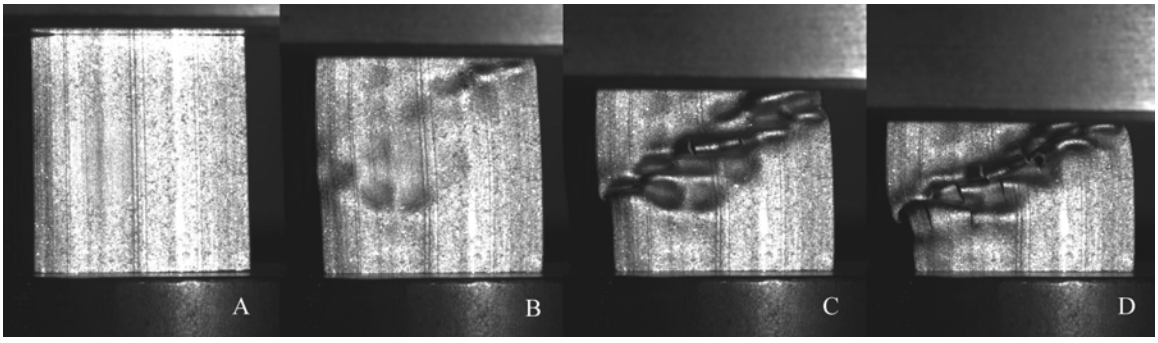

Figure 4.18 – Image capture of out-of-plane loading of annealed Super Invar triangular LCA. A – 0%, B – 9.3%, C – 22.9%, and D – 36.4% strain.

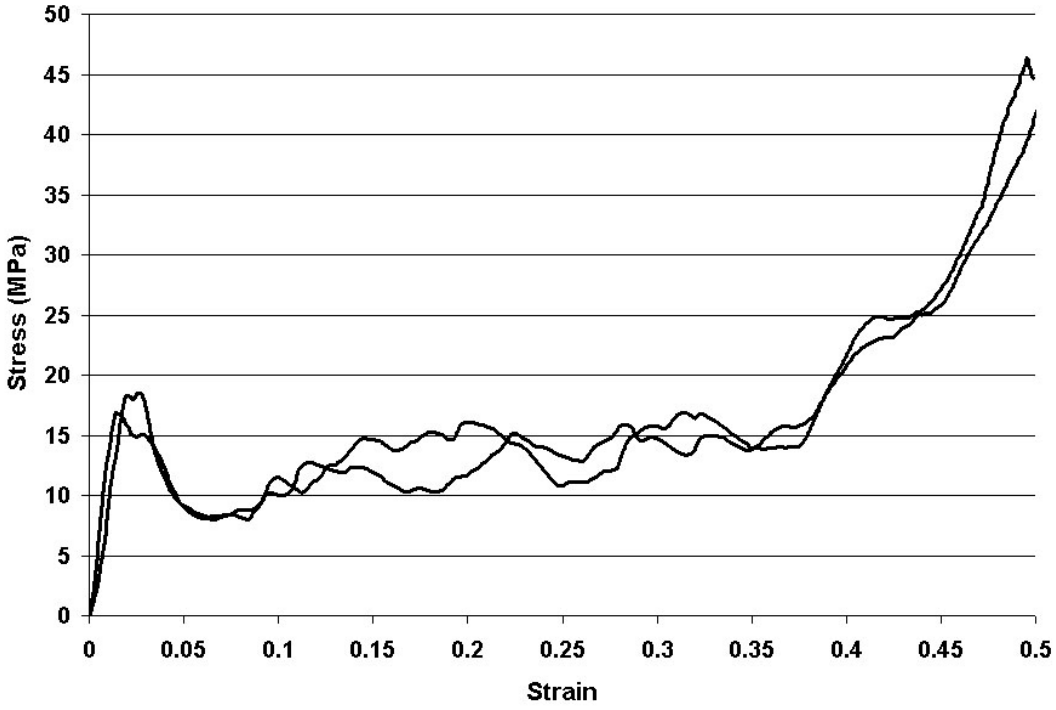

Figure 4.19 – In-plane compression response of annealed Super Invar triangular LCA with cell walls oriented parallel to the loading axis.

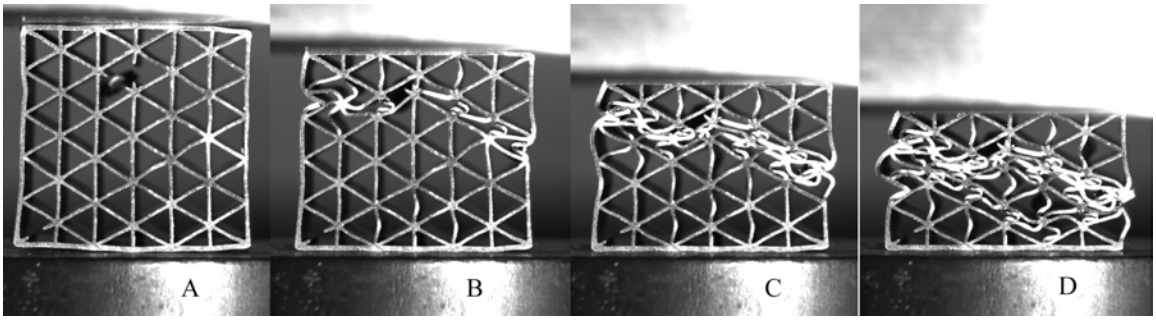

Figure 4.20 – Image capture of in-plane loading of annealed Super Invar triangular LCA with cell walls oriented parallel to the loading axis. A – 0%, B – 9.8%, C – 23.3%, and D – 36.9% strain.

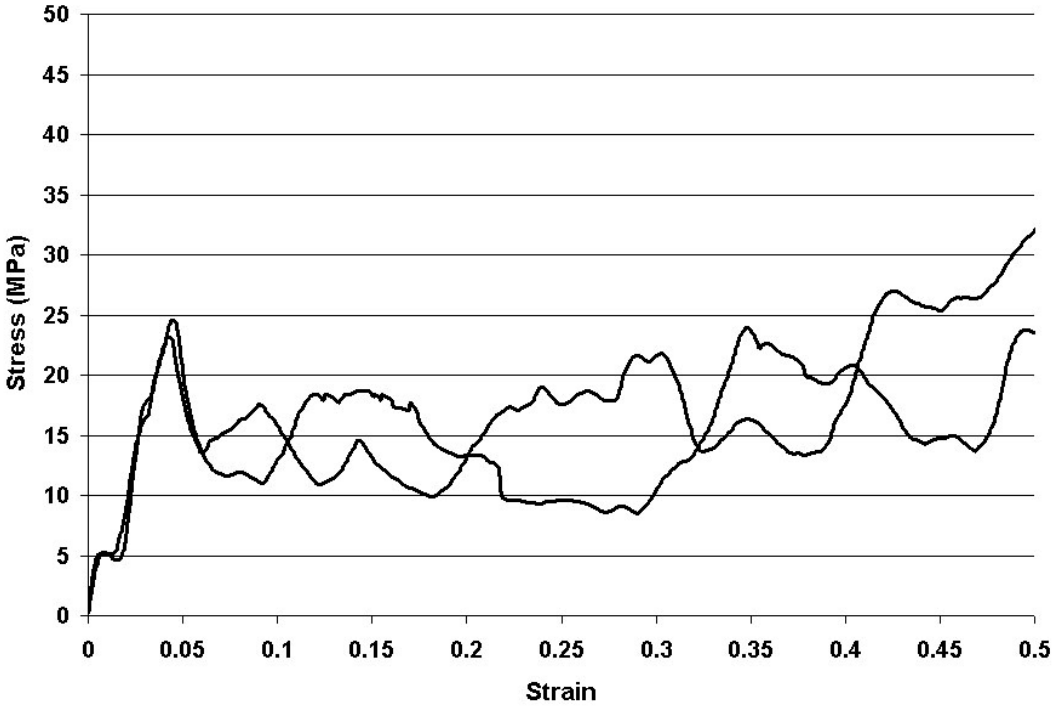

Figure 4.21 – In-plane compression response of annealed Super Invar triangular LCA with cell walls oriented perpendicular to the loading axis.

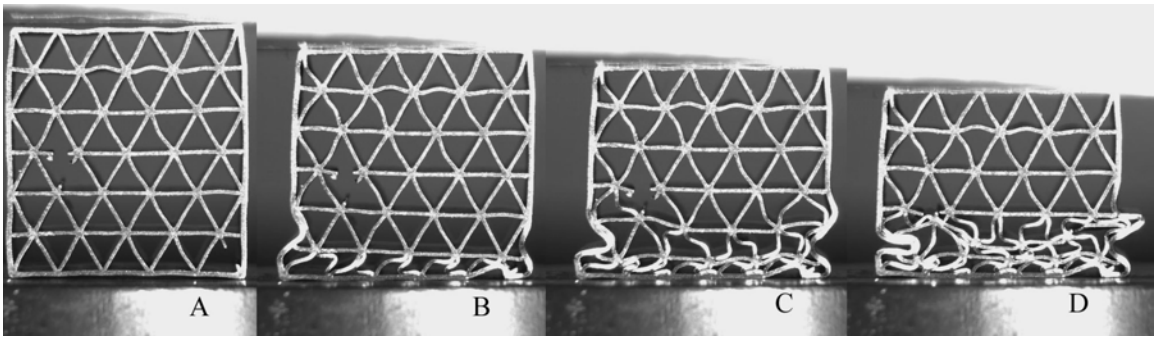

Figure 4.22 – Image capture of in-plane loading of annealed Super Invar triangular LCA with cell walls oriented perpendicular to the loading axis. A – 0%, B – 9.8%, C – 23.3%, and D – 36.9% strain.

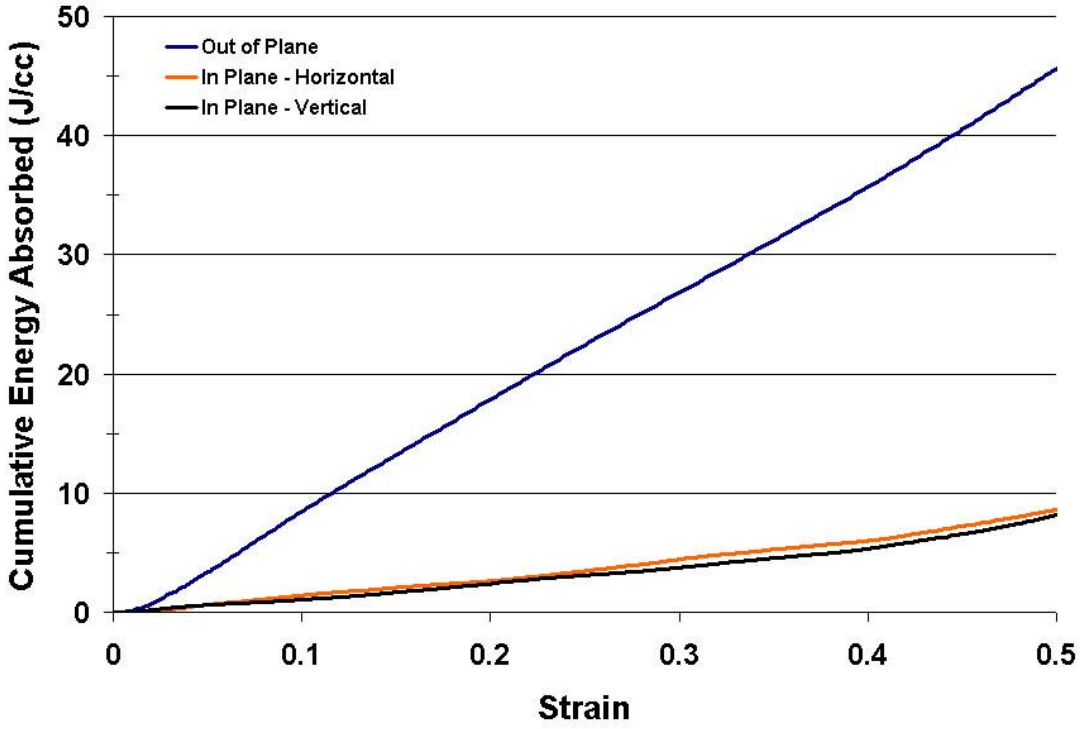

Figure 4.23 – Cumulative energy absorption of annealed Super Invar triangular LCA under quasi-static compression.

Hardened Super Invar Triangular LCA

The out-of-plane compressive behavior of hardened Super Invar triangular LCA is displayed in Figures 4.24 and 4.25. The LCA showed a yield stress of 118 MPa and a peak stress of 178 MPa prior to transitioning to a plateau stress of approximately 120 MPa, Figure 4.24. The plateau was uniform with only 10 MPa difference in the peaks and valleys. Inspection of the visual record, Figure 4.25, showed that the deformation began at the face of the top platen and remained localized to this area. No deformation was seen to occur outside of this area. The localized deformation showed initial buckling, but resulted in splitting and peeling back of exterior cell walls.

In-plane behavior with cell walls oriented vertically is shown in Figures 4.26 and 4.27. The stress-strain behavior, Figure 4.26, showed a series of peaks and valleys with initial peak reaching 24 MPa and no uniform plateau following. The deformation shown in Figure 4.27 was similar to the annealed condition with the presence of defects marking the initiation of a collapse band which propagated through the rest of the sample. The horizontal orientation of cell walls, Figures 4.28 and 4.29, showed better initial strength with a peak of 33 MPa. The plateau stress was not well defined for the lower ductility alloy It was characterized by collapse on a row-by-row basis with stress buildup after the complete collapse of the preceding deformed row. In contrast to the annealed condition, the collapse of this orientation was affected by the presence of the missing cell walls, Figure 4.29. A collapse band can be seen forming along a line containing the missing walls. Ultimately, the collapse band leads to a shearing of the cross-section rather than propagation and the initiation of another collapse band along the bottom of the sample where another defect was located.

Cumulative energy absorption for hardened triangular LCA is shown in Figure 4.30. Again, the out-of-plane orientation gives the highest energy absorption numbers with 50 J/cc at 40% strain. The in-plane values showed more differentiation than the annealed condition, but were small compared to the out-of-plane.

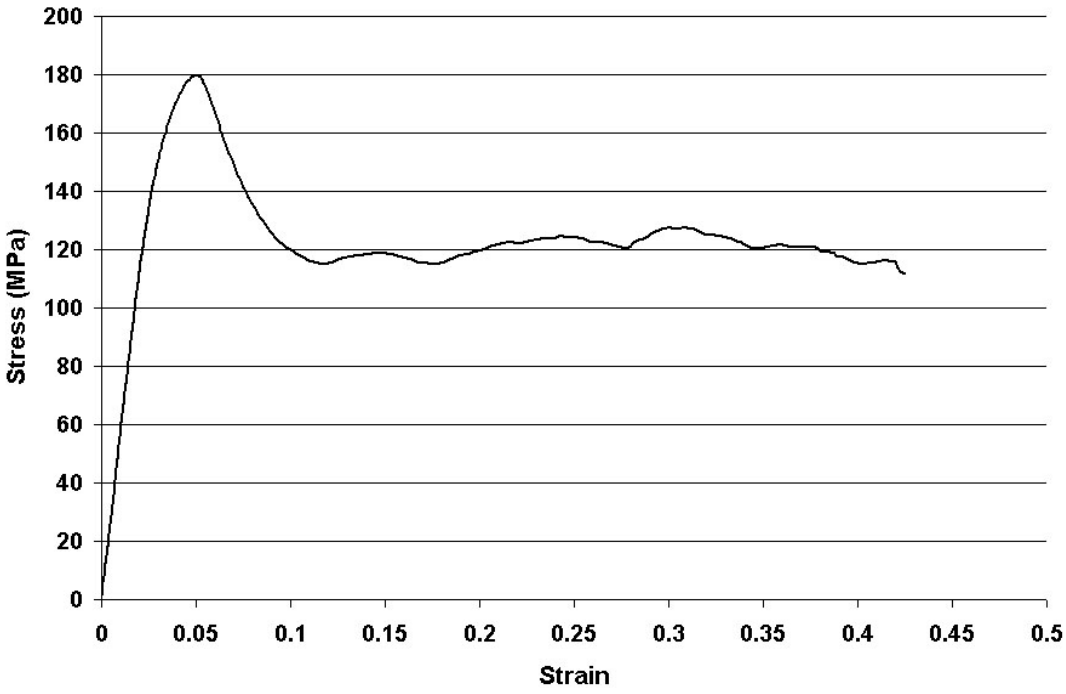

Figure 4.24 – Out-of-plane compression response of hardened Super Invar triangular LCA.

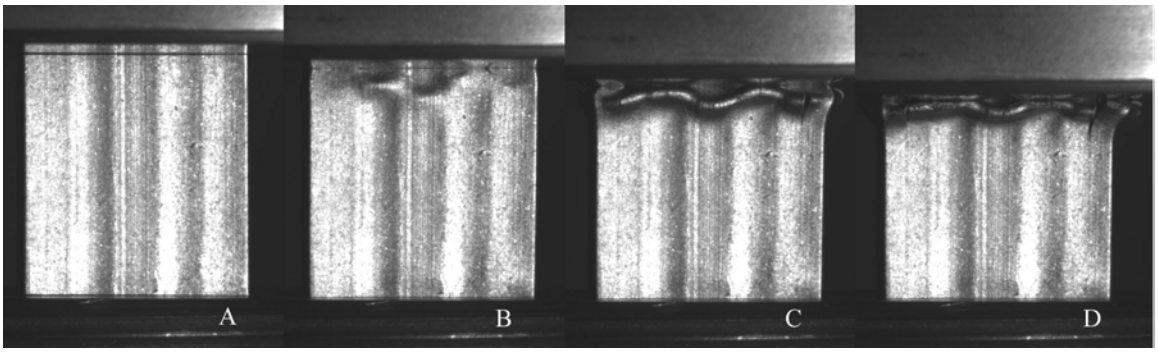

Figure 4.25 – Image capture of out-of-plane loading of hardened Super Invar triangular LCA. A – 0%, B – 4.4%, C – 13.1%, and D – 18.3% strain.

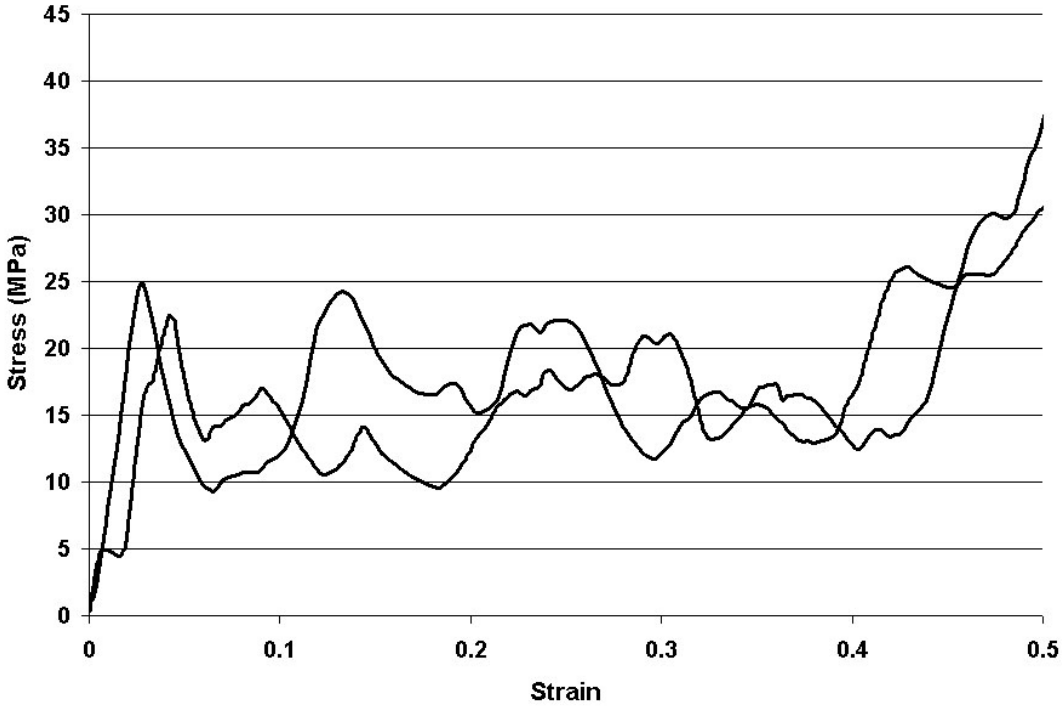

Figure 4.26 – In-plane compression response of hardened Super Invar triangular LCA with cell walls oriented parallel to the loading axis.

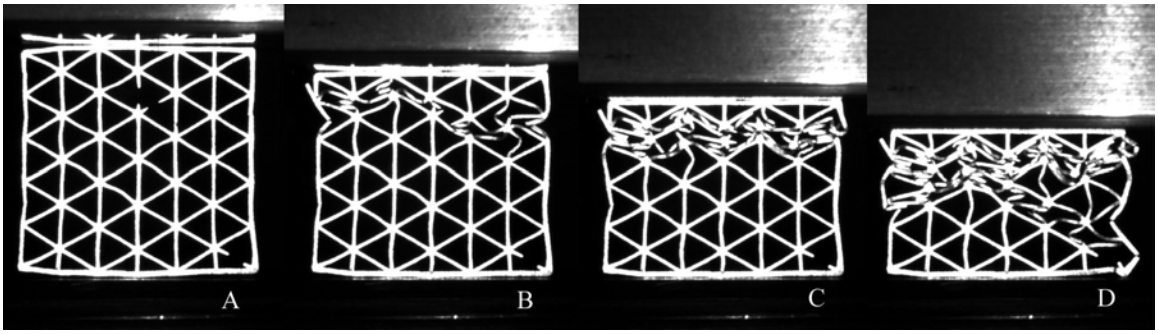

Figure 4.27 – Image capture of in-plane loading of hardened Super Invar triangular LCA with cell walls oriented parallel to the loading axis. A – 0%, B – 11%, C – 23.5%, and D – 36% strain.

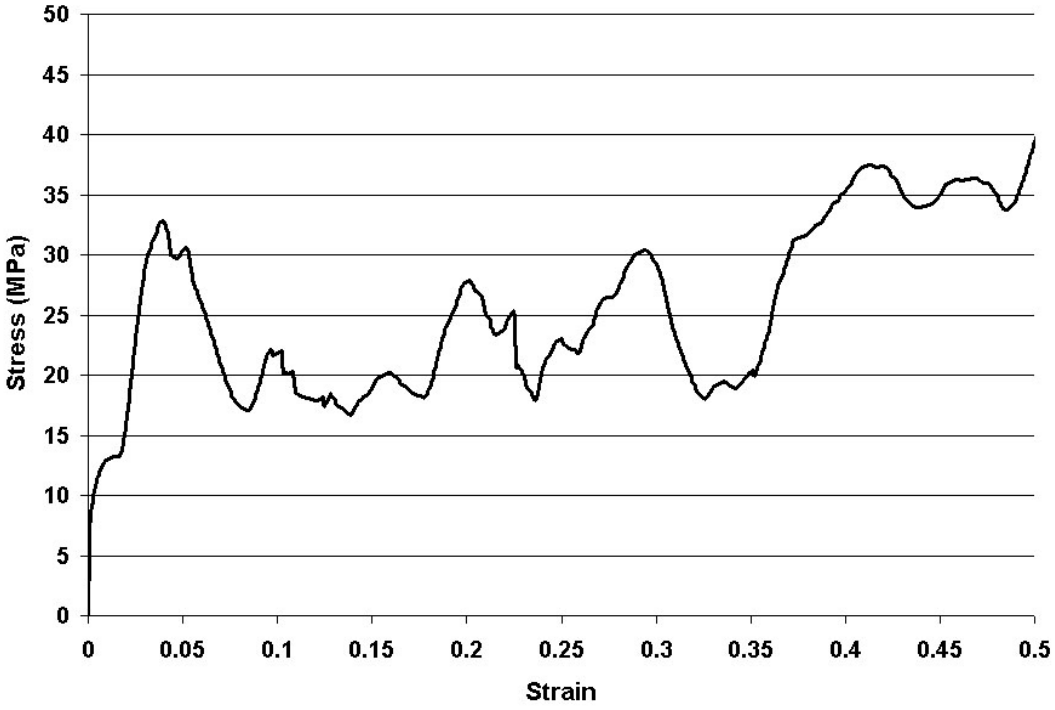

Figure 4.28 – In-plane compression response of hardened Super Invar triangular LCA with cell walls oriented perpendicular to the loading axis.

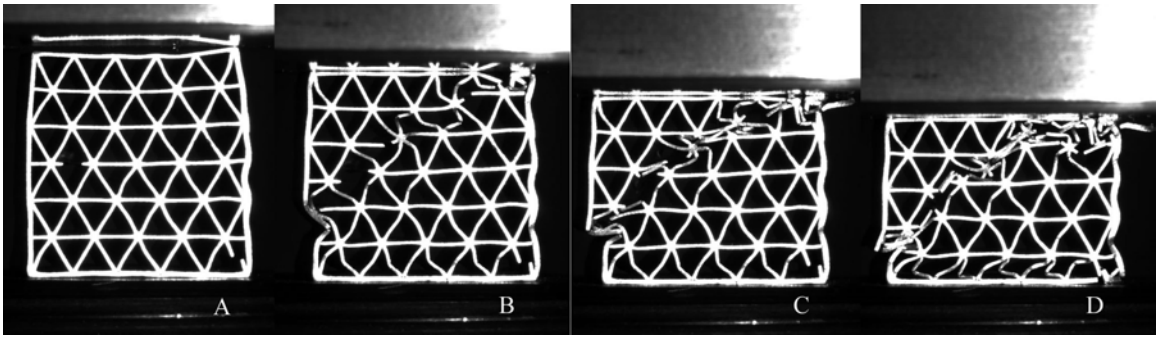

Figure 4.29 – Image capture of in-plane loading of hardened Super Invar triangular LCA with cell walls oriented perpendicular to the loading axis. A – 0%, B – 9.6%, C – 18.4%, and D – 27.9% strain.

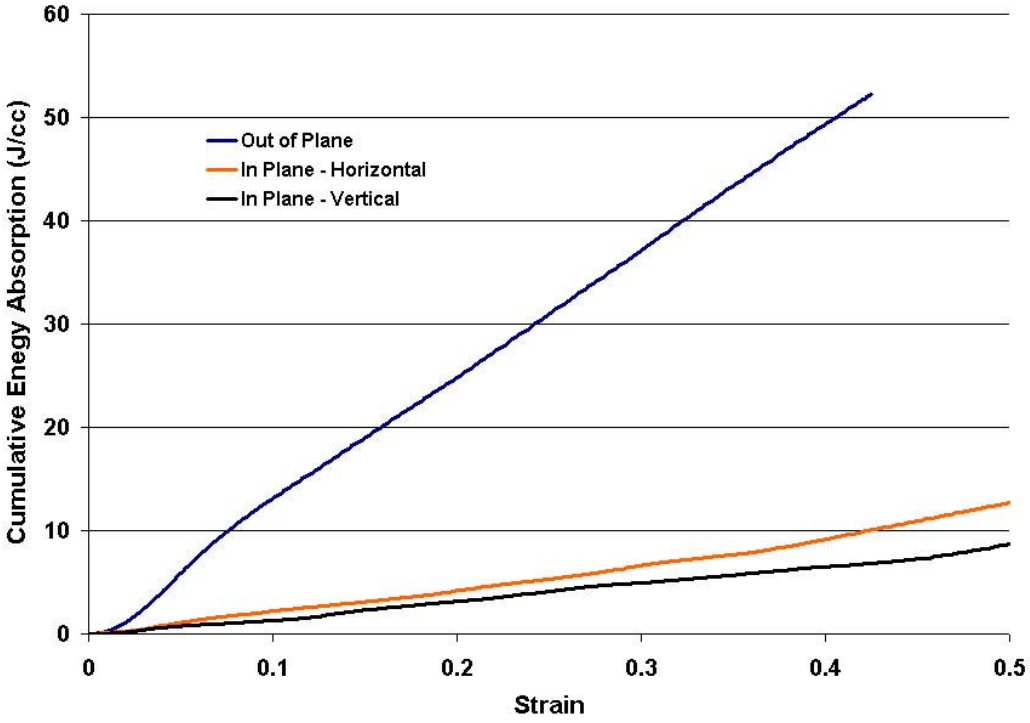

Figure 4.30 – Cumulative energy absorption of hardened Super Invar triangular LCA under quasi-static compression.

4.2.3 Comparison to Cellular Material Models and Experiments

The mechanical properties of the square annulus and triangular honeycomb designs tested in this study can be found in Table 4.1. Values for the yield stress, σ_{pl}, peak stress, σ_{max}, the plateau stress, $\sigma_{plateau}$, and the cumulative energy absorption, E_A, at 40% strain are reported. No models were available with which to compare the performance of the square annulus honeycomb due to its unique design. Of interest, however, is that both the annealed and hardened conditions reach peak stress values well above the upper bound for out-of-plane yield strength of honeycomb. The upper bound predicted value was calculated using the relative density of the honeycomb, 21.4%, and the material strengths taken from Table 3.2. For the annealed and hardened conditions, this would translate to a predicted honeycomb yield strength of 55.9 MPa and 88.6 MPa,

respectively. Experimentally, values of 62.9 MPa and 83.6 MPa were recorded for out-of-plane loading. This represents a 12.5% positive difference for the annealed condition and a 16% negative difference for the hardened condition. In-plane behavior for the square annulus showed a much lower strength as expected from this orientation. However, the annulus performed at a similar level as the triangular honeycomb for both in-plane orientations with respect to the plastic buckling strength. The annulus design showed poor performance in the plateau strengths for in and out-of-plane loading due to shearing and splitting of the annulus walls.

The triangular honeycomb does have in-plane models available for comparison. The models used for comparison were presented by Hayes et al. and Wang and McDowell and were detailed in a Section 4.1.2. The predicted values for plastic buckling strength in the out-of-plane and two in-plane orientations can be found in Table 4.1 along with the experimental values for the triangular LCA. The relative density of this design was determined to be approximately 23.7%. Some error in determination of relative density exists due a number of non-uniformities present in the powder-processed LCAs. These include curvature and rippling in the outer skin of the LCA. Additionally, the experimental specimens had a number of internal defects including wall curvature and corrugation, missing cell walls, and cell wall splitting. These must be recognized as strength modifiers in the comparison to the idealized models. Like the square annulus, the out-of-plane orientation for the triangular LCA performed well above the simple upper bound model for out-of-plane peak strength due to post-yield buckling behavior. The annealed and hardened alloys showed yield strengths that were 9% and 20% higher than the predicted strengths, respectively. Conversely, the in-plane behavior for the

triangular LCA was lower for both in-plane orientations and alloy conditions ranging from a 15 to 33% difference. The most probable cause for the poor performance can be traced to the presence of defects described previously. Analysis of the image capture data showed that the missing cell walls nucleated a collapse band in the vicinity of the defect from which the deformation propagated through the bulk of the specimen. For the in-plane orientation in which the cell walls were oriented parallel to the loading axis (Orientation 1), Figures 4.20 and 4.27, the absence of adjacent cell walls including a vertical ligament result in the local collapse. Consequently, these orientations showed the greatest negative deviation from the predicted value for the respective alloy conditions with differences of 22.7% for the annealed and 33.2% for the hardened. In-plane loading in Orientation 2, Figures 4.21 and 4.28, showed similar local deformation at missing cell walls. Collapse initiated at a missing cell wall intersecting the corner of the LCA in both specimens rather than at adjacent missing cell walls in the center of the LCA.

Due to machine compliance and error in the results for elastic modulus from stress-strain analysis, the moduli presented in Table 4.1 are purely based on the models. The model used to calculate the predicted modulus was $\frac{E_3^*}{E_S} = \left(\frac{\rho^*}{\rho_S}\right)$, where E* is the modulus and ρ* is the density of the honeycomb, and E_S is the modulus and ρ_S is the density of the bulk material. Modulus data, presented in Table A.1 of the Appendix, was used for the bulk material.

Table 4.1 – Quasi-static compression properties of honeycombs tested under in-plane and out-of-plane loading.

	Super Invar Triangular Honeycomb							
	Experimental Values					Predicted Values		
	σ_{pl} (MPa)	σ_{max} (MPa)	$\sigma_{Plateau}$ (MPa)	E_A @ 0.4ε (J/cc)	E (GPa)	σ_{pl} (MPa)	σ_{pl1} (MPa)	σ_{pl2} (MPa)
Annealed								
OP	67.5	105	90	36	28.9	61.9	--	--
IP_1	23.9	--	15	6	9.6	--	30.9	--
IP_2	17.5	--	13	5	9.6	--	--	20.6
Hardened								
OP	117.8	179.4	120	49	30.1	98.1	--	--
IP_1	32.8	--	22	9	10.0	--	49.1	--
IP_2	23.1	--	16	6.5	10.0	--	--	32.7

	Super Invar Square Annulus					
	σ_{pl} (MPa)	σ_{max} (MPa)	$\sigma_{Plateau}$ (MPa)	E_A @ 0.4ε (J/cc)	σ_{pl} (MPa)	
Annealed						
OP	62.9	99.5	--	18	55.9	
IP	22.9	--	6	3	--	
Hardened						
OP	83.6	157.4	80	37	88.6	
IP	27.5	--	6	2.5 @ 0.27e	--	

OP - out-of-plane
IP_1 - in-plane, walls perpendicular
IP_2 - in-plane, walls parallel
IP - in plane
σ_{pl} - out-of-plane yield stress
σ_{max} - max buckling stress
$\sigma_{Plateau}$ - plateau stress
Subscripts 1 and 2 denote in-plane cell wall orientations specific to triangular honeycomb anisotropy

The out-of-plane predictions for plastic yielding of the honeycomb structures have been shown to agree well with predicted values. For instances where the model predicted higher than achieved yield strengths it was assumed that defects were responsible for the deficiencies. Defects were not uncommon due to the manufacturing process. Missing cell walls, and cell wall curvature or corrugation were the most common defects. For instances where models predicted lower than achieved values the discrepancy was attributed to two possibilities. First, the yield strength used in modeling was from uniaxial testing rather than compression. It should be expected that the compressive strength of the same bulk material would likely be higher than the tensile response. This

is because the porosity present in the material would be annihilated during compression and the material would behave as fully dense. Thus, a higher compressive strength for the bulk material would translate to higher predicted honeycomb values. Second, the non-uniformity in exterior dimensions of the honeycomb created uncertainty in the measurement of relative density. By underestimating the relative density, the model would predict lower values.

Recent models have been introduced to predict the mean crushing strength in out-of-plane compression. Since the mean crushing strength is tied to the plateau stress, these models have important implications for designing honeycombs for the purpose of energy absorption. Wierzbicki et al [31,43,44] predicted a mean crushing strength proportional to $r^{5/3}$, where r is relative density. More recently, Wang, Totty, and McDowell[44] introduce a relationship,

$$\sigma_m / \sigma_0 = c_1 r + c_2 r^2,$$

where σ_m is the mean crush strength, σ_0 is the bulk yield strength, r is relative density, and c_1 and c_2 are constants equal to 0.684 and 2.64, respectively, for triangular cells. Using this model, a mean crushing strength for the triangular honeycomb in the annealed and hardened was predicted to be 81 MPa and 129 MPa. Comparing this to the plateau stress from the experimental data in Table 4.1 showed that the honeycomb performs very close to expectations. Plateau stress for the annealed honeycomb exceeded expectations with a stress of 90 MPa while the hardened condition showed a slightly lower than predicted stress of 120 MPa.

Energy absorption for LCAs was shown to be significantly higher in the out-of-plane direction as opposed to the in-plane direction. Hayes[45] reports energy absorption at

25% strain as high as 63.2 J/cc and 140 J/cc just prior to densification for out-of-plane loading. Tests on Super Invar showed a maximum of 49 J/cc prior to densification. This result follows the hierarchy of material strengths of maraging and Super Invar. The maraging compositions show bulk strengths double that of the hardened Super Invar and therefore higher honeycomb strength. This translates to more energy absorption for the maraging composition. In-plane energy absorption was also superior in the maraging composition with the best Super Invar values matching the lowest of the maraging.

When compared to other cellular materials the out-of-plane properties of LCAs, in general, far exceed the properties of foams. For example, Ashby et al.[46] report that the best available metal foam has the ability to absorb approximately 11 J/cc at 25% strain and a plateau stress of 40 MPa. This is well below the capabilities of both the maraging steel and Super Invar LCAs tested and described in this section. In-plane properties, however, are highly dependent on the material and geometry of the LCA. The highest strength materials such as maraging steel can surpass the best foams while the lower strength Super Invar LCAs fall within the current capabilities of foams.

4.3 Conclusions

Metal honeycombs fabricated using the powder processing technique have been shown to perform near or above levels predicted by available models. Out-of-plane behavior was consistent with existing models for yield strength and mean crushing strength. In-plane performance was adversely affected by the presence of defects such as missing cell walls, cell wall corrugation, and rippling of the LCA skin. Consequently, in-plane performance did not meet the predictions of the models. If it is assumed that the predictions are reasonably accurate, then loading in Orientation 1, which had cell walls

parallel to the loading direction, showed more sensitivity to the presence of defects than Orientation 2. However, the overall performance of the triangular LCA showed good energy absorption due to high plastic buckling strengths and plateau strengths. In-plane performance showed good energy absorption as well, but in general did not exceed the performance of some metal foam. The square annulus design showed good results in terms of plastic buckling strength. However, plateau strength suffered for this design due to splitting and shearing of the annulus walls. As a consequence, energy absorption was lower. However, energy absorptions values ranging from 49 to 140 J/cc have been achieved from LCAs. Due to the small number of samples tested for each condition and geometry, the behavior of LCA honeycombs that has been presented must be tempered with a lack of statistical strength. However, the reproducibility among samples and close approximation to the models validates these conclusions. Overall, honeycombs fabricated using chemo-powder processing have been shown to have excellent mechanical properties, in many cases, exceeding those of metal foam and other honeycomb.

Chapter 5

LCA Dynamic Behavior

5.1 Introduction

It has been demonstrated throughout this research that Linear Cellular Alloys can be fabricated with numerous cross-sections using a number of alloy systems. The ability to control cell wall thickness, cell shape, and cell size in conjunction with alloy selection has been shown to offer tailorable mechanical properties under quasi-static compressive loading conditions. Further exploration of the potential applications of LCAs has led to the investigation of the dynamic response of these materials. Characterization of these materials under high strain rate loading allows comparison to be made with the performance of monolithic materials and for determination of the suitability of LCAs for various impact loading applications. Specifically, there is great interest in the use of LCAs as an encapsulant for energetic materials. The key to the successful implementation of Linear Cellular Alloys as energetic capsules lies not only in their ability to deliver the materials to their intended destination, but also to transmit the stress and aid in the initiation and sustainability of the high-energy reaction. It is to this end that the research presented in this chapter has been conducted.

5.2 Background

Considerations for the use of LCAs as energetic capsules must take into account the dynamic response of the honeycomb materials including deformation and fragmentation upon impact. This data, in turn, must be related to the mechanisms of initiation and propagation of common energetic materials.

5.2.1 Properties of Materials under Static and Dynamic Loading

The LCA mechanical properties presented in this research thus far have been restricted to low strain-rates on the order of 10^{-2} to 10^{-3} s^{-1}. This falls into the regime of quasi-static loading encompassing a strain-rate range of ~10^{-4} to 10^{0} s^{-1}. In this range the specimen experiences a load rate that allows equal distribution of stress throughout the volume of material during loading. As the loading rate, or strain-rate, is increased the time scale for load distribution is reduced and a nonuniform stress distribution results. The dynamic range of strain-rates covers 10^{1} s^{-1} and higher. For the purposes of LCA testing a strain rate range of 10^{3} to 10^{4} s^{-1} was targeted. In this regime elastic and plastic waves are generated in the material during loading, the latter of which is responsible for plastic deformation in the material. As loading rates are increased still further, the generation of shockwaves is observed.

Elastic Waves

The propagation of an elastic wave through a medium occurs through a succession of atomic displacements at the wave front.[21] The nature of the atoms and their interatomic forces determine the velocity of the wave in the medium. Several types of elastic waves can be generated in a medium subjected to a high loading rate. These can include longitudinal, shear, surface (Rayleigh), and flexural waves among others. For relevance of testing LCAs at high strain rates, longitudinal and shear waves are described here.

Longitudinal waves, also known as dilatational waves, occur with a particle displacement that is parallel to the direction of travel of the wave front. Particle velocity

and wave velocity are parallel and may be of the same or opposite sense. For compressive longitudinal waves the sense is the same and for tensile waves the sense is opposite. By treating the medium as an unbounded continuum, an expression for the velocity of a longitudinal wave can be derived,

$$V_{long} = \left(\lambda + 2\mu \Big/ \rho\right)^{\frac{1}{2}},$$

where $\lambda = \upsilon E \Big/ \left[\left(1+\upsilon\right)\left(1-2\upsilon\right)\right]$, $\mu = E \Big/ \left[2\left(1+\upsilon\right)\right]$, ρ is density, υ is Poisson's ratio, and E is the elastic modulus. Assuming the material is under uniaxial stress, the relationship becomes,

$$V_{long} = \left(E \Big/ \rho\right)^{\frac{1}{2}}.$$

This is identical to the velocity of a wave propagating in a cylindrical bar.

Shear waves, or distortional waves, create particle displacements perpendicular to the direction of travel of the wave front. Particle velocities are therefore perpendicular to that of the wave velocity. Density changes are not observed during shear wave propagation and longitudinal strains remain zero. The velocity of shear waves in an unbounded medium is given as,

$$V_{shear} = \left(\mu \Big/ \rho\right)^{\frac{1}{2}}.$$

Plastic Waves

Plastic waves are the result of a pulse that exceeds the yield stress of the material. In this case both elastic and plastic waves are generated in the medium. The velocity of the plastic wave is dependent on the material,s behavior in the plastic regime. Von

Karman and Duwez[48] calculate a velocity, $V_p = \left(\frac{\delta\sigma/\delta\varepsilon}{\rho} \right)^{\frac{1}{2}}$, where $\delta\sigma/\delta\varepsilon$ represents the instantaneous slope of the stress-strain curve in the plastic regime. The relationship is the same as that presented for the speed of an elastic wave. However, $\left(\delta\sigma/\delta\varepsilon\right)_p$ will be less than $\left(\delta\sigma/\delta\varepsilon\right)$ in the elastic regime for a bounded medium. This means that the plastic wave speed will necessarily be less than the elastic wave speed. Furthermore, the dependence of the plastic wave speed on the instantaneous plastic slope implies that the wave speed will not be constant over the duration of the pulse. As the pulse duration extends into the plastic regime, the material is expected to work-harden and the slope of the plastic portion of the stress-strain curve decreases to the point of necking and failure. This leads to a continual decrease in plastic wave speed as strain increases. The resulting wave velocity profile will show an elastic portion followed by a plastic portion that decreases to a minimum as the critical strain is approached.

Assuming a plastic behavior given by $\sigma = k\varepsilon^n$, where k is the work-hardening coefficient and n is the work-hardening exponent, the plastic wave speed can be calculated as a function strain. In this case, $V_p = \left(\frac{\delta\sigma/\delta\varepsilon}{\rho} \right)^{\frac{1}{2}}$ and $\delta\sigma/\delta\varepsilon = \left(kn\varepsilon^{n-1}\right)^{\frac{1}{2}}$, therefore $V_p = \left(kn\varepsilon^{n-1}\right)^{\frac{1}{2}} \Big/ \rho$.

If one considers an unbounded medium where lateral flow of material can be neglected then a uniaxial strain state is the result. Under these conditions the slope in the plastic regime increases with strain, or pulse duration, and the plastic wave velocity will

necessarily increase. This has the reverse effect on the wave velocity profile. Instead of the dispersion of the plastic wave with time/strain, there is what researchers have referred to as a "steepening" up of the plastic wave front. This discontinuity in the plastic wave velocity profile is known as a shock front.

Shock Waves

Shock waves[21] have been defined as discontinuities in material properties ahead of and behind a shock front. A shock front may result from the propagation of a plastic wave in a medium under uniaxial strain or by application of load in a strain rate range of 10^5 to 10^8 s^{-1}. As the shock front propagates through a material under the initial conditions of pressure (P_0), particle velocity (U_0), and density (ρ_0) it establishes new conditions immediately behind the shock front. Since the shock front is very steep, the change in material properties is said to be discontinuous. The new conditions P, U_p, and ρ can be related to the initial conditions and the velocity of the shock front through a series of conservation equations. Rankine and Hugoniot developed these equations based on a hydrodynamic treatment of a piston compressing a fluid. The analysis assumed that the shock front was a discontinuous event and that the material experienced such a high hydrostatic stress that the material effectively had no resistance to shear. It also assumed that there was no elasto-plastic behavior and the material did not undergo any phase transformations during the event. Under these conditions the following relationships have been developed to describe the parameters of shock waves,

$$\rho_0 U_S = \rho\left(U_S - U_P\right),$$

$$\left(P - P_0\right) = \rho_0 U_S U_P, \text{ and}$$

$$PU_P = \frac{1}{2}\rho_0 U_S U_P^2 + \rho_0 U_S \left(E - E_0\right),$$

where ρ is material density, U_S is shock wave velocity, U_P is particle velocity, P is pressure, and E is internal energy. The subscript '*0*' refers to initial conditions as opposed to post-shock conditions. Respectively, these equations refer to the conservation of mass, momentum, and energy. An additional relationship known as the equation of state (EOS) was postulated to allow each parameter to be solved for in terms of one of measured parameters. The EOS relates particle velocity to shock wave velocity in the following form,

$$U_S = C_0 + S_1 U_P,$$

where C_0 is the velocity of sound in the material at zero pressure and S_1 is an experimentally determined constant.

5.2.2 Measuring Dynamic Yield Strength of Materials

The classic experimental method for determining the dynamic yield strength of materials has been presented by Taylor[49] and validated by Whiffin[50]. It consists of impacting a right-circular cylinder against a rigid anvil at an impact velocity in the plastic wave regime. On impact an elastic wave is created in the material followed by a plastic wave, assuming the flow stress of the material is exceeded. The elastic wave, being faster than the plastic wave, travels through the projectile, reflects off the back surface, and eventually superimposes on the plastic wave front. The superimposition combined with the work-hardening characteristics of the projectile ultimately lead to the dissipation of the plastic wave. Taylor's post-impact analysis of the projectile relates the final

geometry of the projectile to the dynamic yield stress. The following relationship was derived to calculate the dynamic yield stress,

$$\frac{\rho U^2}{S} = \frac{e_1^2}{1-e_1},$$

where ρ is density, U is impact velocity, S is dynamic yield stress, and e is the compressive strain defined as $e = 1 - \frac{A_0}{A}$, where A_0 is the starting cross-sectional area and A is the final cross-sectional area at the impact face. The relationship is said to be valid for $\frac{L_1 - X}{L} \leq 0.4$, where L_1 is the final length of the rod, X is the length of the plastic zone, and L is the initial rod length. Above this value the length of the plastic zone approaches the final length of the projectile and the uncertainty in the measurement of the plastic zone becomes significant. Wilkins and Guinan[51] revisited the problem of impact on a rigid body with the aid of computer modeling. They developed a similar relationship relating initial and final projectile lengths to dynamic strength as follows,

$$\ln \frac{L^f}{L^0} = -\frac{\rho^0 U^2}{2Y^0},$$

where L^f is the final length, L^0 is the initial length, ρ^0 is density, U is impact velocity, Y^0 is dynamic strength.

Efforts to model the behavior of materials as a function strain rate have mostly centered around use of a constitutive equation proposed by Johnson and Cook[52]. This relationship takes into account three factors associated with plastic behavior: work-hardening, strain-rate sensitivity, and temperature effects on flow stress. Johnson and Cook proposed the following relationship to describe plastic behavior,

$$\sigma = \left(\sigma_0 + B\varepsilon^n\right)\left(1 + C\ln\frac{\dot{\varepsilon}}{\dot{\varepsilon}_0}\right)\left[1 - \left(T^*\right)^m\right],$$

where σ_0 is yield stress, B is work-hardening coefficient, n is the work-hardening exponent, T^* is the homologous temperature, and C and m are constants. Several modified or revised forms of this equation have been proposed. Most focusing on the strain rate factor as it relates to different materials.[53]

5.2.3 Fragmentation

The Taylor anvil impact test described in the previous section requires that test samples remain intact after impact for post impact geometrical analysis. Conservation of mass is a requirement of the Taylor analysis approach as it is among others. However, as one increases impact velocity or decreases ductility of the specimen, dynamic fracture may result. Unlike quasi-static fracture where the sample simply fractures into a few pieces, dynamic fracture can generate a significant number of fragments. This is due to the nature of crack nucleation and propagation at high strain rates. For brittle materials under quasi-static loading failure occurs through initiation and propagation of a flaw or crack. As load is increased the crack tip experiences an increased stress as a result of stress distribution about the crack tip. The crack propagates through the sample cleaving it in two. Materials under dynamic loading can experience loading rates that exceed the crack propagation velocity. Crack propagation is dependent on energy provided to the crack tip. However, the speed with which energy can reach the crack tip is limited. It has generally been accepted that the Rayleigh wave velocity is the limiting velocity for propagating cracks. When the limiting velocity is reached crack branching occurs to meet the energy release demands. Several researchers have investigated fragmentation

events at high strain rates in an attempt to relate fragment characteristics (e.g., size and weight distributions) to materials properties.

Mott[54] analyzed fragmentation using the example of an expanding ring such as can be found in the detonation of a hollow cylinder shell casing. His analysis considered thin rings stacked to form a hollow cylinder. This allowed the estimation of fragment sizes in terms of length rather than length and width. Ultimately Mott argued that the average fragment length would be proportional to fracture strength and strain, and inversely proportional to work-hardenability and density of the material. This means that high strength or high ductility materials would create large fragments while highly work-hardenable and high density materials would generate small fragments. Thus it would be expected that a high strength, low ductility alloy such as maraging steel would produce smaller fragments than a high ductility, low work-hardenable alloy such as Super Invar. Grady and Kipp[55,56] relate strain rate to fragment size through a mechanistic approach. They found that the fragment size was proportional to the $\dot{\varepsilon}^{-m/(m+3)}$ where m is the Weibull flaw distribution. Minimizing the energy of the system with respect to the fracture surface area density, a relationship was derived for the fragment diameter, $d = 6\left(\frac{5\rho\gamma}{3\pi\dot{\rho}^2}\right)^{1/3}$. Similarly, Yew and Taylor[55] used thermodynamic arguments to minimize the Gibbs energy in a volume by the number of fragments in that volume. The resulting relationship differed with Kipp and Grady's equation by a factor of $1/(2)^{2/3}$. Kipp et al[58] and Grady and Kipp[59,60] more recently analyzed the fragmentation properties of metals through both experimental work and numerical analysis. In their work they

derive a relationship for the dynamic fracture toughness based on the projected area of fragments and the statistical fragment size. The relationship showed that the dynamic toughness was directly proportional to the strain rate and fragment size.

Energetic Reactions

Energetic reactions such as those considered for use with LCA capsules typically require high pressures to initiate and sustain the reactions. For example, Ni + Ti reactive powder materials require a minimum of 3 GPa to initiate a highly exothermic reaction with a heat of reaction of 624 J/g that results in the formation of a NiTi intermetallic.[61] Increased pressures above the initiation pressure also serves to generate more highly energetic reactions. The significance of testing at high strain rates lies in the need to understand the dynamic behavior of not only the direct-reduced alloy system, such as Super Invar or Maraging steel, used to fabricate the LCA, but also the need to understand the effect of both the cellular nature of the LCA material and potential fillers, i.e., energetic materials.

5.3 Experimental

The investigation into the suitability of LCA materials as energetic capsules consisted of quasi-static and dynamic testing of two capsule designs. The designs were intended to simulate a potential projectile ordinance system. Samples were fabricated with multiple alloys and thermal treatments. These samples were tested unfilled and filled with an inert polymer chosen as a simulant to energetic material behavior. Quasi-static tests of both designs were completed under all conditions of alloy system, thermal treatment, and fill. Dynamic testing was limited to a single capsule design and two

alloys. A reverse setup of the classic Taylor anvil impact test was used to achieve dynamic loading conditions.

5.3.1 Materials Selection

The selection of materials for use in LCA energetic applications required the choice of two components for the test specimens. The components were the structural element of the energetic capsule, or the LCA, and the energetic material carried by the capsule, or the simulant filler.

The metallic materials used for LCA energetic capsule experimentation were chosen from the Super Invar and Maraging steel compositions discussed previously in this research. The body of data generated from this research for the behavior of these alloys processed using the LCA fabrication technology along with the range of properties possible with thermal treatments and minor composition changes made them the most suitable candidates. For validation of the experimental setup with respect to the classic Taylor anvil impact test, a copper rod was chosen as the first sample to be tested. This allowed comparison of the post impact sample geometry to results in the literature and provided insight into needed modifications to the setup without sacrificing the more valuable LCA materials. Super Invar in the fully annealed condition was used for subsequent LCA tests due to its good strength and high ductility. Maraging 200 steel was chosen for a final test to observe the effects of high strength and low ductility on impact behavior.

The energetic capsules were tested in the filled and unfilled conditions. The filler was chosen based on possible energetic material compositions including Fe_2O_3 and Al powder in a epoxy matrix or Al powder in a Teflon binder matrix. For purposes of LCA

testing, reactive ingredients were not used as filler in order to reduce safety concerns. LCAs were instead filled with polymer filler that would simulate the mechanical properties of an energetic filler. Polymers for consideration included epoxy, Teflon, and polyethylene. The compressibilities of these polymers are plotted in Figure 5.1 from Hugoniot data found in the literature. All three candidates show similar behavior making the choice of polymer one of convenience. It was determined that epoxy was a suitable alternative to a reactive filler. The epoxy was a two-part epoxy using Miller-Stephenson Epon 826 resin and diethanolamine hardener mixed at a 12:1 weight ratio.

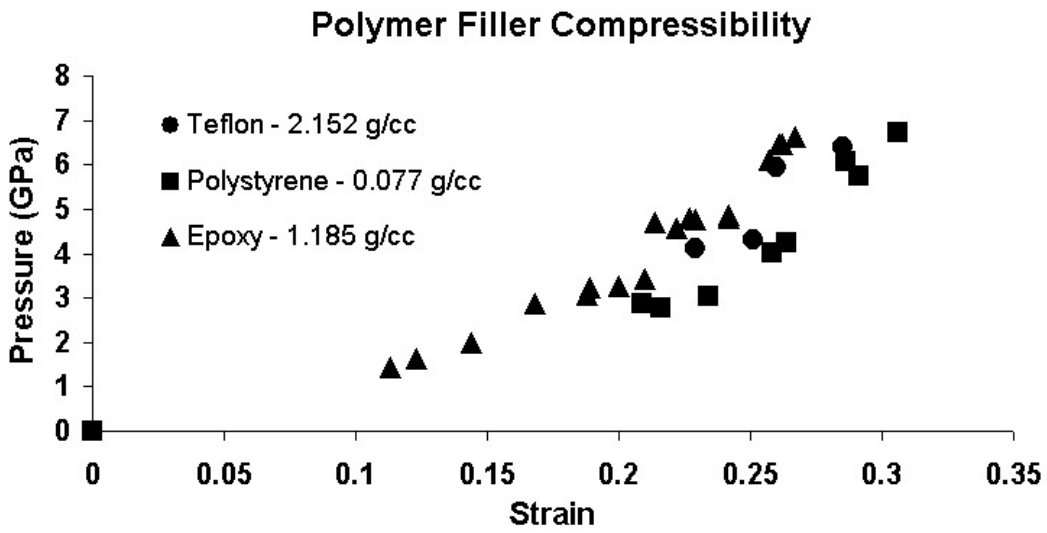

Figure 5.1 – Compressibility of candidate polymer fillers for energetic capsule testing.

5.3.2 Energetic Capsule Fabrication and Characterization

Energetic capsules were fabricated using two extrusion die designs. The designs were termed Energetic Capsule 1 (EC1) and Energetic Capsule 2 (EC2). The design cross-sections are shown in Figure 5.2. Both designs maintain a 25 mm circular cross-sectional area with triangular cell shapes. EC1 has a graded structure with a high density of small triangular cells at the perimeter of the cross-section, larger triangular cells inside,

and a hollow, cylindrical center section. EC2 has a more uniform cross-section with uniform triangular cells surrounding a crosshatched central cylinder. The crosshatching was added to improve roundness of specimens by providing increased rigidity and support for handling during extrusion. The EC1 and EC2 designs yield extrusions with a relative density of 33% and 25%, respectively.

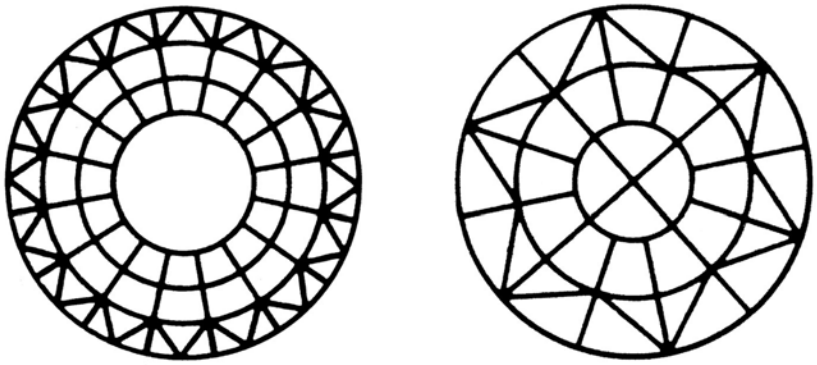

Figure 5.2 – Cross-sectional view of energetic capsule designs. Relative densities of designs 1 and 2 were 33% and 25%, respectively.

The overall fabrication process was similar to that described in Chapter 2. The appropriate powders for each composition were dry-mixed with A4M methocellulose. Liquid phase consisting of water and lubricant was added and the mixture was granulated using a conventional food processor. The granulated mixture was compounded into a paste using a high shear mixer and extruded through the energetic capsule dies. Extrusions were cradled in specially-made foam supports with 12.5 mm radius half-cylinders cut along the length of the support. The extrusions were laid in the foam supports and covered with a mating piece of foam to completely surround the extrusion. The foam served to maintain straightness and roundness of the LCAs while promoting uniform drying by limiting water vapor transport through the foam material. After 48 hours, the extrusions were removed from the foam supports and placed in a convection

dryer for the remainder of the drying process. The green extrusions were finally cut down to a maximum of 36 cm due to size constraints of thermal processing and placed on kiln furniture with similar half cylinder cut-outs for support during the reduction process. The extrusions were heated to 1350°C in hydrogen and held for 10 hours. The fully reduced LCAs were cut to length for both quasi-static and dynamic loading. Super Invar specimens were tested in the as-reduced state or partially transformed state after cryogenically treating with liquid nitrogen. Maraging 200 steel specimens were thermally treated at 480°C for 5 hours to achieve maximum strength.

With the fabrication of the energetic capsule materials complete, the process of infiltration with epoxy filler was addressed. The epoxy was a two-part system consisting of Epon 826 resin and diethonalamine hardener mixed in a 12:1 ratio. The resin was heated to approximately 70°C prior to mixing to lower the viscosity and promote pouring and infiltration. Resin was added to the hardener to insure that there was a minimum 12:1 ratio. It was determined during early processing attempts that too much hardener, or hardener that was dated, could have profound effects on the mechanical behavior of the epoxy. Care was taken to extend the life of the hardener by storing in an argon glove box and maintaining the minimum mixture ratio. The resin and hardener were mixed using a hand drill with a mixing attachment. The components were mixed at high speed for 5 minutes. The mixture was placed in a vacuum chamber to de-aerate the epoxy. Samples of pure epoxy were cast in cylindrical molds for the purpose of determining the mechanical properties of the epoxy alone. The Al molds were 17 mm in diameter and 15.24 cm in length. LCA samples were prepared for epoxy infiltration by sealing off one end of the extrusion, and any other holes such as defects in the exterior walls, using foil

tape. The samples were covered completely with the tape and a reservoir created at the open end. Both the epoxy mixture and the taped samples were heated to 70°C to lower the epoxy viscosity and promote infiltration into the cells and wetting of the cell walls. The reservoir was filled with epoxy and the samples place in a vacuum chamber. The vacuum was cycled to remove air from the cells and allow influx of epoxy. Infiltrated samples were then held at 70°C for a minimum of 15 hours to allow the epoxy to cure fully. After removing the foil tape and excess epoxy the samples were cut to length for testing.

Samples were cut to length for quasi-static and dynamic testing using a diamond cut-off wheel. Specimens for quasi-static compression tests were cut to lengths of approximately 25.4 mm. Reverse Taylor test specimens were cut to a minimum 4:1 aspect ratio resulting in an average specimen length of 65 mm. To achieve flat, parallel loading surfaces the test samples were lapped using a 45 μm diamond slurry. Prior to testing sample dimensions were measured and recorded. For LCA samples an average diameter was recorded due to irregularities in sample roundness. Epoxy samples were turned on a lathe to attain a uniform diameter. All samples were weighed and the Archimedes method was used to determine density. Samples that were to be filled with epoxy were measured for density prior to and after filling.

5.3.3 Experimental Setup

Quasi-Static Compression

Compression tests were conducted using a screw-drive test frame with 50,000 pound load cell. Maraging 350 steel compression platens and a crosshead rate of 0.1 inch per minute were used for all tests. All samples were tested in compression along the

axial direction. Data, in the form of crosshead displacement and load, were collected via computer acquisition. Load data were converted to strain using the apparent cross-sectional area of the honeycomb and displacement data were converted to strain using the change in crosshead displacement divided by the original sample height. Visual records of the compression tests were made using a digital video capture system. Twenty-four frames were captured at an interval of 12 seconds to account for approximately 12.57 mm of crosshead travel, or 50% specimen strain.

Reverse Taylor Anvil Impact Test

Testing of energetic capsules in the dynamic regime was accomplished through a modified setup of the Taylor anvil impact test. In the classic Taylor test the test specimen acts as a projectile that is accelerated to impact a rigid body. The 80 mm bore single stage gas gun used in this research was better suited to a modified version of this test. The setup was reversed such that the test specimen became the target upon which a flat anvil plate projectile was impacted. Thus, the test setup is referred to as a reverse Taylor impact test. The projectile in this case was a machined aluminum cylinder approximately 125 mm long and 80 mm in diameter. Inset into the striking surface of the projectile was a 6 mm thick Maraging 350 steel plate with a hardness of approximately 60 HRC. This was used to insure that the projectile impact surface experienced only elastic strain. The target specimen was mounted in a plexiglass ring using a fast setting epoxy. The target ring itself was mounted to an adjustable ring inside the experiment chamber. This allowed for the laser alignment of the target impact surface and the projectile impact surface so that a planar impact would result. Because of the nature of the setup, the target is accelerated by the projectile upon impact rather than being decelerated by a rigid wall

as in the classic Taylor test. The target sample was decelerated without creating additional damage using a soft recovery tank filled with textiles to slow the target and projectile. Additionally, a wooden aperture was placed in the tank to slow the projectile, but allow the target to pass unimpeded. The aperture's purpose was to separate the projectile and target and prevent a secondary impact of the projectile and target within the recovery tank.

Instrumentation was also added in the experiment chamber to allow determination of projectile velocity and triggering of the high-speed digital camera. Attached to the gun muzzle was a velocity block consisting of 4 metal pins staggered across a Lucite block and protruding into the path of the projectile. Contact by the projectile with each pin triggered a series of counters to which the pins were wired. Using the distance between pins and the time between contacts an average velocity was calculated. High-speed digital image capture was similarly triggered. A fifth pin was located just ahead of the velocity pins to trigger two simultaneous camera flashes. A crush pin located off axis and protruding ahead of the target triggered the digital camera. Images of the setup are shown in Figure 5.3.

Digital image capture was performed using the Imacon 200 system. The system featured a camera unit with computer control and data acquisition. Once triggered the camera had the capability of capturing images every 50 ns up to a total of 16 frames, or at speeds of up to 200 million frames per second. Actual image capture intervals were calculated based on the predicted speed of the projectile and the desired time resolution. Prior to firing, a calibration image of the field of view was taken. This allowed each test

to be calibrated to its own field of view and data analysis more precise. An example of the timing schematic is shown in Figure 5.4.

Subsequent to each shot all shot parameters including velocity data, oscilloscope trigger data, and digital image data was saved for further analysis. Physical recovery of the projectile and target was a matter of separating textiles from the sample. In some cases the target did not remain intact so retrieval was aided by the use of magnetic separation.

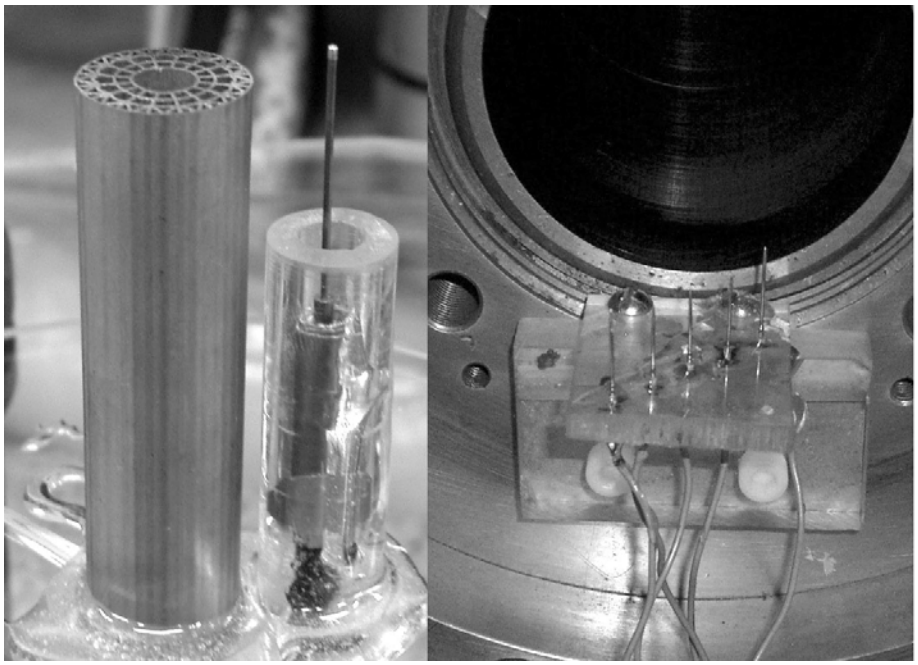

Figure 5.3 – Sample and instrumentation setup. Left, LCA mounted alongside camera trigger in target ring. Right, velocity pin cluster mounted to muzzle face.

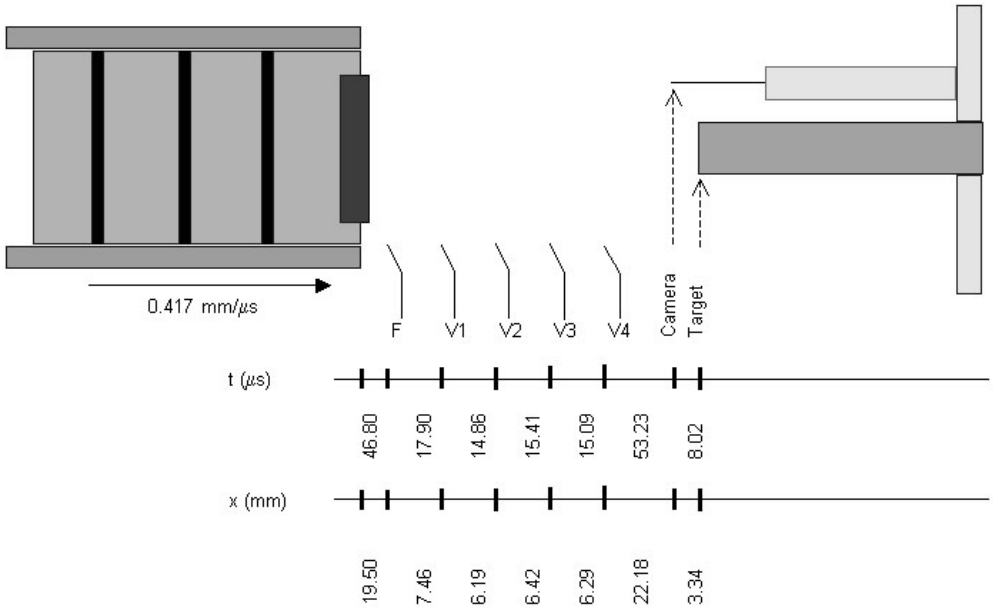

Figure 5.4 – Example timing schematic showing triggers for flash, velocity, and camera. Timing was based on predicted velocity of projectile and image capture considerations.

5.3.4 Data Analysis

Electronic data retrieved from the test instrumentation included velocity of the projectile and 16 frames of digital images. Velocity data was necessary to calculate the expected plastic wave speed, dynamic strength, and kinetic energy of the projectile. Digital image data was used in conjunction with digital image analysis software to estimate the actual plastic wave speed, strain rate, and strain prior to fragmentation. Strain was calculated from the change in length of the target sample. Additionally, the digital images were used to observe the failure mode of the samples that were damaged to the degree that there was very little sample left intact.

Physical recovery of test samples from the catch tank provided measurable values of length change and areal strain that were used to calculate dynamic strength for intact

specimens. Samples that were extensively fragmented were collected and a fragment distribution was determined using simple sieving techniques. Distributions could then be compared for the various test conditions.

5.4 Results and Discussion

5.4.1 Quasi-Static Results

Quasi-static compression behavior of the energetic capsule designs is presented in this section. Both Design 1 and Design 2 were tested in in-plane compression for a variety of conditions including alloy system, thermal treatment, and the presence of an epoxy filler. The focus, however, will be on the performance of energetic capsule Design 1 since this design was used in dynamic testing to be presented in subsequent sections. Results for Design 2 will be summarized and compared to Design 1. Stress-strain and energy absorption data for Design 2 can be found in Appendix C. Results of quasi-static testing are tabulated in Table 5.1.

Samples of pure epoxy were tested to determine the mechanical properties of the filler that would be used in the energetic LCA capsules. Cylindrical samples were prepared and tested in compression. The compression behavior for several samples is given in Figure 5.5. Variability among samples was a concern as initial testing showed different modes of failure. Some samples showed plasticity while others showed only brittle fracture. This was attributed to the aging of the hardener used in the epoxy and procedures for mixing the epoxy. Reproducibility was improved by using new hardener and insuring excess hardener was not used. The average yield strength of the material was 112 MPa. Density of the epoxy was determined to be 1.197 g/cc. An elastic

modulus of 5.528 GPa and a shear modulus of 2.054 GPa were determined using sound speed measurements.

Stress-strain behavior for the annealed Super Invar capsules in the filled and unfilled conditions is shown in Figure 5.6. The density of the unfilled samples was calculated to be 2.62 g/cc while the filler raised the density to 3.41 g/cc. Yield strength of the capsule was increased by 19% from 105 MPa to 126 MPa by filling with epoxy. The maximum stress after yielding also increased with the addition of filler from 203 MPa to 308 MPa. The compression of the unfilled samples showed uniform buckling and collapse consistent with a cellular material while the filled samples showed barreling and splitting of the exterior walls of the LCA, Figure 5.7. This was expected since the LCA cell walls were unable to buckle and collapse internally due to the presence of the epoxy filler. As expected the energy absorption was also improved by the addition of the polymer filler, Figure 5.8. Energy absorbed at 40% strain was 104 J/cc which was 55% higher for the filled samples than that for the unfilled samples. Filled LCA samples also showed higher strength properties than pure epoxy. Yield strengths for the two systems were essentially the same, but the strength of the LCA was almost 3 times higher that of the pure epoxy.

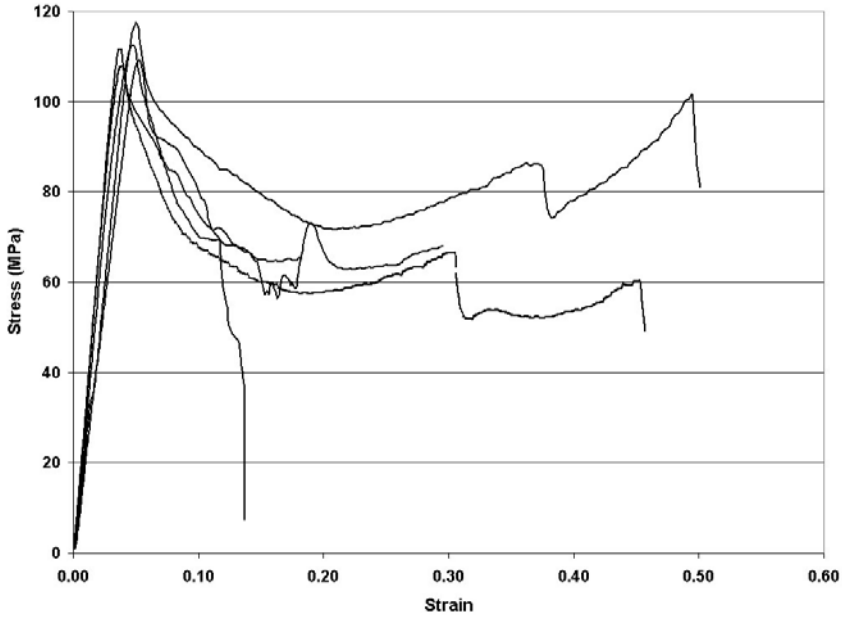

Figure 5.5 – Quasi-static compression results for pure epoxy samples.

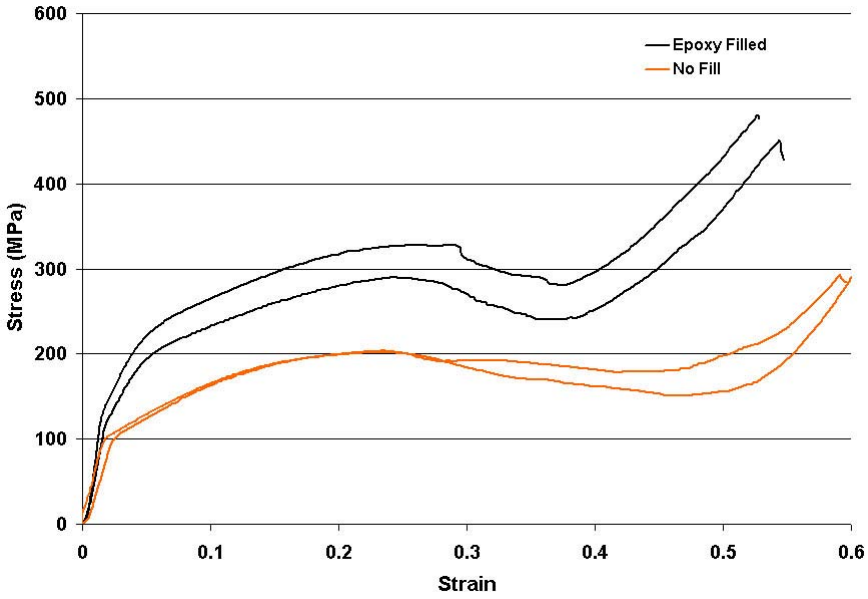

Figure 5.6 – Stress-strain behavior for annealed Super Invar energetic capsule Design 1 in the filled and unfilled condition.

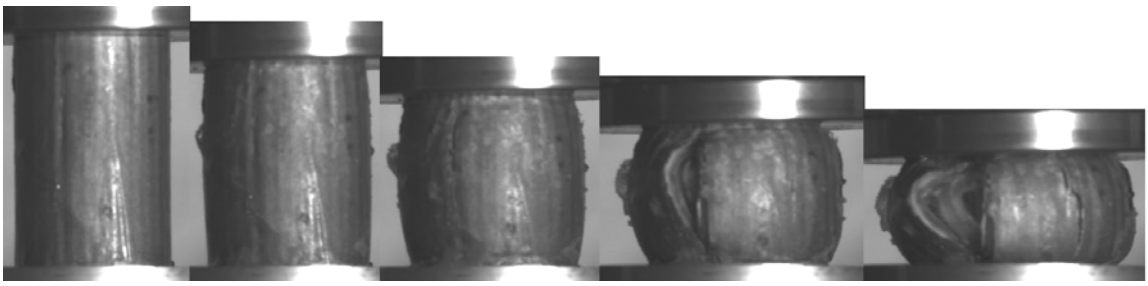

Figure 5.7 – Compression behavior of filled Super Invar LCA capsule.

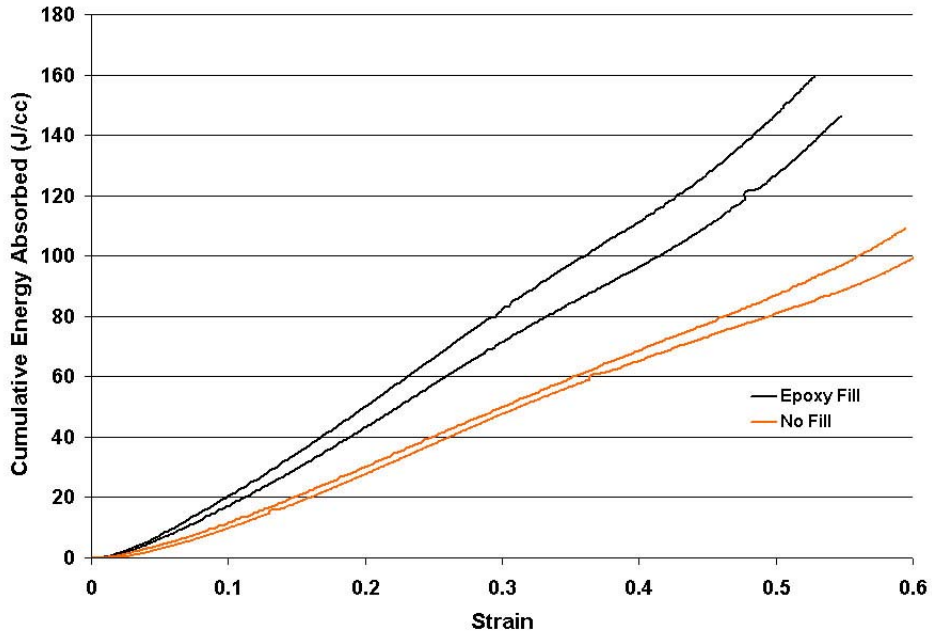

Figure 5.8 – Energy absorption for annealed Super Invar energetic capsule Design 1 in the filled and unfilled condition.

Stress-strain behavior for the Maraging 200 capsule in the filled and unfilled condition is shown in Figure 5.9. Densities for these samples were 2.52 and 3.34 g/cc for filled and unfilled conditions, respectively. The maraging alloy showed a higher strength than the Super Invar due to the much greater intrinsic strength of the cell walls. Unfilled samples yielded at 421 MPa while filled samples yielded at 451 MPa. The unfilled capsule had a plateau strength of 330 MPa despite brittle fracture at the platen surface. The filled samples had maximum strengths of 561 MPa over a range of approximately 10% strain before brittle fracture and shearing caused a load drop to 200 MPa where

reloading of fractured halves occurred. The maraging samples absorbed 132 and 125 J/cc in the unfilled and filled conditions, respectively, Figure 5.10. The brittle failure of the filled sample caused the energy absorption to lag behind that of the unfilled sample at strains greater than 27%. Like the Super Invar alloy, the maraging alloy LCA added significant static strength to the epoxy system, quadrupling the overall strength.

The performance of all the samples tested in quasi-static compression is summarized in Table 5.1. In general the higher relative density of capsule design 1 as compared to design 2 resulted in higher overall strengths and energy absorption values for design 1. The upper bound predicted for the out-of-plane yield strength, $\frac{\left(\sigma_{pl}^{*}\right)_3}{\sigma_{ys}} = \left(\frac{\rho^{*}}{\rho_S}\right)$, still applies to the behavior of these honeycomb capsules. For the annealed Super Invar and the M200 alloy in both capsule designs, the predicted values were exceeded. For the hardened Super Invar in both capsule designs, the predicted values were higher than seen in the data.

The epoxy-filled capsules benefited from the fill material with increased overall strengths and energy absorption capabilities with respect to the unfilled. The filler also altered the failure mode of the capsules by preventing buckling of the inner cell walls. This was also responsible for the disappearance of the plateau regime seen in cellular materials. LCA capsules also improved the static performance of the energetic system over the epoxy alone.

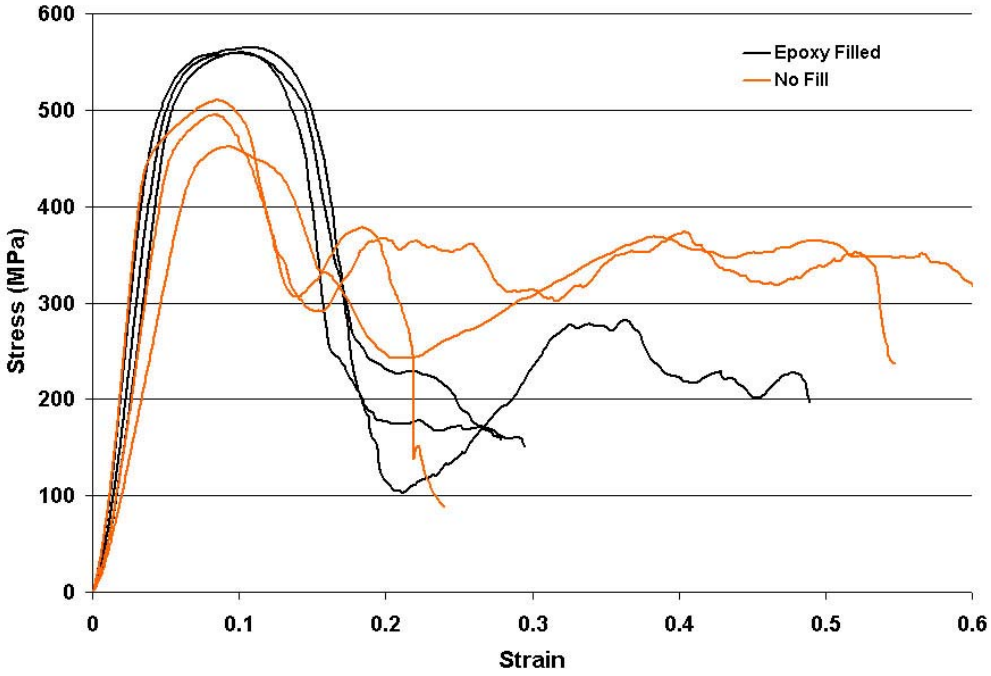

Figure 5.9 – Stress-strain behavior for maraging 200 energetic capsule Design 1 in the filled and unfilled condition.

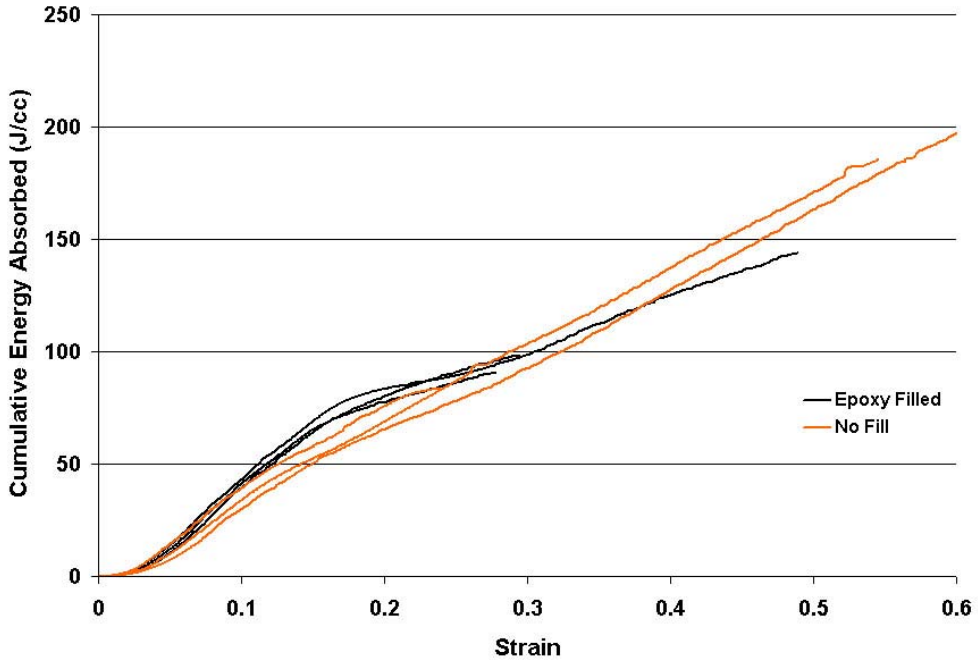

Figure 5.10 – Energy absorption for maraging 200 energetic capsule Design 1 in the filled and unfilled condition.

Table 5.1 – Quasi-static compressive properties of the energetic capsule designs investigated.

	Energetic Capsule Designs							
	1				2			
	σ_{pl} (MPa)	σ_{Max} (MPa)	$\sigma_{Plateau}$ (MPa)	E_A @ 0.4ε (J/cc)	σ_{pl} (MPa)	σ_{Max} (MPa)	$\sigma_{Plateau}$ (MPa)	E_A @ 0.4ε (J/cc)
No Fill								
M200	421	488	330	132	314	346	230	91
Hardened Super Invar	132	256	200	79	139	191	154	60
Annealed Super Invar	105	202	175	67	78	106	89	36
Epoxy Fill								
M200	451	560	--	125	365	471	--	102 @ 0.37ε
Hardened Super Invar	164	337	--	104	169	268	--	91
Annealed Super Invar	126	308	--	104	109	198	--	72

5.4.2 Post-Mortem Analysis of Dynamic Test Samples

LCA capsules were tested at three different velocities. Initials tests on copper rod and Super Invar capsules were performed at low velocity (~100 m/s). Using data for quasi-static and dynamic tests and assuming a linear relationship between velocity and strain, a maximum velocity was chosen to achieve the maximum strain of 40% allowed for a valid Taylor test. This was approximated to be ~700 m/s. This test was performed on a filled Super Invar sample. The result was a near complete pulverization of the sample. Consequently, a middle velocity range was chosen at ~400 m/s for the remainder of testing which included filled and unfilled Super Invar and filled M200 maraging steel. The following results were derived from physical specimens after recovery as well as from image capture data where possible. Data for all tests is summarized in Table 5.2.

Low velocity samples were recovered intact from the catch tank. The deformation is visible in Figure 5.11 for the copper reference and the two LCA samples. The samples show the classic Taylor deformation pattern in which the impact face was radially enlarged as the plastic wave traveled into the samples. Additional damage was visible on the side of each sample due to secondary impact of the samples in the catch tank. The greatest damage was to the unfilled LCA sample since it had a low in-plane strength. The damage obscured the radial enlargement of the impact face, but did not significantly affect measurements for strain from length dimensions. The copper reference showed the largest apparent deformation region and the largest strain as determined by length change to be 11%. The Super Invar LCA samples showed lesser deformation with strains for the unfilled and filled conditions of 7.2 and 6.8%, respectively. The Wilkins-Guinan analysis was used to calculate the dynamic yield strength for each sample. Copper was calculated to have a dynamic yield stress of ~550 MPa at a strain rate of 900 s^{-1}. The Super Invar capsules showed dynamic yield strengths of 240 and 326 MPa for unfilled and filled conditions, respectively, at a strain rate of approximately 1000 s^{-1}. Energy absorption was calculated using the area under the stress-strain curve for each yield strength assuming a linear elastic relationship and a strain level calculated from the final dimensions of the specimen after impact. The energy absorption of the copper was the highest at 30 J/cc followed by the epoxy filled LCA and unfilled LCA with 11 and 8.6 J/cc, respectively. It was also noted that the epoxy in the epoxy-filled LCA was protruding from the cells of impact face by as much 1.5 mm for the large central cavity. This implied that the epoxy-cell wall interface was

not strong enough to prevent some amount of recovery by the epoxy. Digital image data for the copper rod and the epoxy-filled Super Invar capsule are presented in Appendix C.

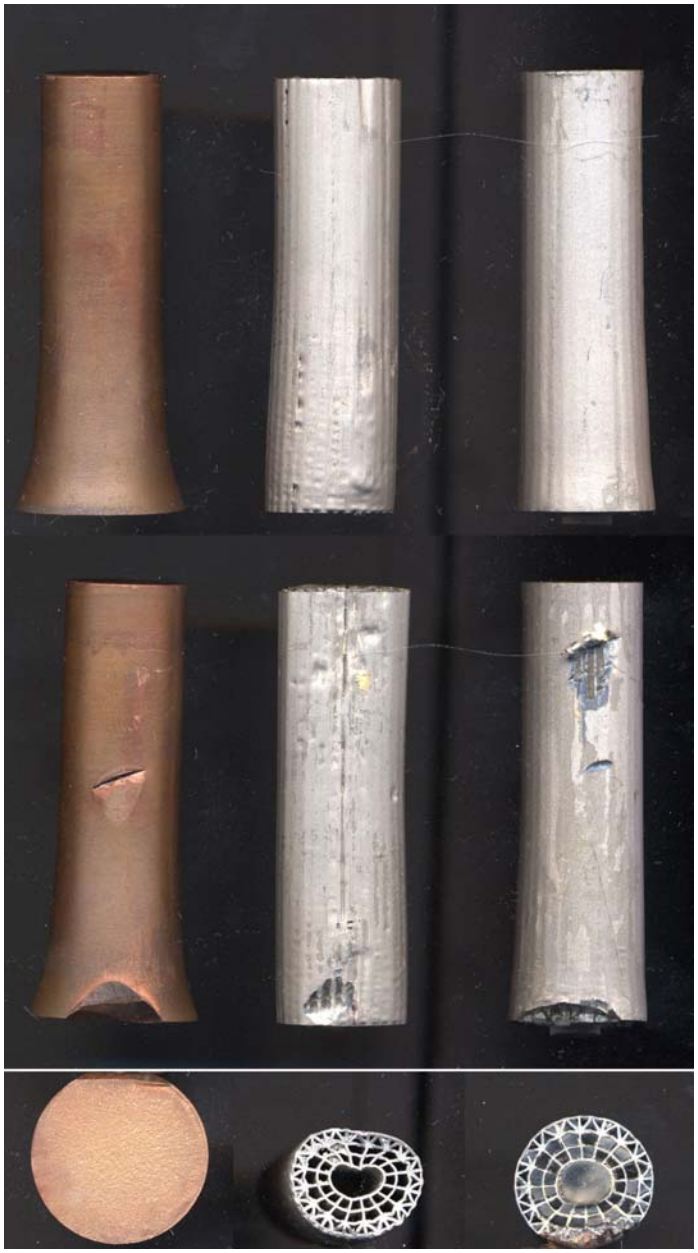

Figure 5.11 – Recovered samples from low velocity impacts. Left - copper rod; center – unfilled, annealed Super Invar; right – filled, annealed Super Invar.

The epoxy-filled LCA sample that was impacted at a velocity of 733 m/s was not recovered intact. The sample was completely fragmented by the impact of the projectile.

The sample fragments were recovered with the aid of magnets resulting in the recovery of approximately 19.4% by mass of the original specimen. Fragment distribution was calculated and will be presented in section 5.4.3. Digital imaging failed to activate during this test so no other data could be extracted from this test.

Three samples were tested at the mid-range velocity of 400 m/s. Two Super Invar LCAs, in the filled and unfilled condition, and one M200 LCA in the filled condition were tested in this regime. Digital image data recorded for each shot (provided in Appendix C) showed fragmentation early in the deformation process for each sample. Since fragmentation invalidates the assumptions of the Taylor test and Wilkins-Guinan analysis, data for calculating the dynamic yield strength was derived from image analysis on frames in the early stages of fragmentation. It was assumed that at this point the plastic zone was established and Taylor analysis should yield valid data. For the Super Invar samples a strain of 17% for the unfilled and 15% for the filled capsule was determined from the digital images and used for calculation. The unfilled capsule at 17% strain was calculated to have a dynamic yield strength of 1310 MPa at a strain rate of 6600 s^{-1}. This sample was observed to fragment by splitting axially and peeling away at the impact face. Energy absorption was calculated at 109 J/cc. The epoxy-filled Super Invar capsule was calculated to have a dynamic yield strength of 1783 MPa at a strain rate of 6100 s^{-1}. Energy absorption was calculated to be 134 J/cc. This sample fragmented as well. The epoxy filler and LCA fragments was observed ejecting radially at the impact face as the LCA was split and fragmented. Also, of note from the digital image data was the ejection of the epoxy core in the latter stages of the test. As the remaining intact portion of the LCA broke away from the target and was accelerated by

the oncoming projectile a large portion of the epoxy from the center cavity, approximately half the original length of the sample, was ejected and accelerated away from the sample at very high speed relative to the projectile.

The impact test of the epoxy-filled M200 capsule showed similar behavior to the Super Invar in terms of fragmentation in the 400 m/s regime. Due to this fragmentation event and the poor resolution of early tests, image capture was adjusted to focus on the leading half of the target and backlighting was used to provide better contrast and resolution for analysis. Images used for analysis are shown in Figure 5.12. The original images can be viewed in Appendix C. The improved imaging allowed accurate measurement of length change between frames and, consequently, a dynamic yield strength and strain rate over each frame interval. The stress-strain analysis for the M200 shot, Figure 5.13, showed how the apparent dynamic yield strength decreased as the sample was reduced in length as dictated by the Wilkins-Guinan relationship. The dynamic yield strength reported here was calculated at the strain level chosen from image capture data. In this case, excessive fragmentation began in Frame 6 where strain was approximately 8%. At that point, the plastic portion of the sample appeared to be stable with respect to latter frames. Using this strain value, a dynamic strength of 3191 MPa was calculated at a strain rate of approximately 6000 s^{-1}. Subsequent to frame 6 the change in length of the capsule (denoted as increased strain in Figure 5.13) was due to fragmentation and loss of mass rather than an increased length of the plastic zone. It may be argued, therefore, that this stress was maintained through the entirety of the test since deformation continued until the sample left the target ring. However, a conservative estimate of the stress-strain response was adopted for energy absorption purposes by

assuming a linear slope to the yield point and a post-yield behavior consistent with the Wilkins-Guinan relationship. The energy absorption associated with this stress-strain relationship is shown in Figure 5.14. The M200 capsule showed a slightly lower energy absorption on yield than the Super Invar at 131 J/cc, but this occurred at a strain value half that of the Super Invar. Also available for comparison in Figures 5.13 and 5.14, is the performance of a pure epoxy sample. A strain of 17% was chosen from the image data for analysis. The dynamic yield strength for the epoxy at this strain was calculated to be 600 MPa with an energy absorption of approximately 50 J/cc.

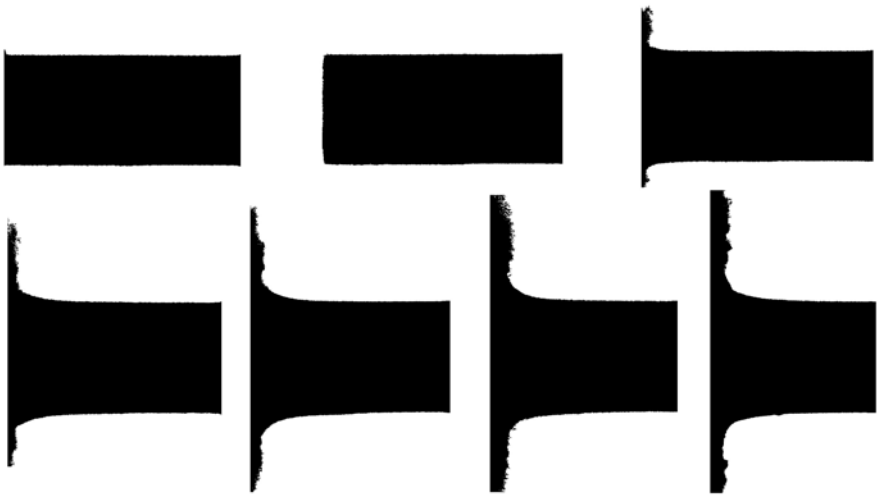

Figure 5.12 – Threshold images used for analysis of M200 impact. Frames 2 (top, left) through 8 (bottom, right) are displayed.

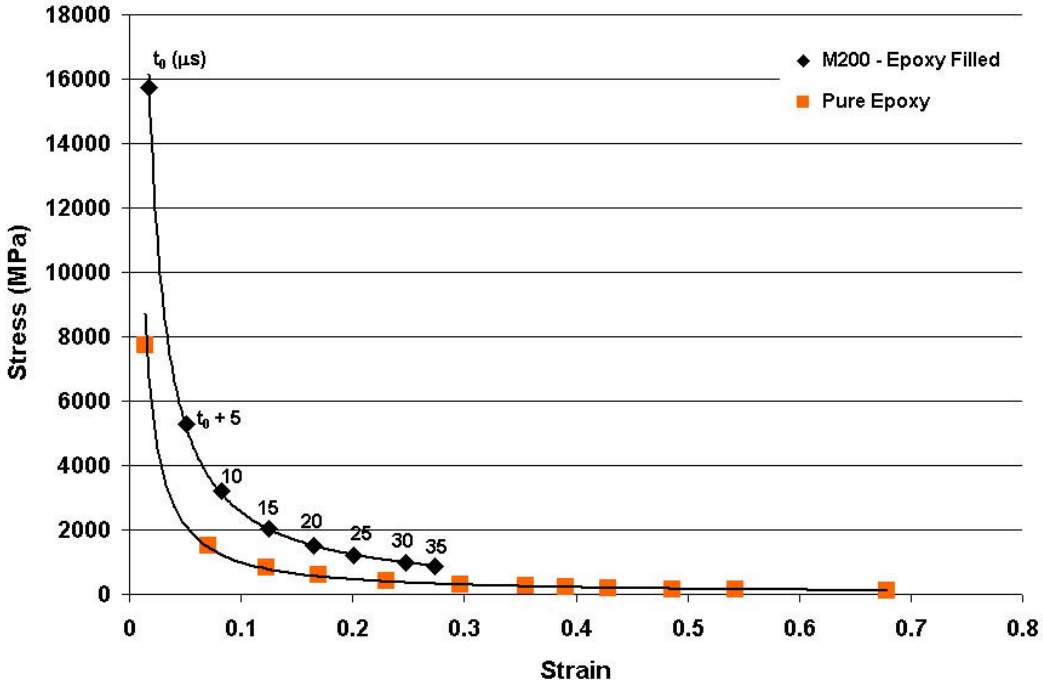

Figure 5.13 – Stress-strain behavior for epoxy-filled M200 and pure epoxy as determined by digital image analysis.

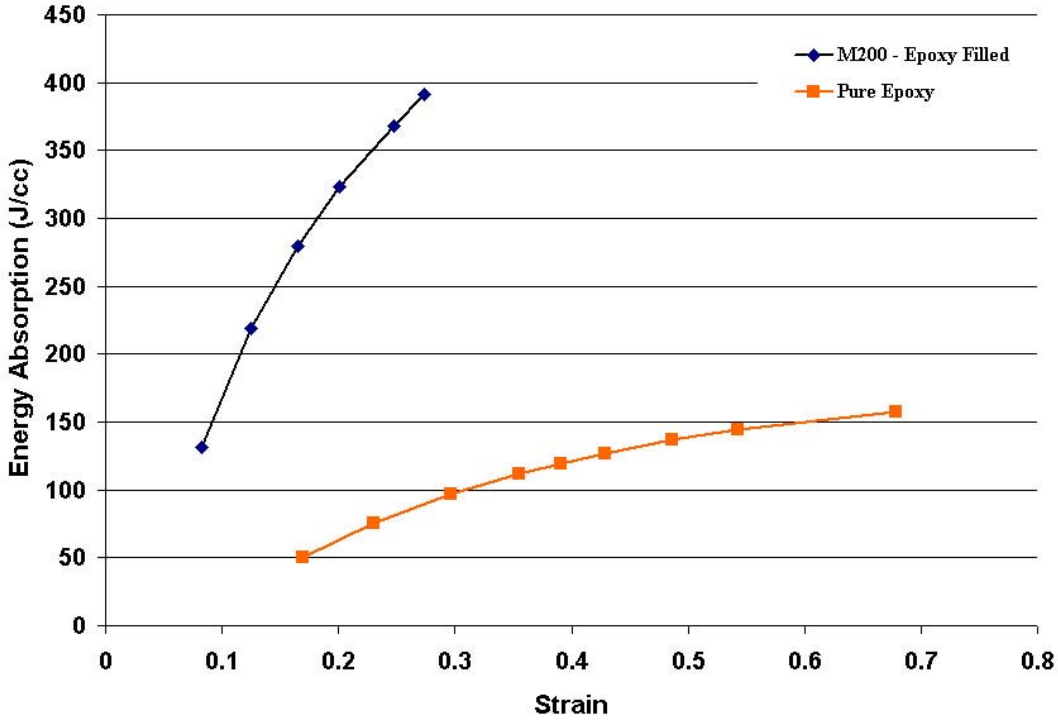

Figure 5.14 – Energy absorption of epoxy-filled M200 and pure epoxy as calculated from stress-strain values.

Table 5.2 – Properties of LCA energetic capsules as determined by dynamic testing using the reverse Taylor anvil impact test.

Material	Impact Velocity (m/s)	Density (g/cc)	Strain	Strain Rate (s^{-1})	Dynamic Yield Stress (MPa)	Energy of Plastic Deformation (J/cc)	Post-Mortem Target Mass (g)
Copper	119.74	8.96	11.0%	889.24	550	30	143.2 (100%)
Super Invar - No Filler	117.05	2.61	7.2%	N/A	240	8.6	35.38 (100%)
Super Invar - Epoxy Filler	118.70	3.23	6.8%	1089.14	326	11	45.59 (100%)
Super Invar - No Filler	416.70	2.74	17%	6628	1310	109	19.17 (45.9%)
Super Invar - Epoxy Filler	419.10	3.30	15%	6120	1783	134	27.95 (62.8%)
M200 - Epoxy Filler	407.10	3.31	8%	6000	3191	131	28.61 (65.2%)
Super Invar - Epoxy Filler	733.00	2.60	N/A	N/A	N/A	N/A	16.89 (19.4%)
Epoxy Filler	427.01	1.19	17%	6000	595	50	--

Based on available data from impact testing, Figure 5.15, the LCA capsules significantly increased the dynamic strength of the energetic system as compared to epoxy alone. Dynamic strength was increased 3 to 5 times over that of pure epoxy. The strengthening effect appears to be additive when considering the case of the Super Invar LCA at approximately 6000 s^{-1}. Adopting a rule of mixtures approach for the epoxy filler at 67 vol% and adding to the strength of the unfilled capsule, the predicted dynamic yield strength of the system is within 5% of the experimentally determined value. At just 33% relative density, the LCA leaves a significant volume of space for filler material to be used for energetic purposes. The LCA capsules also give the energetic system significant strength increases at low strain rates which can help prevent accidental damage to the system prior to impact.

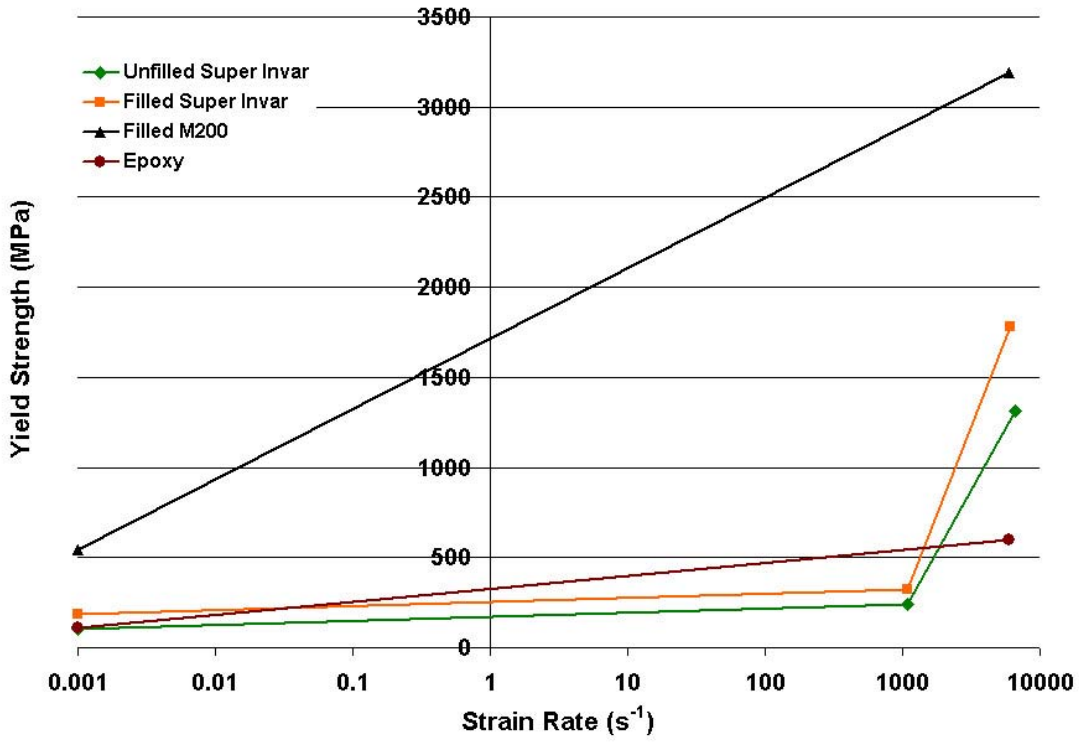

Figure 5.15 – Yield strength is improved for filled systems as compared to epoxy without encapsulation.

5.4.3 Fragmentation Analysis

Fragments that were collected from the medium and high velocity shots were sieved and their cumulative mass distributions plotted, Figure 5.16. The distribution showed that the highest strain rate test at 700 m/s had the smallest average fragment size of 1.5 mm. This was followed by the filled Super Invar at 400 m/s with an average of 3.5 mm and the filled M200 with an average size of 10 mm. This result was somewhat misleading due to the recovery of some large fragments that retained significant volumes of epoxy from the M200 test. Consequently, the mass distribution was skewed towards higher average fragment size despite a size range that dipped below that of the filled Super Invar. Finally, the unfilled Super Invar showed the largest fragment size profile though the distribution was also skewed by the recovery of a significantly larger

fragment. The profile order fits reasonably well with Mott's and Kipp and Grady's predictions. The highest strain rate did result in the smallest fragment as predicted by Kipp and Grady. There is some justification for the filled Super Invar to have a similar fragment size to the M200 based on Mott's analysis. Since the M200 alloy has a higher fracture strength and low work-hardenability it would be expected to produce small fragments. However, it failed at a lower strain than the Super Invar which points to smaller fragments for the Super Invar. The presence of the filler has a definite effect on the fragment size. All three samples with filler showed much lower fragment sizes than the unfilled sample. This was attributed to the differences in compressibility of the two materials leading to radial stresses and significant tensile and shear forces.

The cumulative mass distribution obfuscates the distribution of small fragments due to the significant mass of the larger fragments, especially those that retain filler within intact cells. Assuming a cubic volume for the fragments, a number distribution can be calculated based on the mass, density, and size of fragments. This assumption is reasonably accurate at fragment sizes approaching the cell wall thickness. For larger, non-uniform fragments the conversion will underestimate the number of fragments. However, the total number of larger fragments is a much smaller overall percentage of the distribution as compared to the small fragments. The cumulative number distribution gives a better indication of the relation of fragment size to cell size. For the filled samples, the average fragment size is on the order of the cell wall thickness, or ~300 μm. The unfilled sample distribution points to fragment sizes on the order of the cell wall length, or ~1.5 mm. The number distribution also shows a lower overall distribution for the more brittle M200 alloy than the Super Invar at the same strain rate. The highest

strain rate test showed comparable results to the lower strain rate Super Invar, but only 20% of the target mass was retrievable as compared to 60% for the lower strain rate tests.

The fragment distributions are also consistent with visual inspection of the fragments. Fragments from the unfilled sample were elongated strips or large collapsed sections of the cellular material. Fragments from the filled samples typically were very fine with a small number of large fragments. The large fragments retained some intact cells from the outer most ring of triangular cells many of which still contained the filler material. The fracture surfaces of the 700 m/s filled fragments display both tensile type and shear type failures, Figure 5.17. This was expected due to the high velocity impact and the resulting radial stresses from filler compression and cell wall extension.

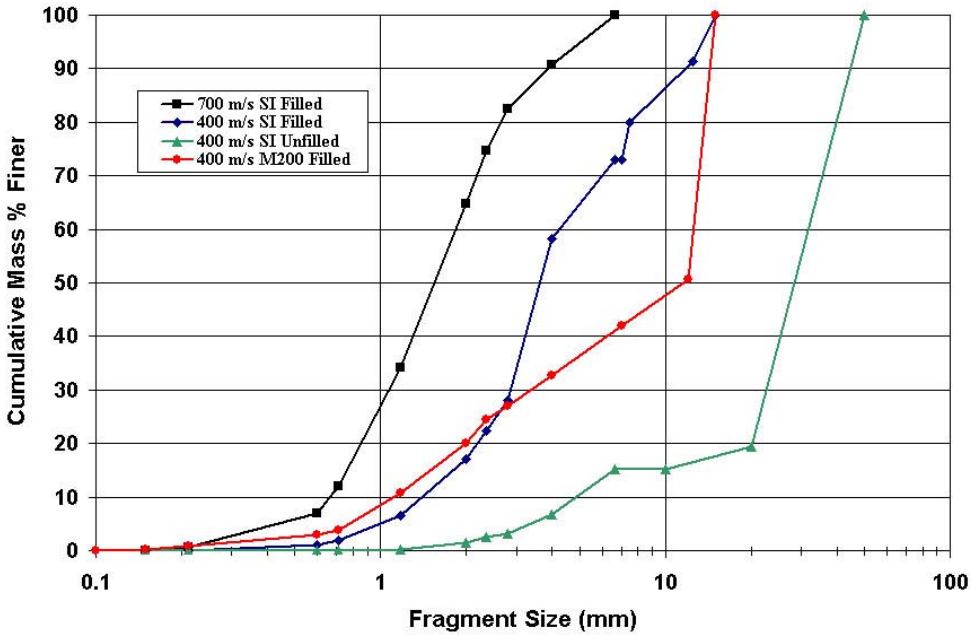

Figure 5.16 – Distribution profile of fragment sizes for reverse Taylor tests.

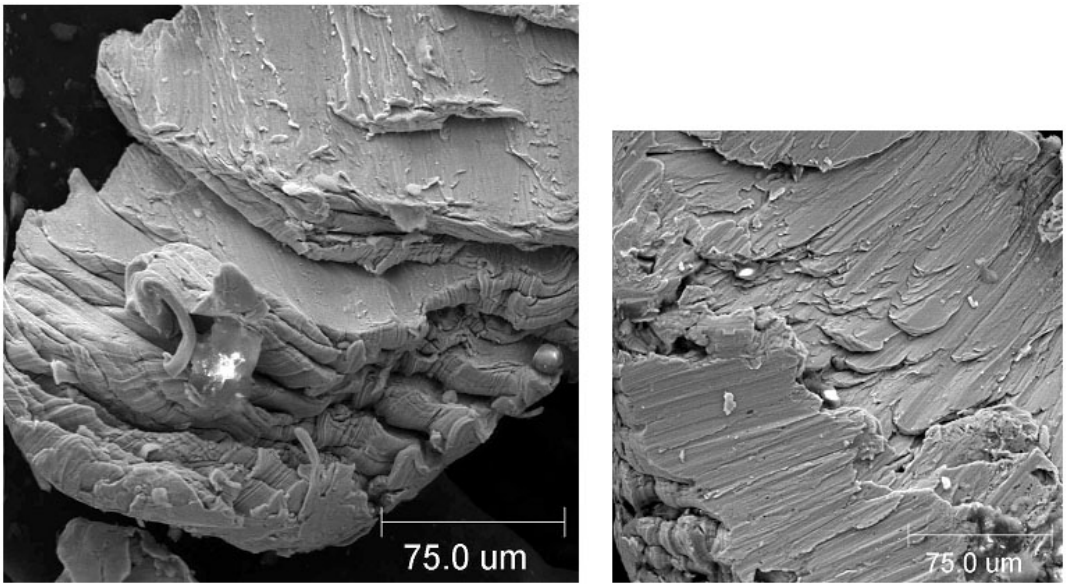

Figure 5.17 – Images of fragment surfaces show damage consistent with fragmentation event including both tensile and shear failure.

5.4.4 Suitability of LCAs for Energetic Capsule Applications

The suitability of LCAs as energetic capsule depends on their ability to deliver the energetic materials to their destination and whether they will aid or hinder the reaction of the materials. From the dynamic tests presented thus far, the addition of the LCA capsule to the epoxy system significantly increases the dynamic strength as compared to epoxy alone. This will certainly aid in the successful delivery of the material to its target. Data also suggest that the LCA will aid in the initiation of the energetic reaction. The calculated dynamic yield strength for the M200 LCA with filler material approaches pressures required for the initiation of some energetic reactants such as Ni+Ti. Investigation of Hugoniot data and impedance matching techniques, Table 5.3, shows that pressures of 4 GPa are possible at the impact face for a velocity of ~400 m/s.

Increasing the velocity to 700 m/s should generate initial pressure conditions exceeding 8 GPa.

Fragmentation at medium velocities excludes the LCA capsule from unaided penetrator applications. Fragmentation does have a positive aspect, however. Many energetic systems require both high pressures and shearing action to initiate and sustain the reaction. Fragmentation events such as those seen in the filled LCA impact will generate significant shearing. Related data point to a relationship between fragment size and cell wall thickness for the filled samples. Depending on the desired fragmentation event, the LCA can be tailored to generate a specific fragment size range by adjusting the cell wall thickness. It was also shown that cell size had an effect on the retention of the filler materials. Larger cell sizes may result in filler decoupling from the cell walls during acceleration or impact which may adversely affect reaction propagation. Thus, cell size may also be tailored based on application requirements.

LCAs offer significant static and dynamic stability to the energetic system. The fracture and fragmentation of the capsule system generates significant shear and pressures not seen in epoxy alone. The combination of fragmentation and increased impact pressures certainly makes LCAs candidates for energetic capsules.

Table 5.3 – Equation of State parameters and calculated impact pressures for reverse Taylor tests.

Projectile		Equation of State Parameters	M200 + Epoxy	
C_0 (km/s)	4.2511		C_0 (km/s)	3.8618
S_1	1.4601		S_1	1.5211
ρ (g/cc)	8.129		ρ (g/cc)	3.34
Super Invar + Epoxy			Epoxy	
C_0 (km/s)	3.7406		C_0 (km/s)	2.5094
S_1	1.5456		S_1	1.7329
ρ (g/cc)	3.41		ρ (g/cc)	1.197
	V (km/s)	U_P (km/s)	P (GPa)	U_S (km/s)
M200 + Epoxy	0.407	0.289	4.2	4.30
SI + Epoxy	0.119	0.087	1.1	5.09
SI + Epoxy	0.419	0.3	4.3	4.20
SI + Epoxy	0.733	0.518	8.1	4.54
Epoxy	0.427	0.388	1.5	3.18

5.5 Conclusions

In this section the dynamic behavior of LCAs was investigated as it relates to their suitability for applications such as energetic capsules or penetrators. Epoxy was used to simulate the mechanical response of energetic filler. Two capsule designs were tested in quasi-static compression with multiple alloy and fill conditions. Dynamic testing was accomplished using a reverse Taylor anvil impact test to achieve strain rates greater than 6000 s^{-1}.

Quasi-static compression testing showed improved yield strengths for filled samples as compared to pure epoxy samples. Energy absorption was significantly improved as well. The presence of the epoxy altered the mode of failure of the LCA by preventing buckling and collapse consistent with cellular materials. Barreling and

splitting of cell walls was predominant for the ductile LCA material, while fracture and shearing was seen in the brittle materials. Addition of the LCA to the energetic system served to significantly increase the quasi-static strength and energy absorption of the system. This effectively gives the system greater stability during storage and handling.

Dynamic testing showed that by encapsulating the energetic filler in a cellular material such as an LCA, the pressures generated at the capsule impact face could be increased by a factor of 3 at the same velocity and a factor of more than 5 at higher velocities. Further, the fragmentation of the capsule system provides an additional element of shear that can aid in initiation of the energetic reaction. The LCA alloy may also be tailored to control fragment size through alloy choice and geometry considerations such as cell size and wall thickness. While these compositions are likely not suitable for penetrator applications, the LCA provides added stability to the system by increasing the dynamic strength.

Chapter 6

Conclusions

Investigation of cellular materials has led to significant efforts in fabricating and characterizing different types of cellular material such as foam and honeycomb. In this paper a chemo-powder process was introduced as a means to fabricate honeycombs known as Linear Cellular Alloys. The process was validated through characterization of bulk alloy, fabrication of LCAs of multiple geometries and alloys, and quasi-static and dynamic performance of LCAs.

Alloys fabricated by the chemo-powder process have been characterized and compared to wrought alloys of the same or similar compositions. From a microstructural standpoint, the alloys showed all the features expected. The Super Invar alloys showed the single-phase austenitic microstructure in the annealed condition and the two-phase austenitic/martensitic microstructure in the hardened condition. Similarly, the maraging steel compositions showed the characteristic lathe-type martensitic structure. As expected, porosity was also found uniformly distributed throughout the material. Pores due to extrusion defects were easily identifiable as they were much larger than surrounding pores and often times stretched out along the extrusion direction. Homogeneity of the alloys was confirmed through EDS. No segregation was visible on the length scales resolved by the equipment.

Mechanical properties were investigated and compared to available wrought values. The presence of porosity was found to degrade the performance of alloys tested.

Measured values were therefore compared to predicted values calculated on the basis of a minimum solid area model. Super Invar in the annealed condition met or exceeded predictions. Super Invar in the hardened condition had no basis for comparison since no data is published on the properties of the partially transformed alloy. The maraging compositions tested showed a dependence on the amount of Ti content in the alloy. The lower Ti content M200 alloy showed good correlation with predicted values. The higher Ti content M350 alloy was significantly lower in strength than predicted. It was postulated that only partial incorporation of the Ti component is occurring due to high probability of reoxidation. This was confirmed using XRD and uniaxial testing. Because significant strengthening was still achieved with the addition of TiH_2 to the maraging compositions, the hydride was used in all subsequent maraging compositions. Study of the fracture surfaces for Super Invar and maraging alloys revealed consistent, shared features such as dimpling, pores from extrusion defects, and second phase particles. The particles were identified as impurities common to the raw materials.

Paste processing was also shown to affect properties of the bulk materials due to defects associated with extrusions. Poor paste mixing results in a non-homogenous paste not suited to defect-free extrusions. Inhomogeneities in the paste correlated to increased porosity from unmixed binder and defects through poor paste rheology.

The results of characterization show that chemo-powder processed alloys compare well to wrought alloys when porosity is taken into account. Several steps can be taken to improve alloy properties including optimizing paste rheology and using good judgment in alloy selection. Use of high purity raw materials and good control over furnace atmosphere during reduction and sintering can reduce impurities that may affect

overall performance. A comprehensive list of mechanical properties can be found in Appendix A as well as CTE data of annealed Super Invar and M200 alloys for further reference.

Metal honeycombs fabricated using the powder processing technique have been shown to perform near or above levels predicted by available models. Out-of-plane behavior was consistent with existing models for yield strength and mean crushing strength. In-plane performance was adversely affected by the presence of defects such as missing cell walls, cell wall corrugation, and rippling of the LCA skin. Consequently, in-plane performance did not meet the predictions of the models. The overall performance of the triangular LCA showed good energy absorption due to high plastic buckling strengths and plateau strengths. In-plane performance showed good energy absorption as well, but in general did not exceed the performance of some metal foam. Energy absorptions values ranging from 49 to 140 J/cc have been achieved from LCAs. Due to the small number of samples tested for each condition and geometry, the behavior of LCA honeycombs that has been presented must be tempered with a lack of statistical strength. However, the reproducibility among samples and close approximation to the models validates these conclusions. Overall, honeycombs fabricated using chemo-powder processing have been shown to have excellent mechanical properties, in many cases, exceeding those of metal foam and other honeycomb.

Dynamic behavior of LCAs were investigated as it relates to their suitability for applications such as energetic capsules or penetrators. Epoxy was used to simulate the mechanical response of energetic filler. Two capsule designs were tested in quasi-static

compression with multiple alloy and fill conditions. Dynamic testing was accomplished using a reverse Taylor anvil impact test to achieve strain rates greater than 6000 s^{-1}.

Quasi-static compression testing showed improved yield strengths for filled samples as compared to pure epoxy samples. Energy absorption was significantly improved as well. The presence of the epoxy altered the mode of failure of the LCA by preventing buckling and collapse consistent with cellular materials. Barreling and splitting of cell walls was predominant for the ductile LCA material, while fracture and shearing was seen in the brittle materials. Addition of the LCA to the energetic system served to significantly increase the quasi-static strength and energy absorption of the system. This gives the system greater stability when not in use.

Dynamic testing showed that by encapsulating the energetic filler in a cellular material such as an LCA, the pressures generated in the capsule could be increased by a factor of 3 at the same velocity and a factor of more than 5 at higher velocities. Further, the fragmentation of the capsule system provides an additional element of shear that can aid in initiation of the energetic reaction. The LCA alloy may also be tailored to control fragmentation as well by altering cell size and wall thickness. While the compositions tested are likely not suitable for penetrator applications, the LCA provides added stability to the system by increasing the dynamic strength.

The viability of Linear Cellular Alloys generated from an oxide powder processing route was proven in this work. The processing route has been shown to produce bulk materials that show reproducible properties which compare very well to conventionally produced metals. The ability to fabricate multiple geometries and alloy systems was demonstrated and the properties of LCAs under quasi-static loading showed

good correlation to predicted properties as determined by numerous models. Finally, the suitability of LCAs as a multifunctional element in an energetic capsule application was predicted and demonstrated.

Chapter 7

Recommendations

The work presented in this study covered a broad range of alloys, geometries, and loading conditions. It also served a broad purpose which was to validate the LCA fabrication process with respect to conventional processing, characterize LCA behavior, and assess suitability of LCAs for dynamic applications. The conclusions reached also serve to generate more questions and recommendations for future research pursuits.

Bulk Alloy

It was shown that TiH_2, while successfully used to add Ti to the alloy, resulted in significant reoxidation. Further study of the conditions for reduction and incorporation in the alloy matrix may aid in the realization of full strength maraging alloys. This work can be extended to other alloying elements whose oxide is stable at typical processing temperatures opening the door for greater alloy diversity. Additionally, replacing the natural iron oxide powder with a synthetic would serve to eliminate a major source of impurities. However, this has significant implications on the rheology of the pastes due to different powder interactions and new batch compositions must be formulated.

Quasi-Static Behavior

Quasi-static behavior was addressed for a limited number of geometries and alloy combinations. Future testing efforts should center around one alloy and several geometries, or one geometry and several alloys. By holding one variable constant the effects of the other variable can be better determined. Also, the concept of a graded structure has been suggested, but not explored experimentally. The tailorable stress-

strain and energy absorption behavior of such a structure may prove useful for some applications.

Dynamic Behavior

The limited number of high strain rate tests restricted analysis to a small number of variables. More testing would allow determination of strain rate required for fragmentation and more complete yield strength versus strain rate relationship. Future testing should seek to experimentally determine the pressures generated on impact using the appropriate pressure gauges. This would be useful when considering the initiation of the energetic reaction. Dynamic behavior of the bulk LCA material should be investigated to provide better modeling data. This can be accomplished by using conventionally produced rod since fabrication of large cross-sections comparable to the LCAs studied would likely result in significant internal defects.

Appendix A

Bulk Alloy Characterization

Table A.1 – Summary of mechanical properties for chemo-powder processed alloys.

Material	UTS (MPa)	YTS (MPa)	Elongation (%)	Young's Modulus (GPa)
Super Invar Annealed	396.7 ± 14.3	261 ± 11.9	26.5 ± 3.6	122.1 ± 3.7
Super Invar Hardened	678.5 ± 5.2	414 ± 12.5	6.9 ± 0.9	126.9 ± 6.5
Maraging 200	1218.5 ± 41.0	1177.5 ± 32.36	3.5 ± 0.9	177.8 ± 7.0
Maraging 350	1661.6 ± 25.1	1522.3 ± 10.5	2.5 ± 0.5	N/A

Material	Shear Modulus (GPa)	n	Rockwell Hardness
Super Invar Annealed	47.87 ± 1.65	0.314 ± 0.011	57.9 ± 4.4 (B)
Super Invar Hardened	48.37 ± 3.14	N/A	79.3 ± 11.9 (B)
Maraging 200	70.2 ± 5.11	0.061 ± 0.003	33 ± 2 (C)

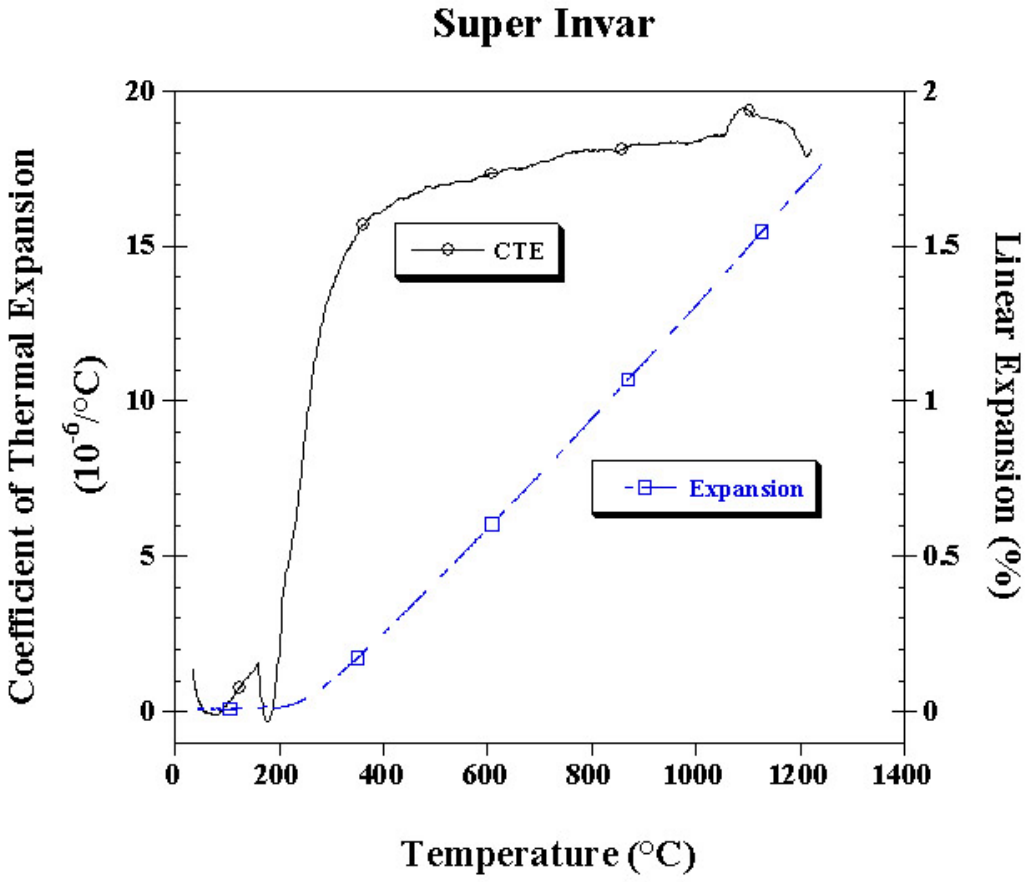

Figure A.1 – CTE and expansion data for as-reduced Super Invar.

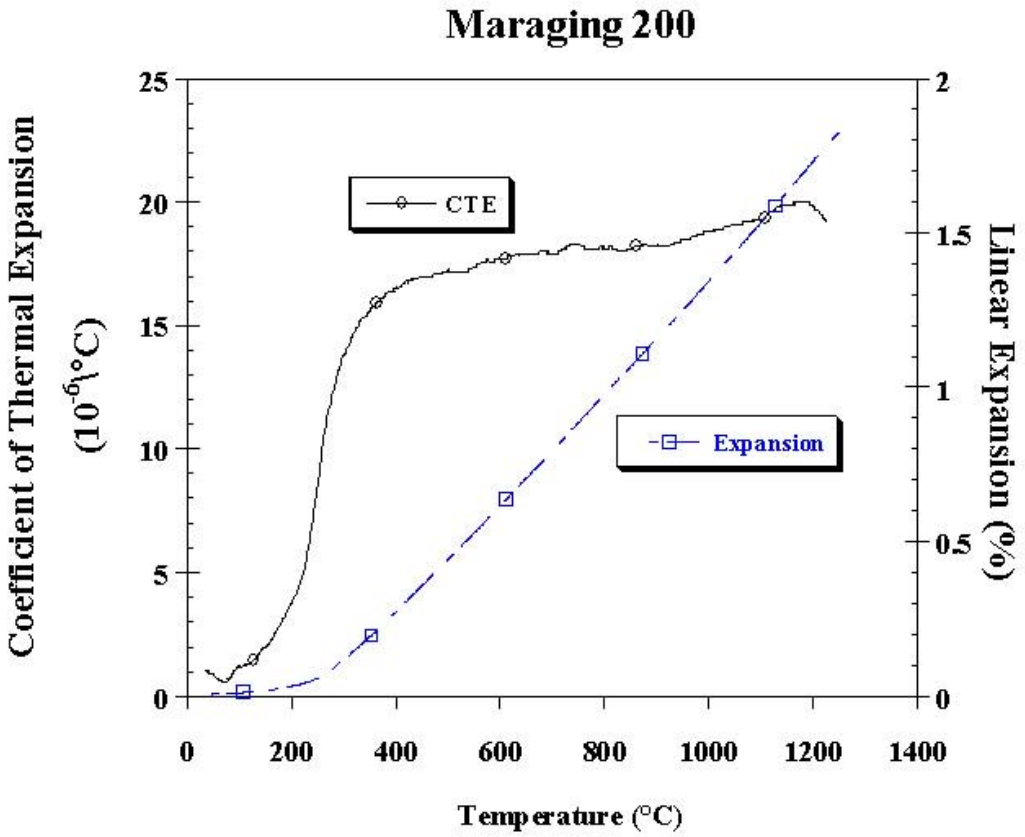

Figure A.2 - CTE and expansion data for as-reduced M200.

Appendix B

LCA Quasi-Static Compressive Behavior

Figure B.1 - Digital image capture of quasi-static out-of-plane compression of annealed Super Invar square annulus LCA at 0.1” per minute to a maximum strain of 46.1%.

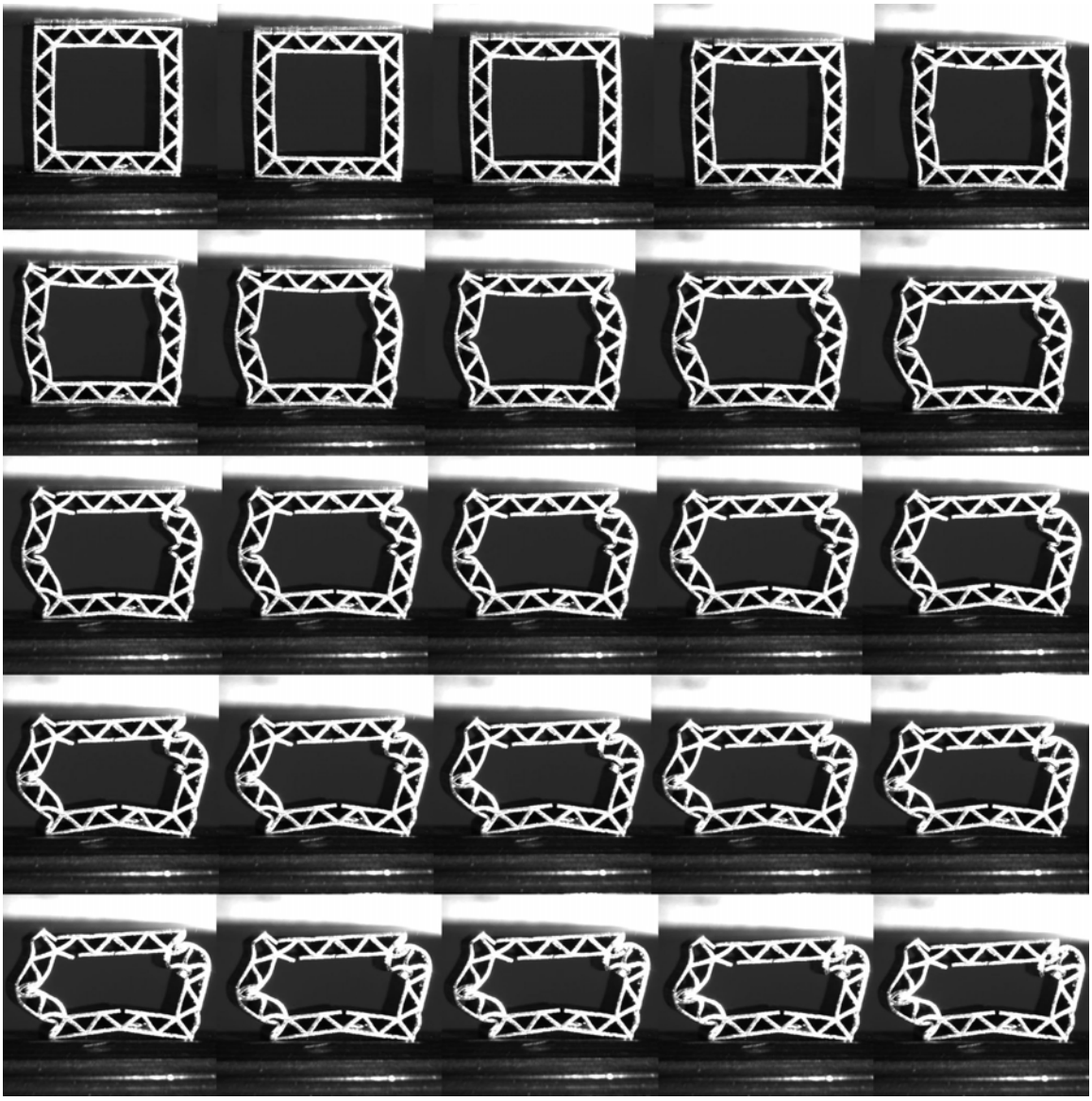

Figure B.2 – Digital image capture of quasi-static in-plane compression of annealed Super Invar square annulus LCA at 0.1” per minute to a maximum strain of 31.5%.

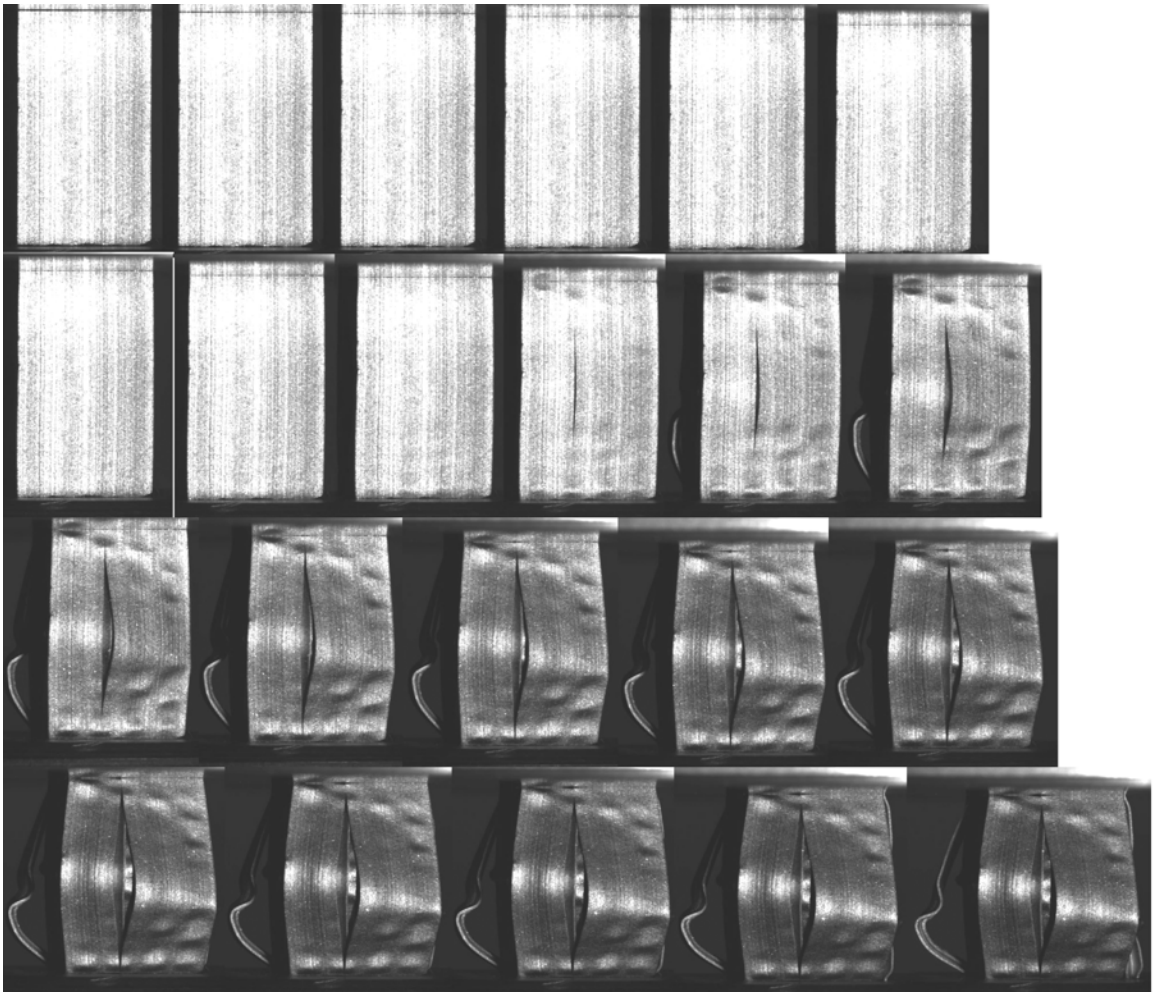

Figure B.3 – Digital image capture of quasi-static out-of-plane compression of hardened Super Invar square annulus LCA at 0.1” per minute to a maximum strain of 22.0%.

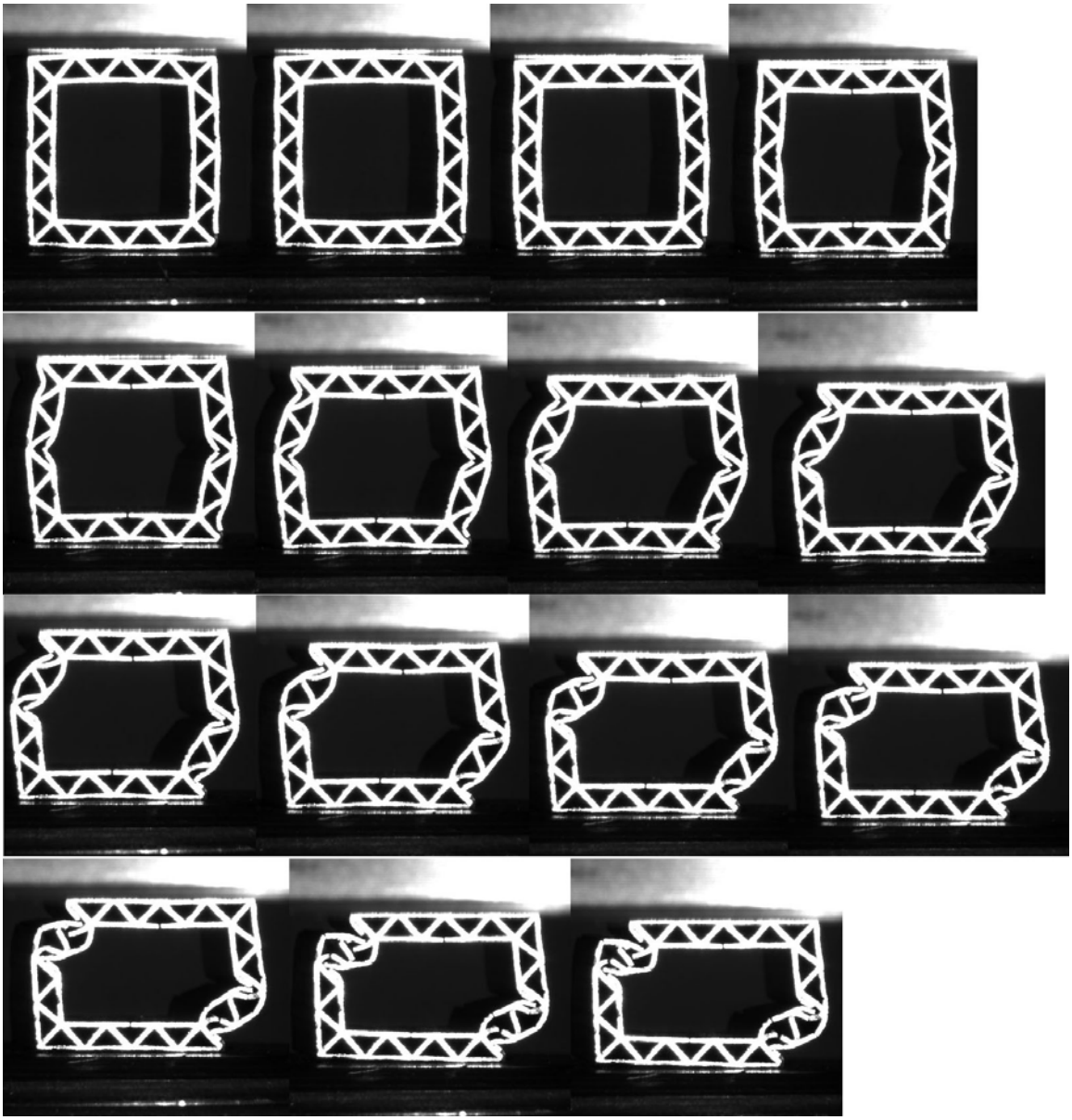

Figure B.4 – Digital image capture of quasi-static in-plane compression of hardened Super Invar square annulus LCA at 0.1” per minute to a maximum strain of 25.5%.

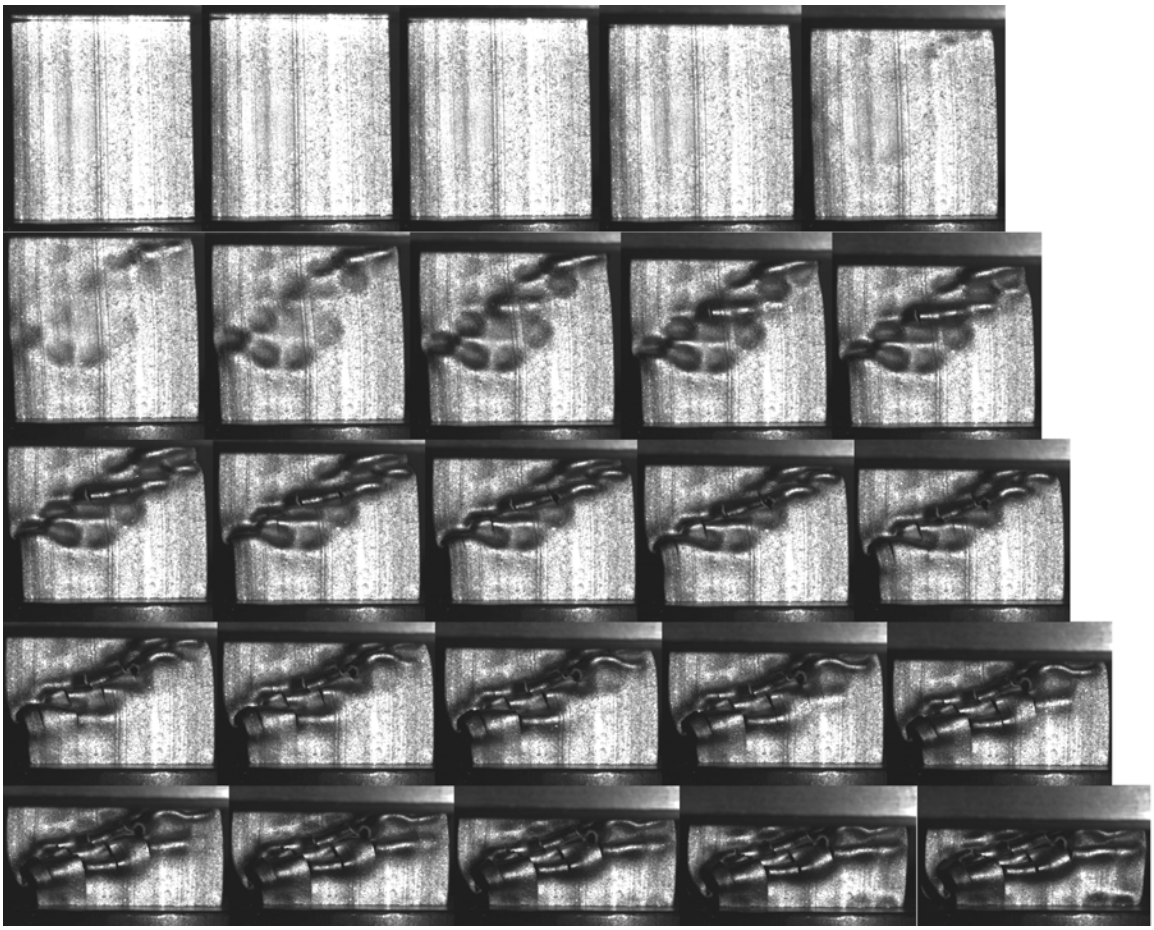

Figure B.5 – Digital image capture of quasi-static out-of-plane compression of annealed Super Invar triangular LCA at 0.1” per minute to a maximum strain of 61.7%.

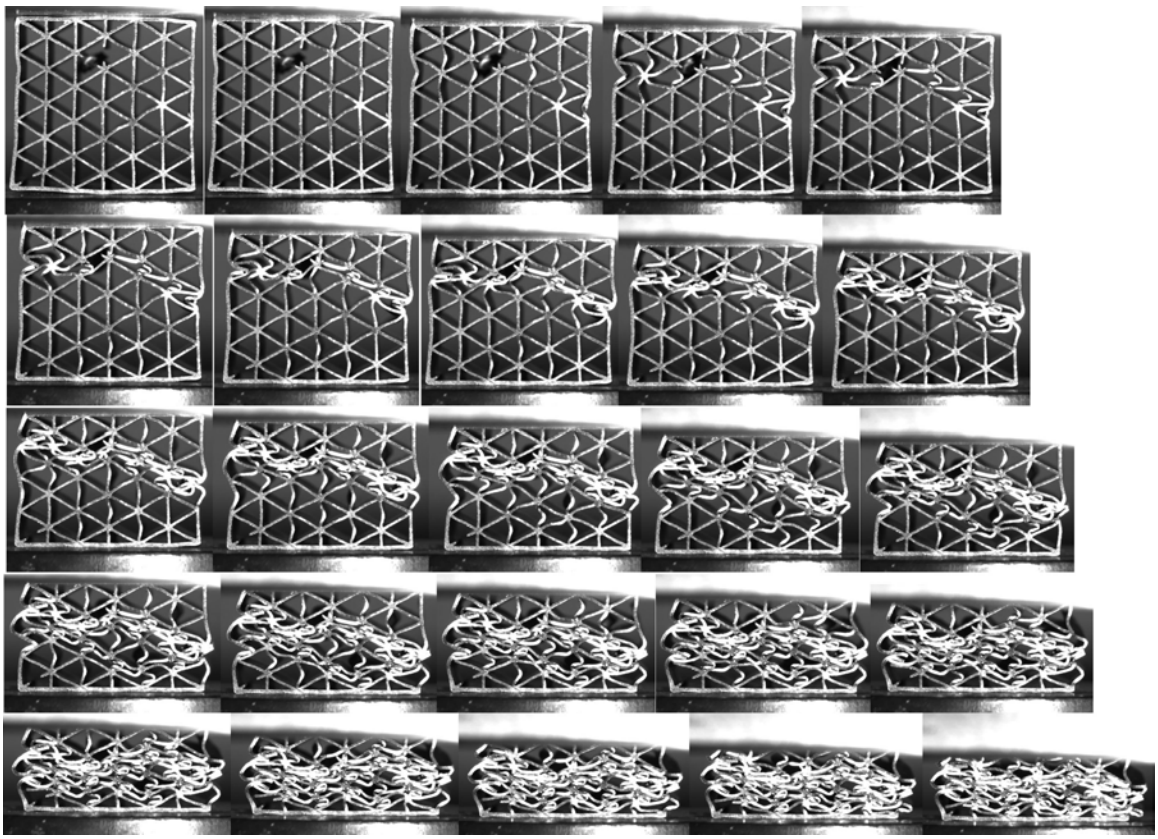

Figure B.6 – Digital image capture of quasi-static in-plane (Orientation 1) compression of annealed Super Invar triangular LCA at 0.1” per minute to a maximum strain of 63.7%.

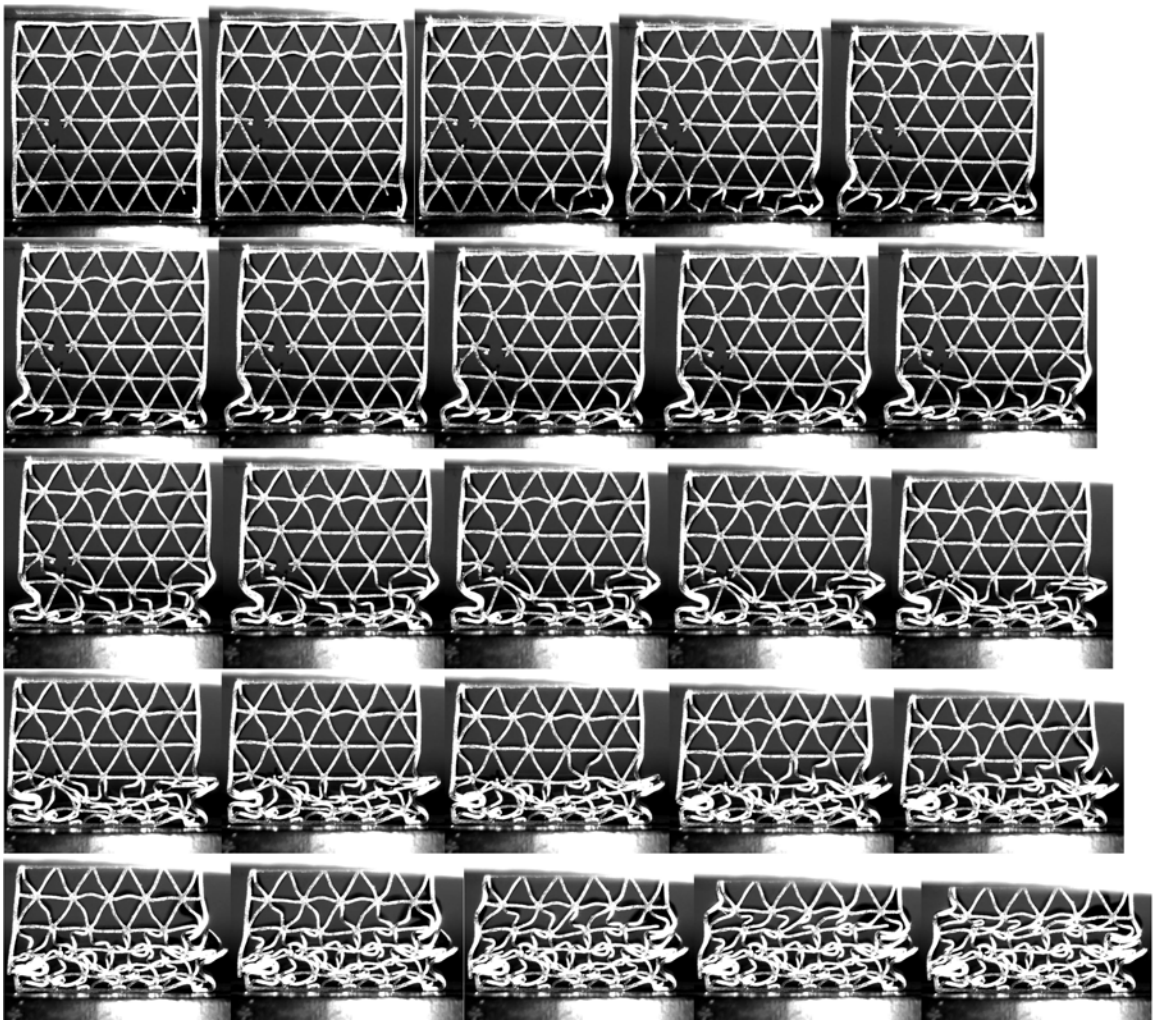

Figure B.7 – Digital image capture of quasi-static in-plane (Orientation 2) compression of annealed Super Invar triangular LCA at 0.1” per minute to a maximum strain of 46.3%.

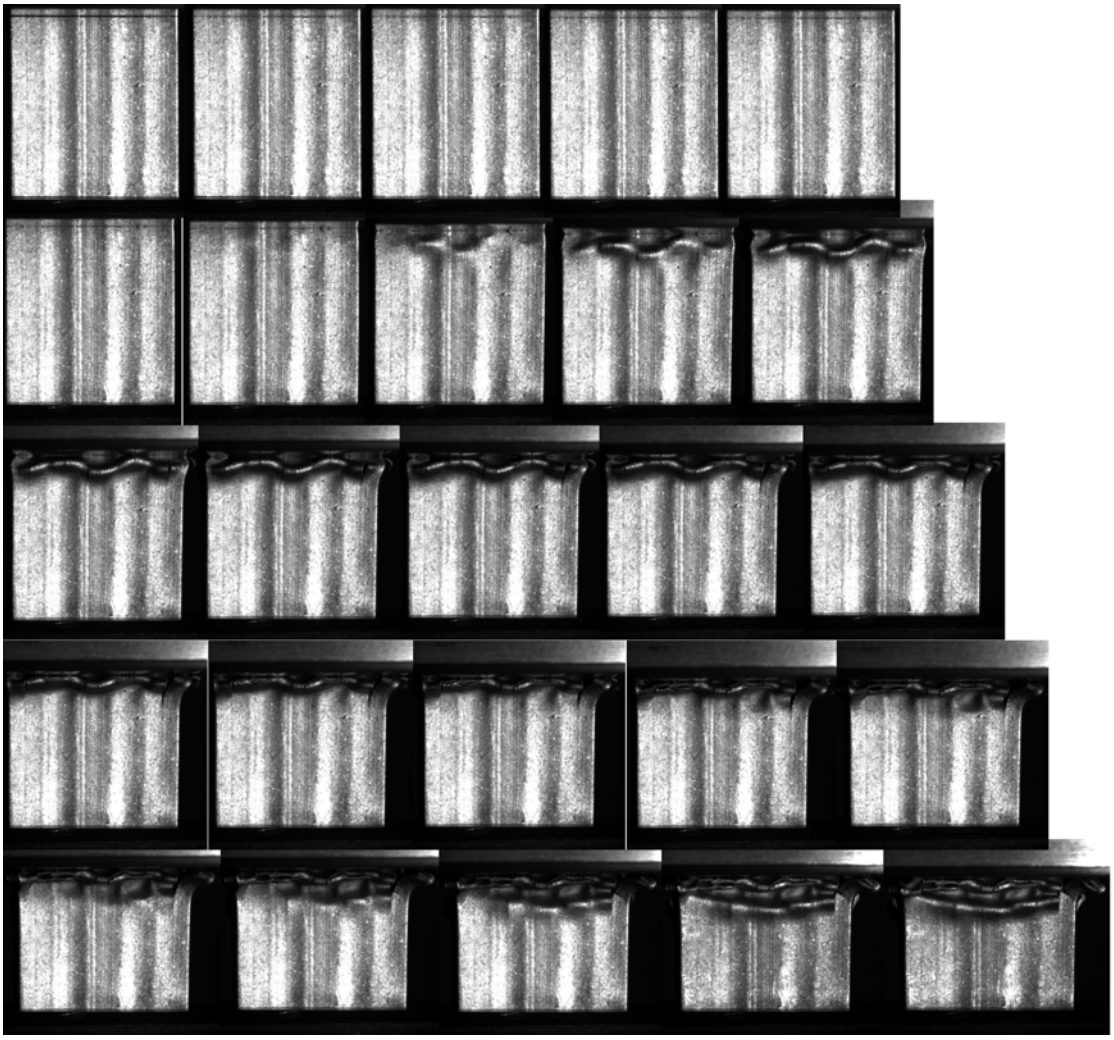

Figure B.8 – Digital image capture of quasi-static out-of-plane compression of hardened Super Invar triangular LCA at 0.1” per minute to a maximum strain of 26.8%.

Figure B.9 – Digital image capture of quasi-static in-plane (Orientation 1) compression of hardened Super Invar triangular LCA at 0.1” per minute to a maximum strain of 61.2%.

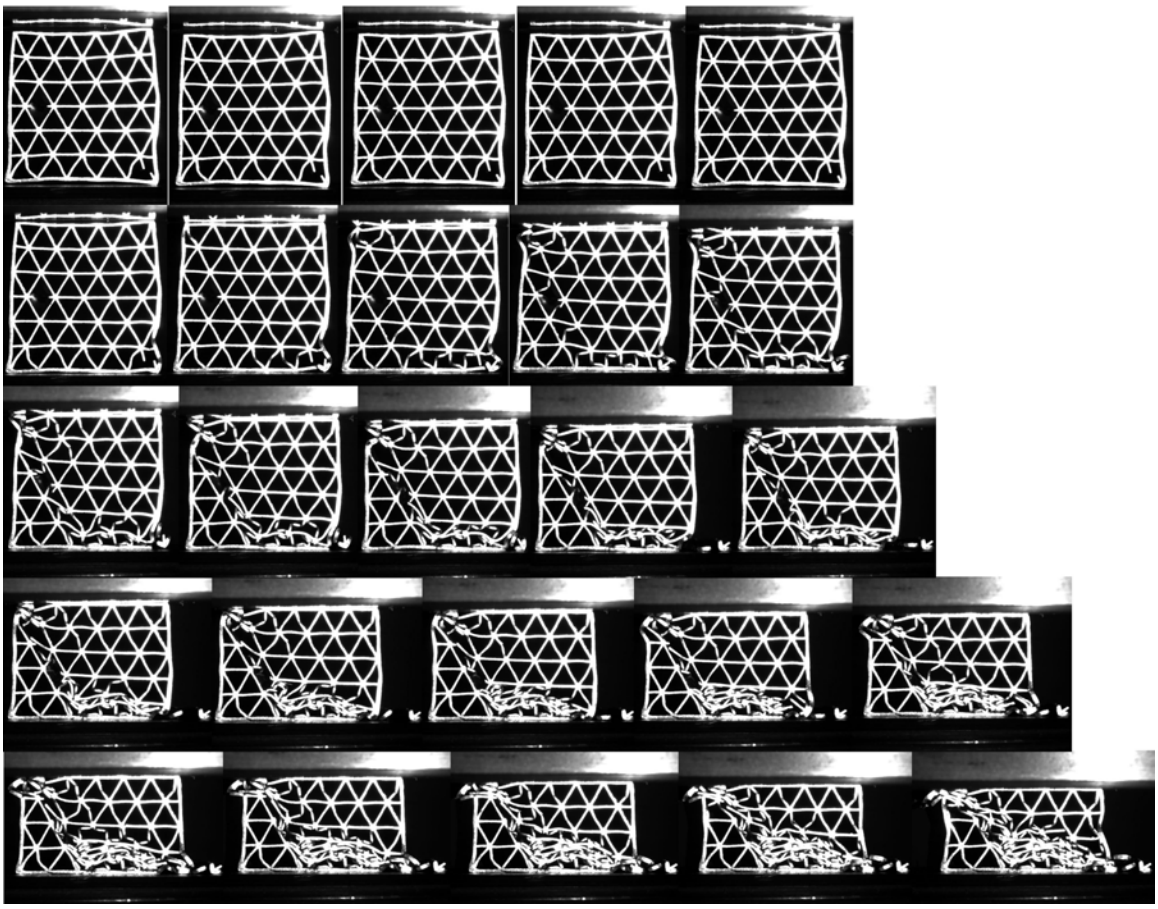

Figure B.10 – Digital image capture of quasi-static in-plane (Orientation 2) compression of hardened Super Invar triangular LCA at 0.1” per minute to a maximum strain of 45.9%.

Appendix C

LCA Dynamic Behavior

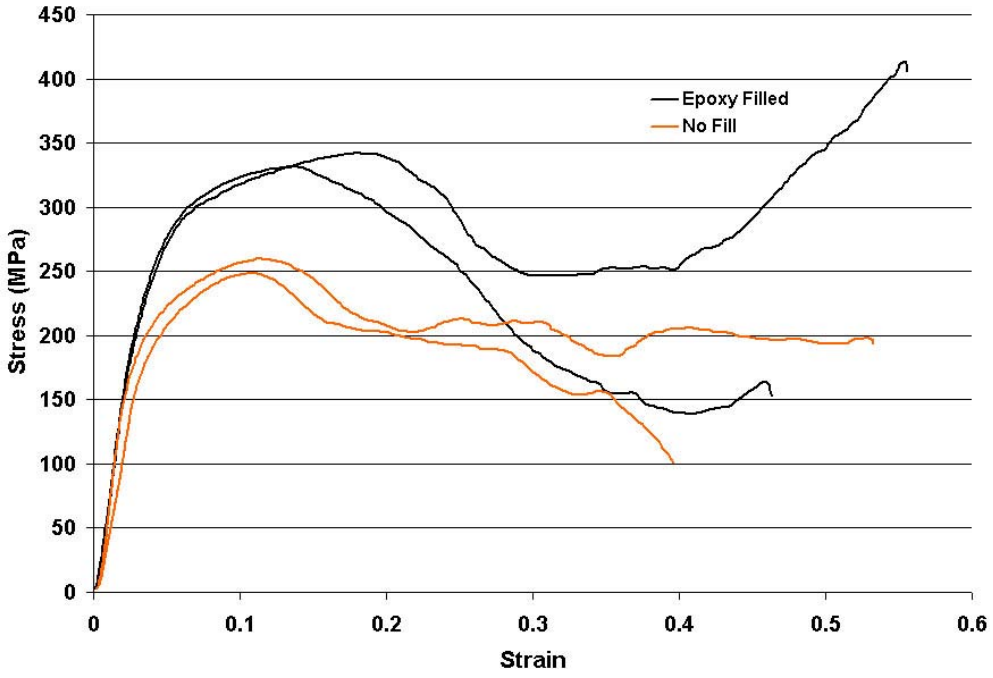

Figure C.1 – Stress-strain behavior for hardened Super Invar Design 1 in filled and unfilled condition.

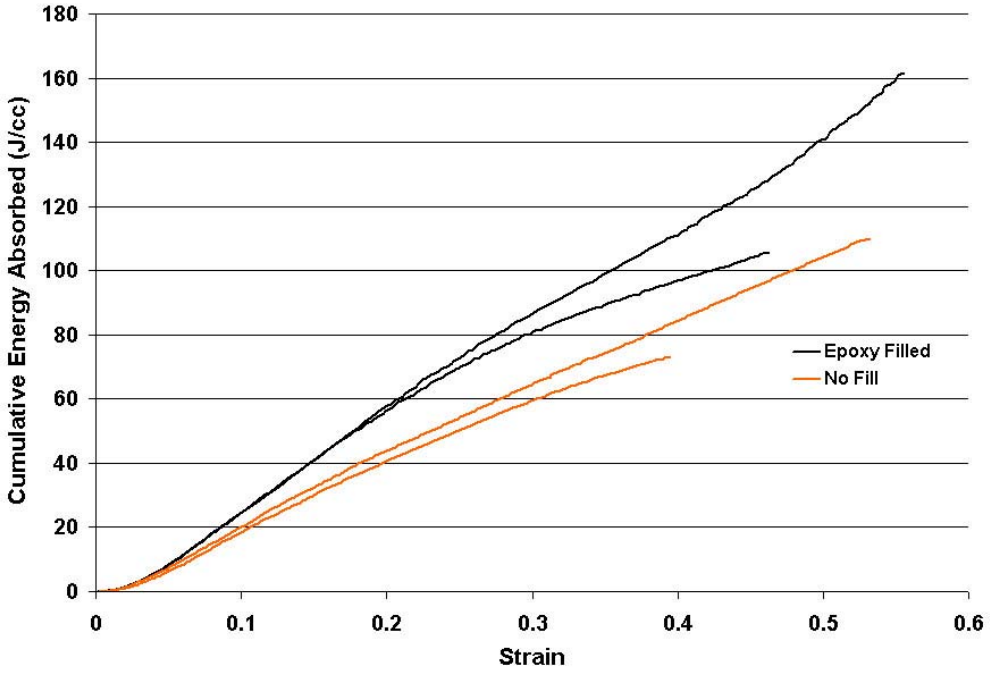

Figure C.2 – Energy absorption for hardened Super Invar Design 1 in filled and unfilled condition.

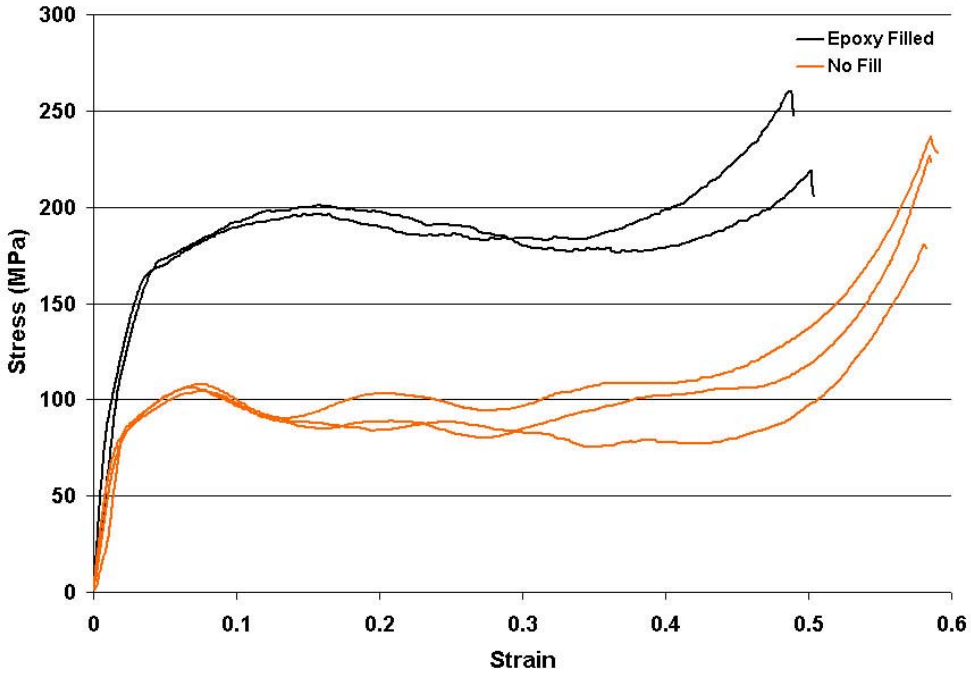

Figure C.3 – Stress-strain behavior for annealed Super Invar Design 2 in filled and unfilled condition.

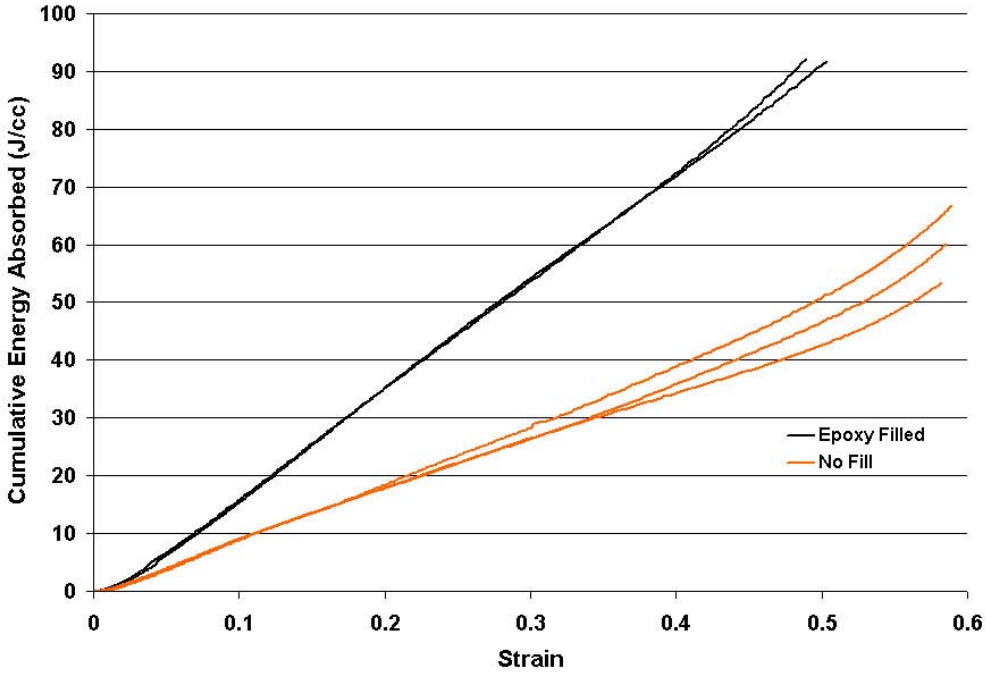

Figure C.4 – Energy absorption for annealed Super Invar Design 2 in filled and unfilled condition.

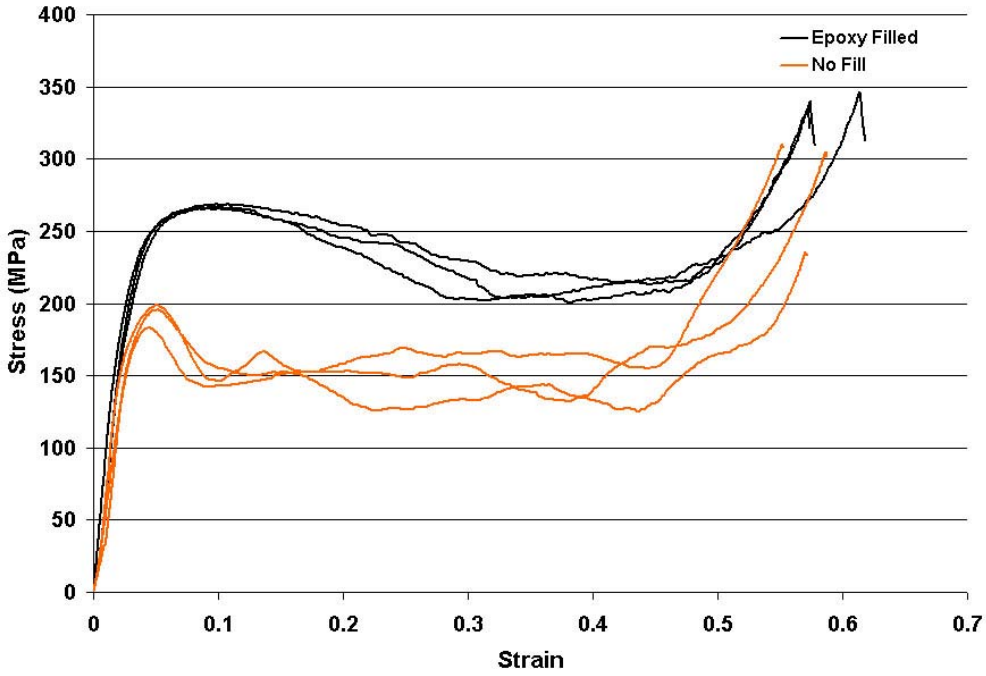

Figure C.5 – Stress-strain behavior for hardened Super Invar Design 2 in filled and unfilled condition.

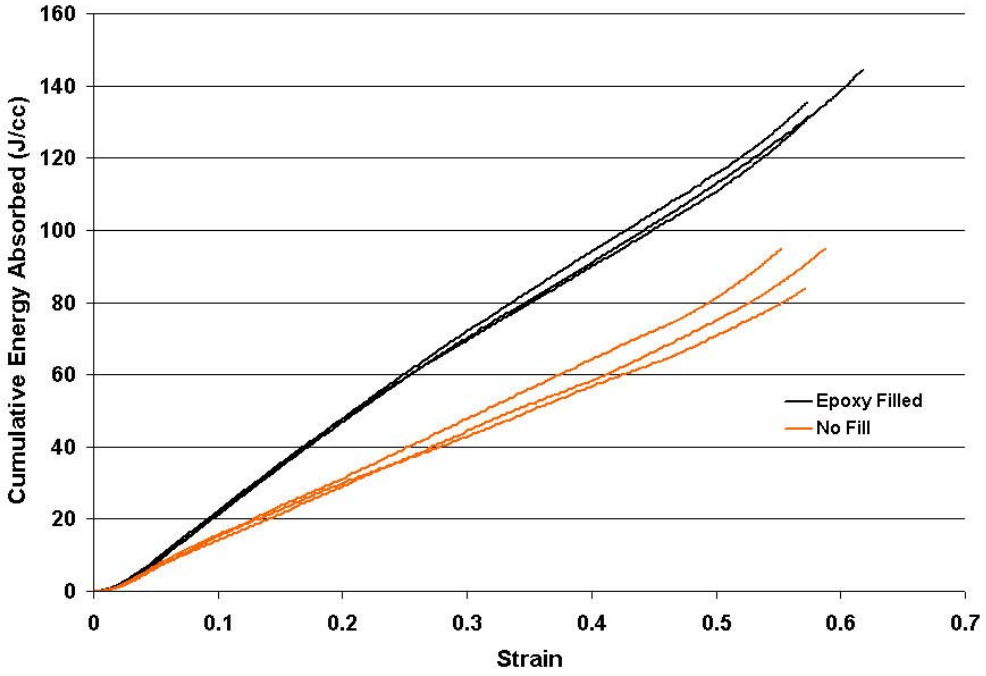

Figure C.6 – Energy absorption for hardened Super Invar Design 2 in filled and unfilled condition.

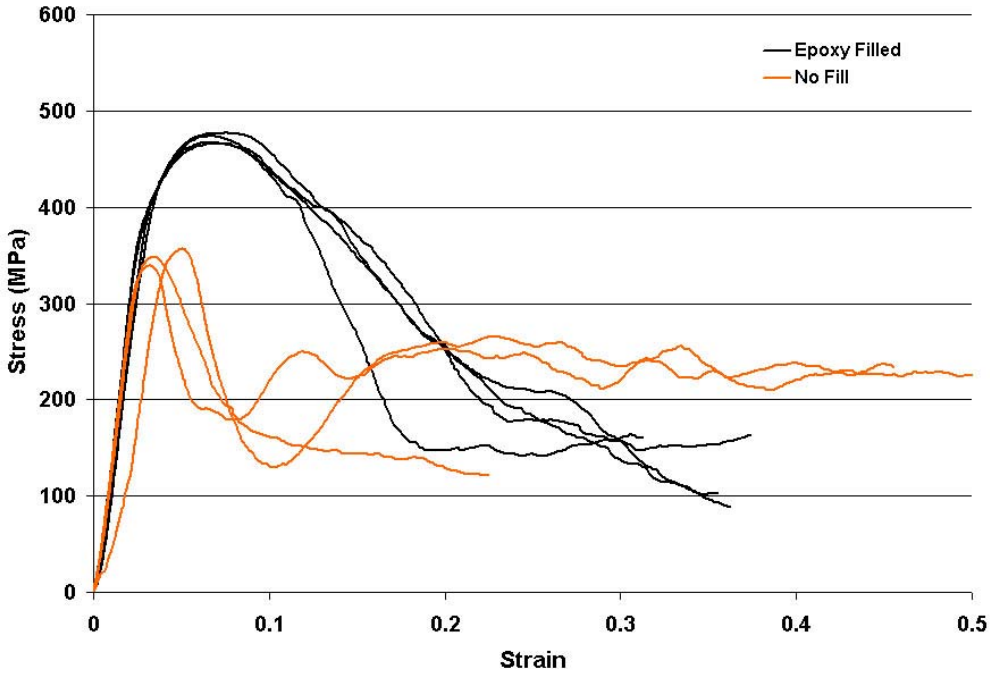

Figure C.7 – Stress-strain behavior for maraging 200 Design 2 in filled and unfilled condition.

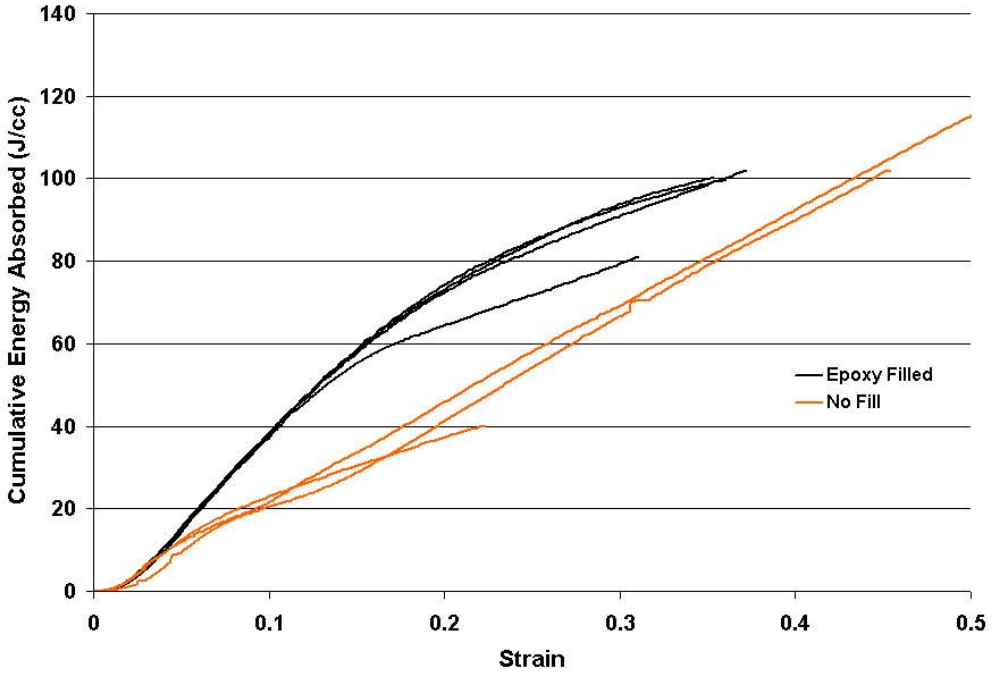

Figure C.8 – Energy absorption for maraging 200 Design 2 in filled and unfilled condition.

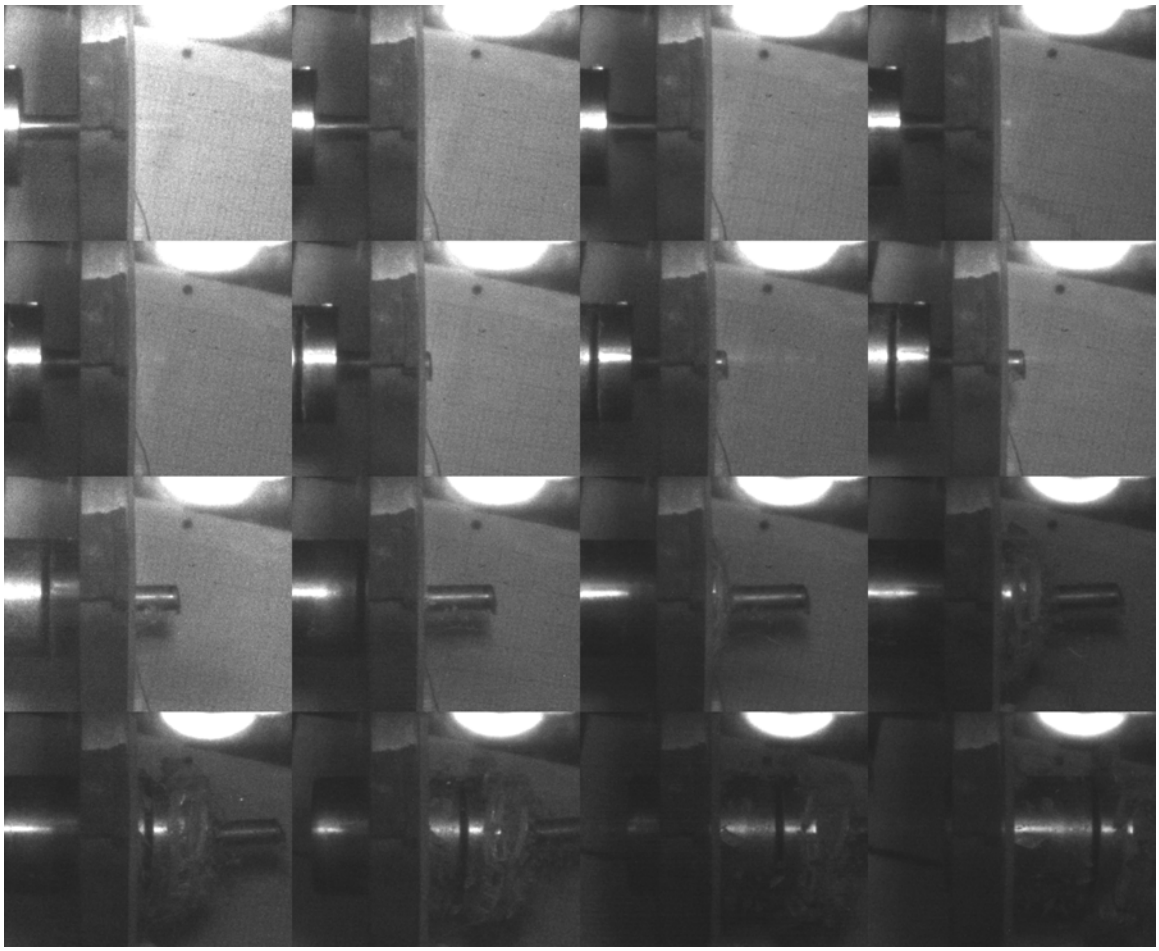

Figure C.9 – Image capture data of copper rod tested in the reverse Taylor setup with a projectile velocity of 119.74 m/s.

Figure C.10 – Image capture data of annealed Super Invar EC1 filled with epoxy tested in the reverse Taylor setup with a projectile velocity of 118.70 m/s.

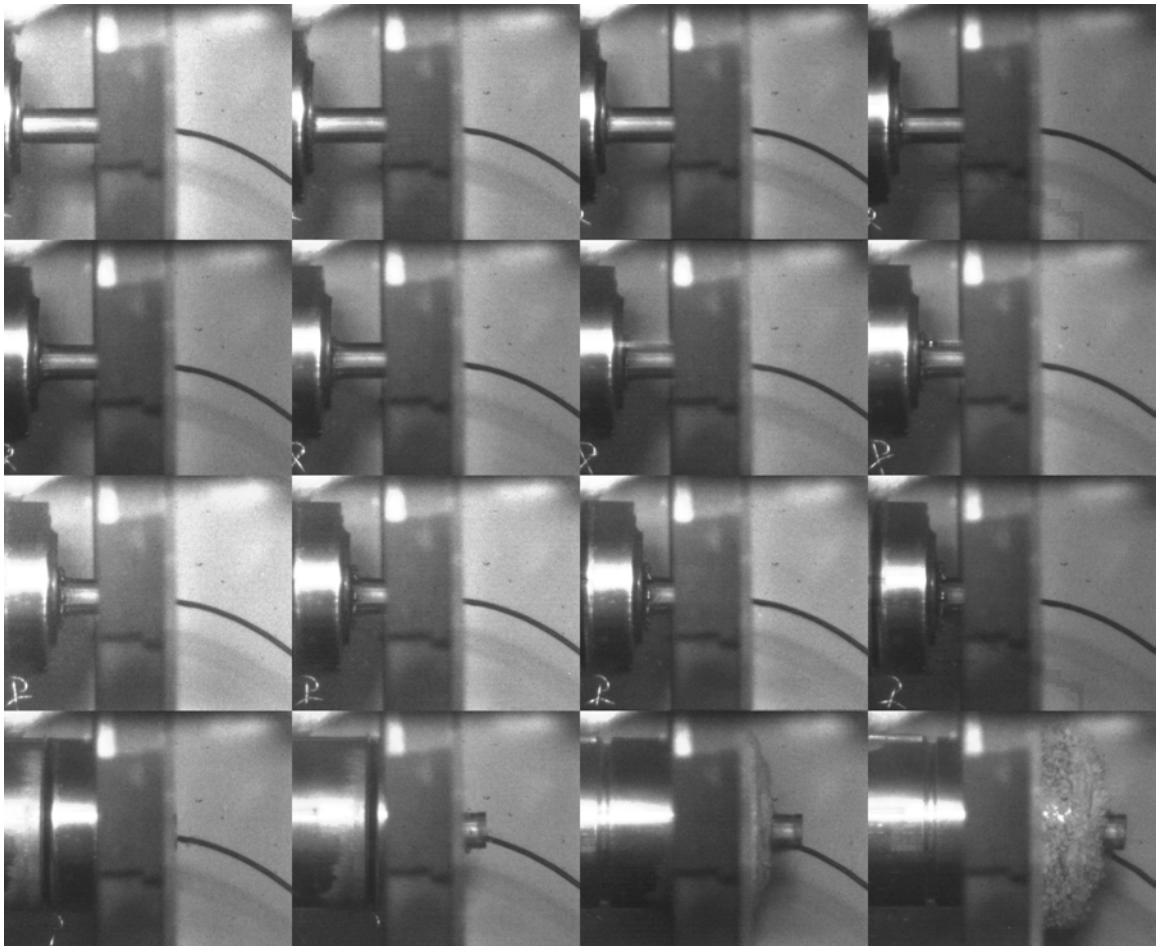

Figure C.11 - Image capture data of unfilled, annealed Super Invar EC1 tested in the reverse Taylor setup with a projectile velocity of 416.70 m/s.

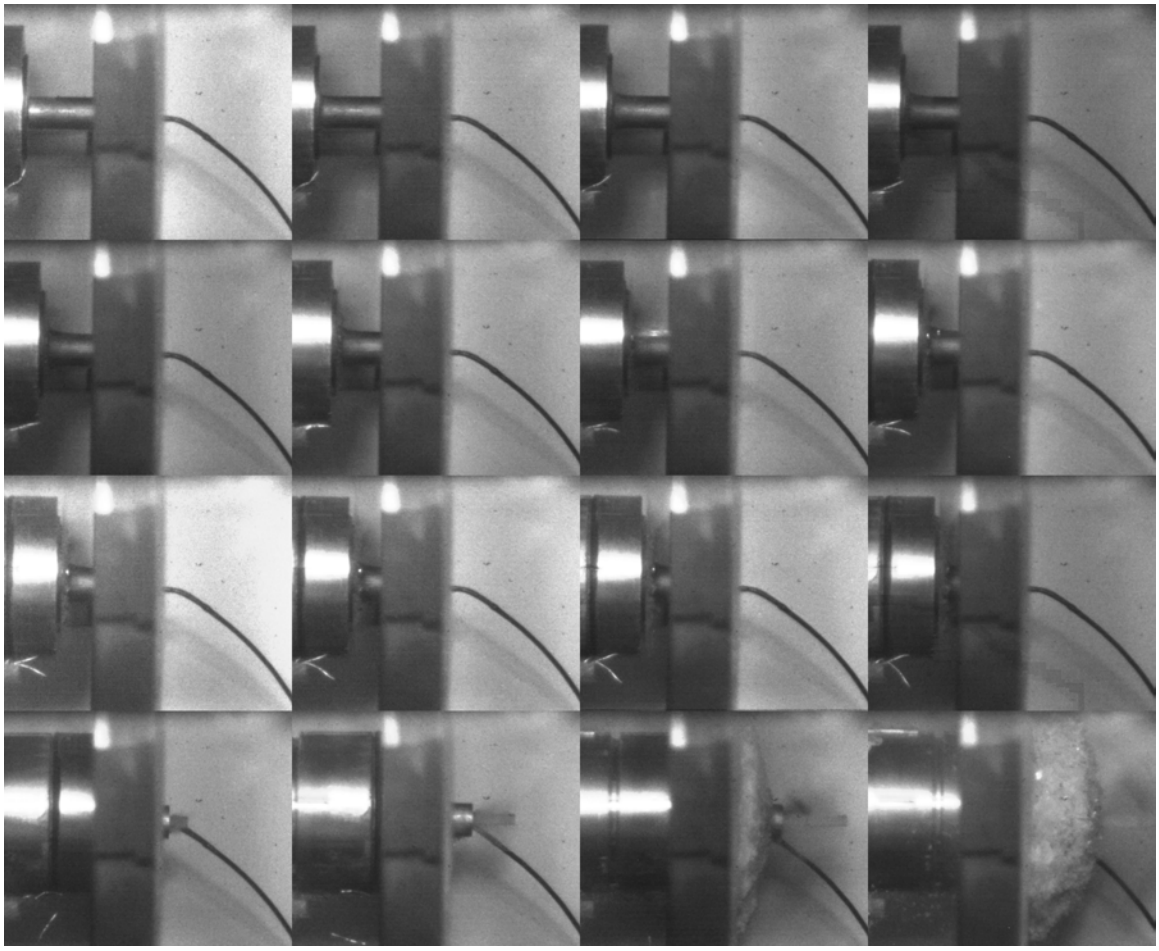

Figure C.12 - Image capture data of epoxy filled, annealed Super Invar EC1 tested in the reverse Taylor setup with a projectile velocity of 419.10 m/s.

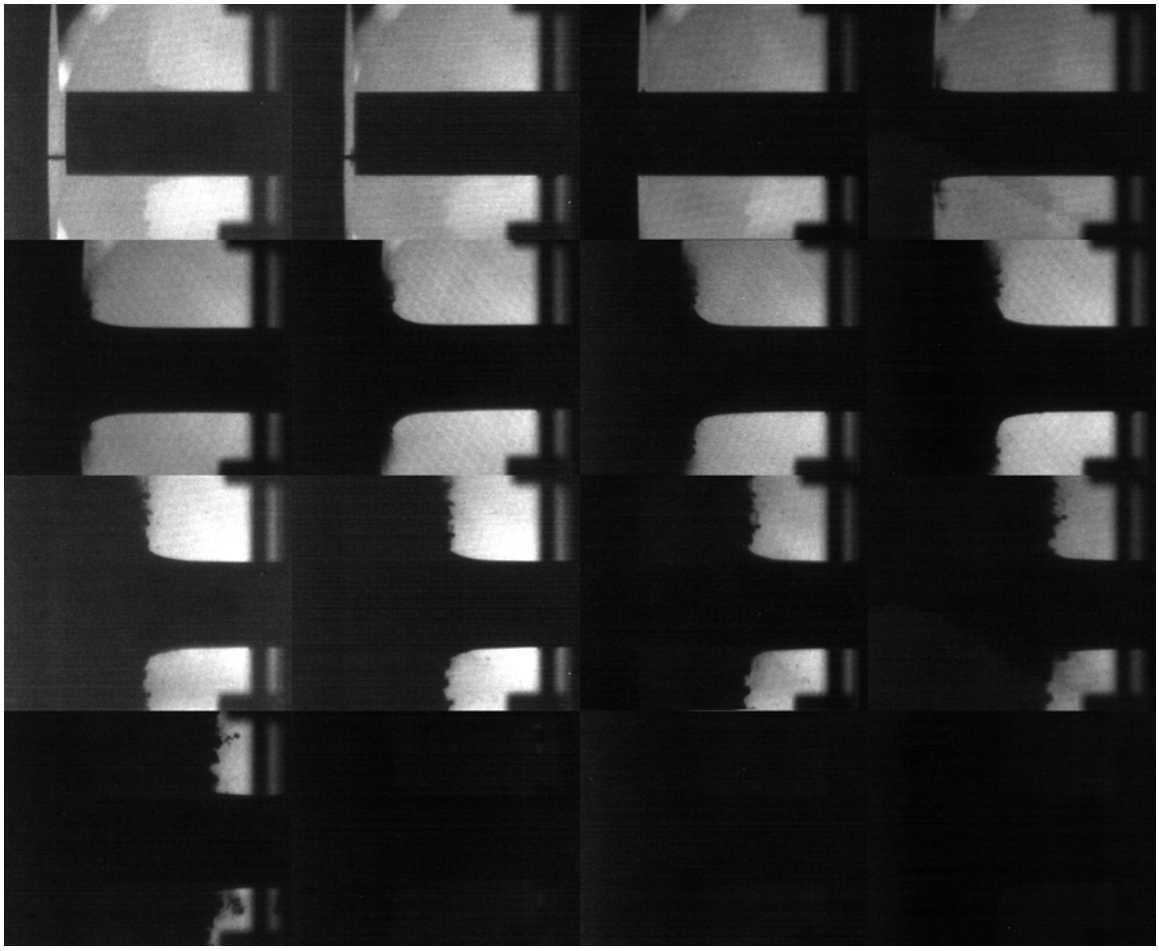

Figure C.13 - Image capture data of filled M200 EC1 tested in the reverse Taylor setup with a projectile velocity of 407.10 m/s.

References

1. Banhart, J., "Production Methods for Metallic Foams," Fraunhofer USA Metal Foam Symposium, 1997, pp 3 - 11.

2. Banhart, John, "Manufacture, Characterisation, and Application of Cellular Metals and Foams," Progress in Materials Science, 46, 2001, 559-632

3. Wood, J.T., "Production and Applications of Continuously Cast, Foamed Aluminum," Fraunhofer USA Metal Foam Symposium, 1997, pp. 31- 35.

4. K.M. Hursyz, *Paste Mechanics of Fine Extrusion*, Ph.D. Thesis, School of Materials Science and Engineering, Georgia Institute of Technology, Atlanta, GA, 2001.

5. Decker, R.F., Eash, J.T., and Goldman, A.J., "18% Nickel Maraging Steel", Source Book on Maraging Steels (Metals Park, OH: American Society for Metals, 1979), pp. 1-19.

6. Reed, James S., Principles of Ceramics Processing, 2nd Edition, John Wiely & Sons, Inc., New York, 1995.

7. German, Randall M., Powder Metallurgy Science, 2nd Ed., Metal Powder Industries Federation, New Jersey, 1994.

8. Komatsubara, N., Hayselden, C., and Cantor, B., "Microstructures and Mechanical Properties of HIP Consolidated 18% Ni Maraging Steel", Powder Metallurgy, v30, n2, 1987, pp119-124.

9. Van Swam, L.F., Pelloux, R.M., and Grant, N.J., "Properties of Maraging Steel 300 Produced by Powder Metallurgy", Powder Metallurgy, v17, n33, 1974, pp. 33-45.

10. Bocchini, G.F., "The Influence of Porosity on the Characteristics of Sintered Materials," The International Journal of Powder Metallurgy, 22 (3) (1986), 185-202.

11. Nadler, Jason, "The Hydrogen Reduction of Iron and Chromium Oxides", PhD Dissertation, Georgia Institute of Technology, May 2003.

12. Sha, W., Cerezo, A., and Smith, G. D. W., "Phase Chemistry and Precipitation Reactions in Maraging Steels: Part IV. Discussion and Conclusions", Metallurgical Transactions A, Vol 24A, June, 1993, pp. 1251-56.

13. Hall, M. and Slunder, J., The Metallurgy and Application of the 18-Percent Nickel Maraging Steels, Nasa Aeronautics and Space Administration, Washington, D.C., 1968.

14. Isserow, S., "Type 350 Maraging Steel Processed by Powder Metallurgy," Powder Metallurgy, No. 3, 1977, pp. 137-144.

15. Tracey, V.A. and Raman, R.S.K., "The Mechanical Properties of Some Sintered Maraging Steels," Powder Metallurgy, vol. 12, no. 23, 1969, 131-56.

16. Komatsubara, K., Hayzelden, C., and Cantor, B., "Microstructures and Mechanical Properties of HIP Consolidated 18% Ni Maraging Steel," Powder Metallurgy, vol. 30, no.2, 1987, pp. 119-24.

17. Joseph Davis et al., eds., Metals Handbook, vol. 1 (Materials Park, OH: ASM International, 1990) 793.

18. Y. He, K. Yang, W. Qu, F. Kang, and G. Su, "Strengthening and Toughening of a 2800-MPa Grade Maraging Steel," *Materials Letters*, 56, Nov. 2002, pp. 763-9.

19. Saito, H et al., eds., Physics and Applications of Invar Alloys, (Tokyo, Japan: Maruzen Company, Ltd., 1978), pp. 530-1.

20. Carpenter Technology Corporation, Alloy Technical Information, 1047 Park Road, Wyomissing, PA 19610-1339.

21. Meyers, Marc A., Dynamic Behavior of Materials, John Wiely & Sons, Inc., New York, 1994, pp. 31-40.

22. V.D. Eisenhuttenleute, ed., Steel: A Handbook for Materials Research and Engineering, vol. 2 (Springer-Verlag, Dusseldorf, 1993) 216.

23. German, R.M. and Smugeresky, J.E., "Ductility in Hot Isostatically Pressed 250-Grade Maraging Steel", Source Book on Maraging Steels (Metals Park, OH: American Society for Metals, 1979), pp. 291-298.

24. V. Thomas and D.J. Jones, "Low-Expansion Nickel-Iron Alloys Prepared by Powder Metallurgy," Symposium on Powder Metallurgy, 1954, 200-203.

25. Papka, Scott D. and Kyriakides, Stelios, "In-Plane Compressive Response and Crushing of Honeycomb," *J. Mech. Phys. Solids*, Vol. 42, No. 120, pp. 1499-1532, 1994.

26. Klintworth, J.W. and Stronge, W.J., "Elasto-Plastic Yield Limits and Deformation Laws for Transversely Crushed Honeycombs," *Int. J. Mech. Sci.*, Vol. 30, No. ¾, pp. 273-292, 1988.

27. Gibson, L.J. and Ashby, M.F., Cellular Solids: Structure and Properties, 2nd edn, Cambridge University Press, Cambridge, 1997.

28. H. E. M. Hunt, "The Mechanical Strength of Ceramic Honeycomb Monoliths as Determined by Simple Experiments," Trans IchemE, Vol. 71, Part A, May 1993, pp. 257-266.

29. Hayes, Alethea M., Wang, Aijun, Dempsey, Benjamin M., and McDowell, David L., "Mechanics of Linear Cellular Alloys", In Revision.

30. Wang, A,-J. and McDowell, D.L., "In-Plane Stiffness and Yield Strength of Periodic Metal Honeycombs," submitted to ASME Journal of Engineering Materials and Technology, July 2002, to appear.

31. Wierzbicki, T., "Crushing Analysis of Metal Honeycombs," (1983), Int. J. Impact Engng., Vol. 1, No. 2, pp. 157-174.

32. Bhat, B. T., and Wang, T. G., "A Comparison of Mechanical Properties of Some Foams and Honeycombs", Journal of Materials Science, vol. 25, Dec. 1990, p. 5157-5162.

33. Sanders, W. and Gibson, L.J., "Reduction in Young's Modulus of Aluminum Foams Due to Cell Wall Curvature and Corrugation," *Mat. Res. Soc. Symp. Proc.*, Vol 521, Materials Research Society, pp. 53-7, 1998.

34. Fortes, M.A. and Ashby, M.F., "The Effect of Non-Uniformity on the In-Plane Modulus of Honeycombs," *Acta Mater.*, Vol. 47, No. 12, pp. 3469-3473, 1999.

35. Simone, A.E. and Gibson, L.J., "Effects of Solid Distribution on the Stiffness and Strength of Metallic Foams," *Acta Mater.*, Vol. 46, No. 6, pp. 2139-2150, 1998.

36. Guo, X.E., and Gibson, L.J., "Behavior of Intact and Damaged Honeycombs: A Finite Element Study," *International Journal of Mechanical Sciences*, 41, pp. 85-105, 1999.

37. Chen, C., Lu, T.J., and Fleck, N.A., "Effect of Inclusions and Holes on the Stiffness and Strength of Honeycombs," *International Journal of Mechanical Sciences*, 43, pp. 487-504, 2001.

38. Albuquerque, J.M., Fatima Vaz, M., and Fortes, M.A., "Effect of Missing Walls on the Compression Behaviour of Honeycombs," *Scripta Materialia*, Vol. 41, No. 2, pp. 167-174, 1999.

39. Wang, A,-J. and McDowell, D.L., "Effects of Defects on In-Plane Properties of Periodic Metal Honeycombs," submitted to International Journal of Mechanical Sciences, August 2002, to appear.

40. Onck, P.R., "Scale Effects in Cellular Materials," *MRS Bulletin*, v 28, n 4, April, 2003, pp. 279-283.

41. Onck, P.R., Andrews, E.W., and Gibson, L.J., "Size Effects in Ductile Cellular Solids. Part I: Modeling," *International Journal of Mechanical Sciences*, 43, 2001, pp. 681-699.

42. Andrews, E.W., Gioux, G., Onck, P., and Gibson, L.J., "Size Effects in Ductile Cellular Solids. Part II: Experimental Results," *International Journal of Mehcanical Sciences*, 43, 2001, pp. 701-713.

43. Abramowicz, W. and Wierzbicki, T., "Axial Crushing of Multicorner Sheet of Metal Columns," *Journal Applied Mechanics*, Transactions of the ASME, Vol. 56, No. 3, pp. 113-120, 1989.

44. Santosa, S. and Wierzbicki, T., "On the Modeling of Crush Behavior of a Closed-Cell Aluminum Foam Structure," *J. Mech. Phys. Solids*, Vol. 46 No. 4, pp. 645-669, 1998.

45. Wang, A., Totty, J., and McDowell, D., "Out-of-Plane Crushing Behavior of Periodic Metal Honeycombs," To be published.

46. Hayes, Alethea M., "Compression Behavior of Linear Cellular Steel," Master's Thesis, Georgia Institute of Technology, August 2001.

47. Ashby, M.F., Evans, A., Fleck, N.A., Gibson, L.J., Hutchinson, J.W., Wadley, H.N.G., Metal Foams – A Design Guide, Butterworth-Heinemann, Boston, 2000.

48. Von Karman, T. and Duwez, P., J. P;;l. Phys., vol. 21, 1950, p. 987.

49. Taylor, G., "The Use of Flat-Ended Projectiles for Determining Dynamic Yield Stress. I. Theoretical Considerations," Proceedings of the Royal Society of London. Series A, Mathematical and Physical Sciences, Vol. 194, No. 1038, Sep. 2, 1948, 289-299.

50. Whiffin, A.C., "The Use of Flat-Ended Projectiles for Determining Dynamic Yield Stress. II. Tests on Various Metallic Materials," Proceedings of the Royal Society of London. Series A, Mathematical and Physical Sciences, Vol. 194, No. 1038, Sep. 2, 1948, 300-322.

51. Wilkins, M.L., and Guinan, W., "Impact of Cylinders on a Rigid Boundary," J. Appl. Phys., Vol. 44, No. 3, March 1973, pp. 1200-1206.

52. Johnson, G.R. and Cook, W.H., Poc. 7th Intern. Symp. Ballistics, Am. Def. Prep. Org. (ADPA), Netherlands, 1983.

53. Rule, W.K. and Jones, S.E., "A Revised Form for the Johnson-Cook Strength Model," Int. J. Impact Engng, Vol. 21, No. 8, pp. 609-624, 1998.

54. Mott, N.F., "Fragmentation of Shell Cases," Proceedings of the Royal Society of Londan. Series A, Mathematical and Physical Sciences, Vol. 189, No. 1018, May 1, 1947, pp. 300-308.

55. Grady, D.E. and Kipp, M.E., Proc. 20th Symposium on Rock Mechanics, Austin, 1979, p. 403.

56. Grady, D.E. and Kipp, M.E., Int. J. Rock Mech. Min. Sci., Vol 17, 1980, p. 147.

57. Yew, C.H. and Taylor, P.A., "A Thermodynamic Theory of Dynamic Fragmentation," Int. J. Impact Engng, Vol. 15, No. 4, pp. 385-394, 1994.

58. Kipp, M.E., Grady, D.E., and Swegle, J.W., "Numerical and Experimental Studies of High-Velocity Impact Fragmentation," Int. J. Impact Engng, Vol. 14, pp. 427-438, 1993.

59. Grady, D.E. and Kipp, M.E., "Experimental Measurement of Dynamic Failure and Fragmentation Properties of Metals," Int. J Solids Structures Vol, No 17/18, pp. 2779-2791, 1995.

60. Grady, D.E. and Kipp, M.E., "Fragmentation Properties of Metals," Int J. Impact Engng, Vol. 20, pp. 293-308, 1997.

61. Xu, X. and Thadhani, N., "Investigation of Shock-Induced Reaction Behavior of As-Blended and Ball-Milled Ni+Ti Powder Mixtures Using Time-Resolved Stress Measurements," AIP Conference Proceedings, Vol. 620(1), pp. 1123-1126, July 8, 2002.